Gamma emission from clustered states in ^{16}O nuclei

By

Pedro Humberto Santa Rita Alcibia

A thesis submitted to
the University of Birmingham
for the degree of
DOCTOR OF PHILOSOPHY

Nuclear Physics Research Group
School of Physics and Astronomy
College of Engineering and Physical Sciences
University of Birmingham
September 2022

Dedicada a Martha Alcibia, mi mamá

ABSTRACT

The experiment involving the reaction $(\alpha + ^{12}\mathrm{C}) \rightarrow (^{16}\mathrm{O}^{*} + \gamma) \rightarrow (\alpha + ^{12}\mathrm{C}_{g.s.})$ was performed at the University of Birmingham MC40 cyclotron facility at a beam energy of 12.29±0.04 MeV to study the gamma to alpha emission ratio of a suspected clustered state in ^{16}O at 16.272 MeV , $J = 6^{+}$. Finding a reduced transition probability value of $B(E2; 6^{+} \rightarrow 4^{+}) = 3.316 \pm 1.736_{w.u.} = 7.942 \pm 4.158\ e^{2}fm^{4}$.

This work also presents a method to create simulations of alpha-gamma coincidences with realistic detectors response, which is used to decompose and analyse the components of the detected gamma spectrum to extract the the reduced transition probability. The methods described in this work can be employed to study nuclear structure properties by gamma emission of other light nuclei.

ACKNOWLEDGMENTS

This work would not be possible without my supervisors Tzany Kokalova-Wheldon and Carl Wheldon, not only they taught me about physics but made me feel as part of a family during my stay in the UK. Thank you for everything!

This work, the living costs during my PhD and part of the tuition fees, are possible thanks to the "Becas al extranjero 2017" program from Mexican Government through the **CONACYT** and The University of Birmingham's School of Physics and Astronomy which helped me to complement my annual tuition.

I was very welcomed to the UK by its people, thank you to all the friends I made during my stay!

This work has been the greatest challenge of my life, it was a trying time as I experience loss as I never felt before. This experience taught me a great deal of nuclear experimental physics and about the person I am.

DEDICACÍON

Este trabajo está dedicado a Martha Alcibia Valdez, mi mamá, sin ti toda esta aventura no hubiera existido, gracias por apoyarme en cada paso que he dado, gracias por enseñarme tanto, gracias por tanto cariño y tanta paciencia.

También quiero dedicar este trabajo a mi pareja Grisel Mendez, tu apoyo ha sido impresionante y agradezco mucho la paciencia y fuerza que tuvimos para poder aguantar tanto dolor que hemos sentido durante esta aventura, gracias por hacer momentos tan bonitos conmigo que jamás olvidare. No hay palabras para expresar lo afortunado de tenerte a ti y a nuesta bebé en camino.

Y a mis abuelos, Martha y Pedro porque siempre se sintieron orgullosos de mi y me lo hicieron y hacen saber.

Mi familia ha sido un pilar de fortaleza para mi y en cada momento me hicieron sentir el orgullo que sentían por mi.

Los quiero mucho a todos!

Mis hermanos Omar, Tibu y Julio que me hacian olvidar un poco la lejania, jamas voy a olvidar su apoyo y su carino ademas esas victorias en el battle royal. Mis primas Carmen,Andrea y Karla que adoro con todo mi corazon

Mis tias Claudia, Carmen, Esther y Sosy han sido importantisimas en mi vida y he sentido su carino en cada paso que doy.

A mis tios y mi papá, de los cuales he aprendido tanto.

Contents

List of Figures

Chapter 1

Introduction

1.1 A short history of nuclear physics

"I see now that the circumstances of one's birth is irrelevant, it is what you do with the gift of life that determines who you are"

-Mewtwo

HE study of Nuclear Physics is still an evolving field, as new experimental data and theoretical models cannot yet fully explain all the physical phenomena we observe in the universe. Ever since the discovery of the atomic nucleus, people have been fascinated by its immense power.

Modern facilities, more efficient detectors, powerful computers, and the collaborative efforts of physicists worldwide are all converging to unravel the mysteries of the nuclear realm.

The study of Nuclear Physics began in 1896 with Henri Becquerel. While studying x-rays from Uranium salts, he observed their impact on photographic plates. Further investigation revealed that the activity registered on the plates was not merely atomic; it was nuclear, leading to the discovery of radioactivity.

Inspired by Becquerel's research, Marie and Pierre Curie delved deeper into this phenomenon, examining various materials for evidence of radioactivity. They found that Uraninite exhibited stronger radioactivity than Uranium alone. This observation suggested the presence of additional radioactive substances. From this insight, they discovered two new elements: Polonium and Radium.

By 1910, Marie Curie successfully isolated Radium, confirming its existence as a distinct element. Her groundbreaking work paved the way for radiation studies, which continue to play a pivotal role in both research and industry to this day.

In 1909, Rutherford discovered alpha decay by measuring the mass-to-charge ratio, identifying the emitted particle as a ^{4}He nucleus.

By 1910, Rutherford proposed a model where the nucleus was envisioned as the central part of the atom. This model depicted the nucleus as a dense, positively charged core, surrounded by electrons in orbits, analogous to planets orbiting the sun in the solar system.

In the following year, Rutherford designed an experiment using a thin gold foil. He bombarded this foil with alpha particles and observed the scattering of these particles at various angles.

The results of the experiment were revealing. The fact that most alpha particles passed straight through the foil indicated that atoms were largely empty space. However, the deflection of some particles at large angles confirmed the presence of a dense, positively charged nucleus. In 1919, Rutherford achieved another milestone by performing the first human-made transmutation:

$$\alpha + N \rightarrow p + O$$

Proving nuclear reactions can transform one element into another.

By 1928, the theory of alpha decay had been described by Gamov [1] and Gurney [2]. They proposed that the alpha particle could move freely within a spherical region defined by the daughter nucleus. This concept suggested that the formation of the alpha particle was due to the excess energy within the nucleus.

Building on the momentum of these discoveries, 1929 saw another significant advancement in nuclear physics. The first cyclotron was constructed at the University of Berkeley in California. This innovation offered the capability to accelerate particles to higher energies than the existing Van de Graaff accelerators.

In 1949, Mayer and Jensen introduced the Shell model of the nucleus [3]. This model described how nucleons populate different shells, drawing an analogy to electronic shells in atomic physics and adhering to Pauli's exclusion principle. Within this model, nucleons can be individually excited, making quantised jumps between states. When they return to the state of minimal energy, they emit radiation. The Shell model proved particularly effective for describing closed shell nuclei.

By 1954, another significant contribution to nuclear physics came from Fred Hoyle. He postulated the existence of a resonant state in ^{12}C, formed by the combination of a ^{8}Be nucleus and an alpha particle. This state had an energy slightly above the alpha particle decay threshold [4]. This mechanism, known as the triple alpha process, involves a ^{8}Be nucleus capturing an alpha particle within 10^{-16} seconds of its formation. This results in a resonant state in ^{12}C, which exhibits greater stability as it decays through gamma emission [5].

In 1976, several new models of the nucleus emerged, including the collective models proposed by Bohr, Mottelson, and Rainwater [6][7][8]. These models posited that the collective motion of the nucleus's components determined its properties at various excitation levels.

Concurrently, as theoretical models were being proposed, experimental techniques underwent significant refinement. The field saw the invention of new tools to meet the growing demand for data. Discoveries of new materials led to the development

of more efficient and higher-resolution detectors [9][10]. Detection techniques grew increasingly sophisticated, and advances in computer science enabled the processing of vast amounts of data.

For a comprehensive understanding of nuclear physics from first principles, it's essential to grasp the components that constitute nucleons and, subsequently, their interactions. While there have been strides in studying the dynamics of quarks and gluons [11][12], these models are still in their infancy, both theoretically and experimentally. The systematic errors in these studies are currently too significant to align with the models. Most of these investigations can only account for very light nuclei (A$\leq$4) due to the immense computational power required for calculations.

Quantum Chromodynamics (QCD) has achieved remarkable progress in describing light to medium-sized nuclei, especially concerning inter-nucleon forces[13][14].

For nuclei ranging from medium to large masses, *ab-initio*[1] methods have been employed [15][16][17]. These methods have yielded results that align well with experimental data. Such calculations hold promise as tools for addressing long-standing challenges in nuclear physics [18].

There have been studies focusing in gamma emissions from clustered states [19] in medium mass nuclei where the structure of ^{28}Si was analysed by the energy and angles of gammas detected in the experiment.

There have been only two direct measurements exploring gamma emissions in light nuclei exploring the same concept of clustering as in this work, the first one in 2005 where Datar *et al.* [20] measured an electromagnetic transition probability in ^{8}Be nuclei, in 2013 this measurement was refined with a smaller uncertainty by the same group [21], showing it is possible to study the nuclear structure in light nuclei by gamma emission. The gamma branching ratio can be measured by indirect methods as the detection of heavy ions after a reaction [22][23][24]. Having a direct measurement of the branching ratios can give us information about the nuclear

[1] *ab-initio* refers to "from first principles"

structure by looking at the angular distribution of emission [25].

The aim of this work is to to make a contribution in the experimental data for electromagnetic transitions in clustered states in light nuclei, in specific in this work we study the ^{16}O nucleus.

The fisrt iteration of this experiment took place in 2015 where a first measurement was carried by Tz. Kokalova, C. Wheldon, J. Bishop, N. Curtis, M. Freer, R. Smith, D.J Parker and J. Walshe, this experiment did not yield favourable results as the experiment was not run for enough time and the target was too thick to let the particles of interest to be detected as the detectors were positioned at backwards angles.

In 2019 I built my first iteration of the experiment, with front facing Double-sided Silicon Strip Detectors (DSSDs) which allowed the detection of forward emitted particles to be detected as well as gamma rays. This run was a poof of concept in order to test the $\alpha - \gamma$ coincidence, as well as the use of a DSSDs telescope to eliminate particle contamination from protons from the chamber. This experiment had two distinct parts, one with a single DSSDs and one including a telescope array for light charged particle discrimination. This second experiment resulted in a branching ratio measurement with a large uncertainty given as the beam time only was around 8 hours in total. The experiment was performed by P. Santa Rita, Tz. Kokalova, C. Wheldon, N. Curtis with help of S. Pirrie, A. Hollands and R. Allen. This experiment helped to prepare a long measurement planned for spring 2020.

With everything ready to perform the experiment, the COVID-19 pandemic happened, delaying the experiment until August 2021. Once the experiment was setup again, the beam time was around 90 hours in order to gather enough detected events to extract a reasonable measurement for the gamma branching ratio for the reaction of interest.

Chapter 2

Theory

Physics is like sex: sure, it may give some practical results, but that's not why we do it.

-Richard P. Feynman

Nuclear physics is still an evolving subject, with the interpretation of experimental results requiring a mutual relation with theoretical models. This relationship allows theoretical models to predict observables and facilitate the designing of experiments while data from experiments generate information on how to test the models and improve the comprehension of the Universe at nuclear scales to create new models.

Experimental nuclear physics can be divided in two broad sections: **nuclear structure** and **nuclear reactions**.

The study of **nuclear reactions** focuses on how nuclei interact with each other by measuring observables such as energy, angles and cross sections of resulting particles after they interact. It is notable that two nuclei interacting might form a different set of particles after their interaction. The information gathered from these experiments provides insight into the behaviour of the nucleus following a perturbation.

The scope of **nuclear structure** studies is to understand the intrinsic structure

of excitation energy levels in nuclei by measuring the decay products. These measurements include the type of emissions, branching ratios, spin-parity and rates of decay. As these states are unique solutions to the Schrödinger equation, they give information about the potentials with which nucleons interact to form these states.

2.1 Nuclear reactions

A nuclear reaction is typically described by $a + X \rightarrow Y + b$ where a is a projectile particle incident on a target X. Particles Y, b are the recoil and ejectile resulting from the reaction respectively. Y is usually a heavier particle than b. In order for these reactions to take place, the projectile (with charge $\neq 0$) has to have enough kinetic energy to overcome the repulsion generated by the protons in the nucleus, this is known as the Coulomb barrier. To calculate the Coulomb barrier energy, a special case of the electrostatic potential energy is used as shown in equation 2.1:

$$U_{Coulomb} = \frac{kZ_1Z_2e^2}{r_0\left(A_1^{\frac{1}{3}} + A_2^{\frac{1}{3}}\right)}. \tag{2.1}$$

Where Z_1, Z_2 are the number of protons of the target nucleus and projectile, A_1, A_2 are the atomic masses of the target and projectile particles, e is the electron charge, k is the Coulomb constant $(\frac{1}{4\pi\epsilon_0})$ with ϵ_0 is the vacuum electric permittivity and $r_0 = 1.2 \times 10^{-15}$ m.

We can note the height of the Coulomb barrier increases with the atomic number, making it harder for heavier elements to overcome, requiring higher kinetic energies for the incoming particle.

There are many types of reactions ranging from transferring energy and momentum from one nucleus to another nucleus, others where the constituents of the nucleus completely change, reactions where particles are stripped from both target and incident nucleus.

To catalogue them, there are two main types of reactions, **direct reactions** and

compound nucleus reactions.

2.1.1 Direct Reactions

In direct reactions the interaction between the incoming particle and the target occur in the time frame of $\backsim 10^{-22}$ s only allowing only a few nucleons be able to interact. These types of reaction are more common when the energy of the projectile is higher than $\backsim 5$ MeV per nucleon and the interaction occurs on the outer layers of the nucleus rather than the inside volume.

In direct reactions, there can be an exchange of nucleons between the target and the projectile, these are called stripping and pick-up reactions. If the projectile can only transfer enough energy to the target to excite it to a greater energy level, the reaction is called inelastic scattering. If there is no energy transfer and both particles stay in their ground state after the reaction, it is elastic. In a knock-out reaction, the projectile can remove a single nucleon or a cluster of nucleons from the target. When a target is broken into two or more components due to the interaction with the projectile, it is called break-up reaction.

2.1.2 Compound Nucleus Reactions

The compound nucleus is a type of nuclear reaction where the projectile fuses completely with a target, usually stationary in the laboratory frame of reference. The time scale of these reactions is greater than in direct reactions ($\backsim 10^{-17}s$) allowing more nucleons to be involved in the interaction. Upon interaction, the nucleons reach a state of thermal equilibrium, rendering it impossible to discern the new nucleus from the constituents that contributed to its formation. This effect is known as the Bohr Independence hypothesis [26][27]. One of the consequences of this process is that the same compound nucleus can be formed using different targets and projectiles and the decay products of the compound nucleus are independent from the method to form it. The compound nucleus can decay into the same components

that form it or decay via other available process.

At excitation energies above the particle threshold and below the continuum, peaks in the cross section (see 2.1.3) of compound nucleus formation represent states of the newly formed nucleus. These peaks are called resonances and they are "quasibound" states in the compound nucleus. A diagram of this phenomenon is shown in figure 2.1.

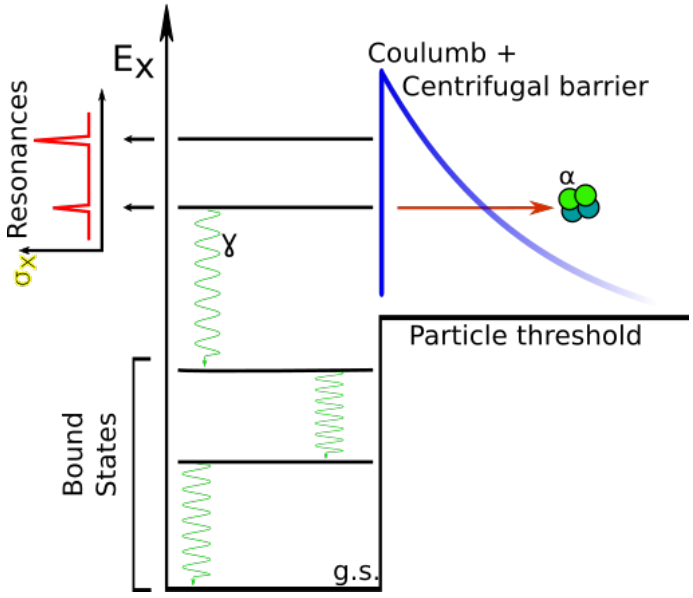

Figure 2.1: Resonances are quasibound states above the particle threshold, gamma decay is permitted to bound states in the compound nucleus.

If the compound nucleus decays into the same components that produced it, the product particles will have identical properties as an elastic scattering reaction.

2.1.3 Cross Section

The nuclear cross section, represented by σ_X, describes the likelihood of a specific reaction X occurring when a beam of incoming particles interacts with a target nucleus at a particular energy level. Essentially, it quantifies how "large" a target appears to the incoming particles, thereby determining the probability of an interaction.

In technical terms, the cross section σ_X establishes a relationship between two

quantities: N, the number of particles incident on a material per unit area per unit time, and R, the number of reactions taking place per unit time. This relationship is typically expressed in equation 2.2. The cross section has area units called barns[1] (1 barn = $10^{-28}\ m^2$).

$$\sigma_X = \frac{R(t)}{N(\theta, E)} \tag{2.2}$$

Various factors influence the cross-section, including:

- The type of incident particles: Different particles may interact differently with the target nuclei.
- The target nuclei: Different materials will have varying cross-sections due to differences in nuclear properties.
- The angle of detection: The angle at which particles are detected can affect the observed cross-section.
- The energy of the incident particles: The probability of reaction often depends on the energy level of the incoming particles.

The total cross-section represents the sum of all possible interaction probabilities for a given reaction. On the other hand, the differential cross-section provides a more detailed view, describing the likelihood of interactions based on specific angles or energy levels. To obtain a precise measurement of the total cross-section for a reaction, it's essential to conduct a thorough analysis across a broad spectrum of energies and detection angles.

[1]The story behind this name comes from the early days of nuclear reaction studies (circa 1942) where an experiment yielded an unexpected large value for uranium nuclei, Marshall Halloway and Charles Baker proclaimed over dinner "They are as big as a barn". The term was classified until 1948 where its use spread.

2.2 Nuclear Structure

To completely study the structure of the nucleus, it would be necessary to solve the Schrödinger equation for each specific system. However, this is analytically impossible[2] and the computational approach requires intensive calculations that require expensive infrastructure and it is not readily available just yet.

We can try start to understand the nucleus by looking at the two body system (nucleon_1, nucleon_2). The potential energy operator only depends on the relative positions of the particles. If we add another particle to the system, the potential energy operator will not only have contributions from their relative positions but from the interactions of the particles, this problem does not have an analytical solution (and we were only describing an interacting three particles system!).

At this point, another approach is needed, a new model that matches experimental results, predicts additional results and it reasonably easy to solve mathematically. This kind of approach is used in complex systems such as large [29] and small scale fluid dynamics [30][31], as well as biological systems [32], where it is impossible to measure all variables but a model can predict the evolution of the system.

One of the first attempts to describe the nucleus was the **liquid-drop model (LDM)** in which, a nucleus was thought as a droplet of nuclear material that could be deformed and even broken into smaller drops much like the coalescence system in fluid dynamics as shown in figure 2.2. This model proved unable to provide adequate explanation of all intrinsic nuclear phenomena, but it helps as a good approximation of the average behaviour of the nucleus, as the **LDM** is a classical model and does not include the quantum effects.

[2] Only seven problems in Quantum Mechanics have an analytical solution [28]

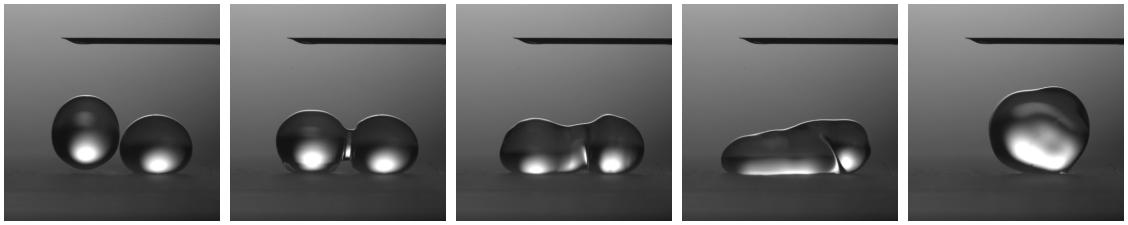

Figure 2.2: In the **liquid-drop model** the nucleus is equivalent to a droplet of liquid; in this figure we can see the evolution (left to right) of two droplets of water coalescing, analogous to two nuclei fusing. Or a nucleus fissioning if seen right to left.

One of the most notable result from this model is the **Bethe–Weizsäcker semi-empirical formula** for binding energy shown in equation 2.3, which is the difference between the mass of an atomic nucleus and the sum of the masses of proton and neutrons, $m = Zm_p + (A - Z)m_n - \frac{E_B(A,Z)}{c^2}$.

$$E_B = a_V A - a_S A^{2/3} - a_C \frac{Z(Z-1)}{A^{1/3}} - a_A \frac{(N-Z)^2}{A} + a_P A^{k_p} \delta_A(N,Z). \tag{2.3}$$

To understand this equation it is necessary to analyse the coefficient in each term:

- a_V Volume: If we imagine the nucleus as a droplet, the volume increases as the cubic power of the radius, the radius is proportional to the amount of nucleons.

- a_S Surface: The nucleons on the surface would have a weaker interaction with the nucleons inside the droplet, due to fewer nearest neighbours.

- a_C Coulomb: The repulsive force due to the proton charge interaction has an effect on the binding energy. The nuclear force acts in a smaller range than the electromagnetic force.

- a_A Asymmetry: this term takes consideration of the Pauli exclusion principle [33], having a different number of protons and neutrons implies that they must occupy higher energy levels.

- a_P Pairing: Pair of neutrons and protons tend to form, this configuration causes a more stable nucleon with an even number of nucleons due to spin coupling. The factor k_p in A^{k_p} is a specific coefficient for a given nucleus, and $\delta_A(N, Z)$ is a factor that describes the spin coupling effect. Depending on the nucleus this term is 0 or $\pm\delta_A$

A visual representation of each term can be seen in figure 2.3.

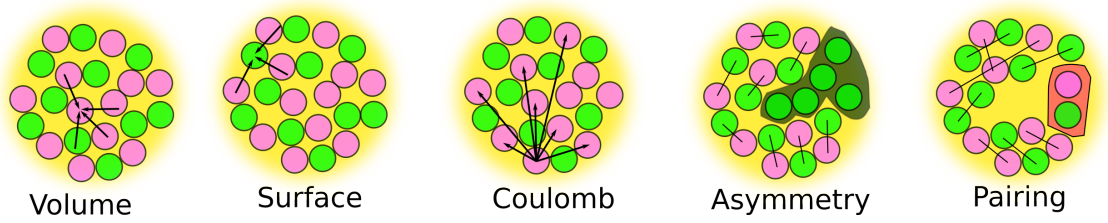

Figure 2.3: Visual representation of each coefficient contribution in the **Bethe–Weizsäcker semi-empirical formula**

Every component contributes to the mass difference; the asymmetry and the pairing terms are an attempt to model the quantum nature of the nucleus but the model is still considered a classical model. A better model that considers quantum effect is the **Shell model**.

2.2.1 Shell model

The shell model of electrons offers one of the most effective approaches to understanding atomic structure. Naturally, the idea of adapting a similar model to describe the nucleus is enticing. However, there are fundamental differences to consider. In atomic systems, the potential is externally provided, primarily by the nucleus. In contrast, within the nucleus, the potential is generated by the system itself. Additionally, while electrons in atomic orbitals have a relatively low probability of colliding with one another, nucleons in the nucleus face a different scenario. They are not only larger but also interact through both electromagnetic and strong forces. To adapt the shell model for the nucleus, these interactions, along with the

Pauli exclusion principle [33] — which states that no two nucleons can occupy the same quantum state — must be considered. The non-overlapping individual wave functions of nucleons mean that their interactions don't preclude the use of the shell model.

One can model the nuclear potential by assuming that the dynamics of an individual nucleon are governed by the potential created by all other nucleons, let us consider the potential of the shell model as an infinite well. This framework allows each nucleon to occupy distinct energy shells. Within this model, the primary mechanism for a nucleon to ascend in energy is to transition to higher shells. Such transitions require more energy than what nucleons can typically exchange within a shell. Consequently, nucleons orbit within their respective shells almost as if they are transparent to one another.

Supporting the shell model's applicability to the nucleus, experimental evidence can be observed when examining the experimental data for binding energy per nucleon when compared to the binding energy predicted in the **LDM**, as depicted in figure 2.4:

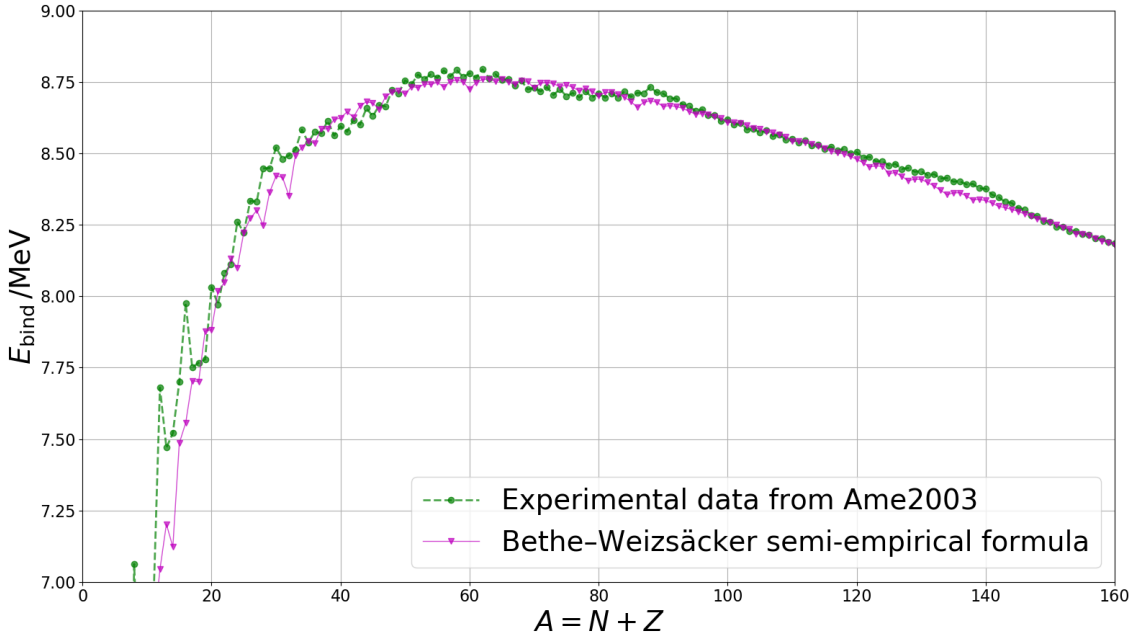

Figure 2.4: We can see a difference between data from reference [34] and the Bethe–Weizsäcker semi-empirical formula 2.3. Notably, we can see peaks at certain masses, hinting there are more stable configurations than others, the so called **magic numbers**.

The binding energy per nucleon is strikingly similar to the ionisation energy in the atomic system.

Major discontinuities in the plot in figure 2.4 hint at the "filling" of principal shells, the **magic numbers(2, 8, 20, 28, 50, 82, 126)** represent completely filled shells. The filling of these shells depend on the Pauli exclusion principle [33].

A better shell model

Until this moment we assume an infinite potential which would require an infinite amount of energy to remove one nucleon. To improve our model we require a better radial approximation for the potential. We know that the potential must tend to zero if the distance of a nucleon from the nucleus goes to infinity. The potential must tend to a minimum at $r = 0$, otherwise nucleons would not form bound states. With these constrictions we use the Woods-Saxon potential:

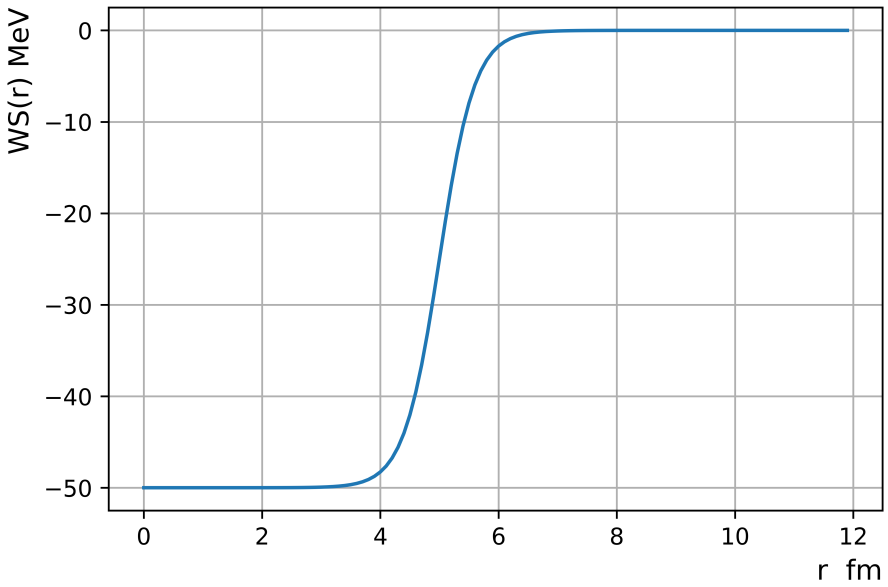

Figure 2.5: Wood-Saxon potential with a depth $V_0 = 50$ MeV, radius $R = 5$ fm and diffuseness parameter a =0.3 fm

$$V_{WS}(r) = \frac{-V_0}{1 + exp\left(\frac{r-R}{a}\right)} \tag{2.4}$$

Where V_0 is the potential well depth and R is the radius of the nucleus, and a is the diffuseness parameter which can be interpreted as the "thickness" of the nucleus surface. These parameters can be extracted from experiments. The shape of the potential is shown in figure 2.5.

This is a better approximation of our nucleus but still fails to explain the complete nuclear phenomena seen experimentally. We have not considered spin-orbit nucleon interactions. This idea of another type of interaction inside the nucleus that is supported by data from scattering experiments [35].

The spin-orbit interaction adds a term to the nuclear potential in the form $V_{\text{LS}} = \lambda \mathbf{L} \cdot \mathbf{S}$, where $\mathbf{L}$ is the orbital angular momentum operator, $\mathbf{S}$ is the spin operator, and λ is a coupling constant. The spin-orbit interaction causes the splitting of energy levels for nucleons with the same principal quantum number but different total angular momentum I, where $I = L \pm \frac{1}{2}$. This leads to the formation of subshells and a more nuanced shell structure, closely aligning with observed nuclear

properties.

The incorporation of the spin-orbit interaction in the shell model is essential for explaining key experimental observations, such as the magic numbers and the detailed structure of nuclear energy levels. Without this interaction, the model predicts degenerate energy levels for different l values, contradicting experimental data. The spin-orbit term introduces a fine structure into the nuclear energy levels, lifting the degeneracy, and leading to better agreement with observed spectra. Moreover, the spin-orbit coupling provides insights into nuclear magnetic moments and electric quadrupole transitions, as it relates to the alignment of the nucleon's spin with its orbital motion. By incorporating this complex interaction, the shell model becomes a powerful tool in nuclear physics, capturing essential features of the nuclear force and offering a sophisticated description of nuclear structure and behaviour.

With these additions to the model, we can note that some energy levels split to fill the lower shell and with this correction the model starts to make better predictions for energy levels and magic numbers. In figure 2.6 a diagram of the shells is shown.

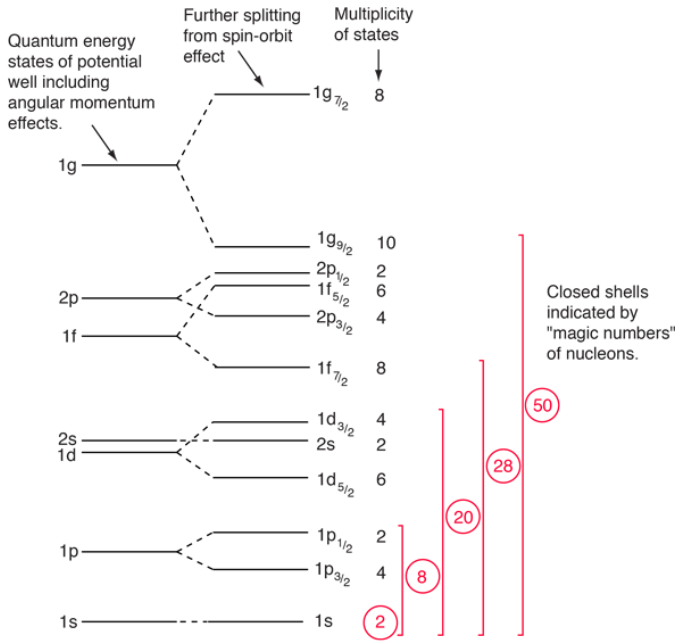

Figure 2.6: Example of the shell model where different energy levels (shells) are shown, as well as, its splitting considering spin-orbit interactions. It is noticeable how the filling of shells give rise to the **magic numbers**. Image taken from [36]

This model is good for nuclear masses A<150 and 190<A<220, as in these ranges the nucleons occupy well-defined energy levels and fill up the available shells; however outside these range, there are particles that are not closed shells which act as valence nucleons and these particles can influence the nuclear structure and properties, such as the nuclear shape, nuclear stability, and the way nuclei interact in reactions. The interaction between valence particles in different nuclei can lead to the formation of nuclear isotopes, isomers, and the understanding of phenomena like nuclear binding energies and nuclear reactions.

One of they key successes of the shell model is the good agreement with data from ground state spin-parity measurements.

There are nuclei for which the shell model is not a good approximation, as most of the shell model predictions are based on the unpaired nucleons which give the nucleus its properties.

The properties of these nuclei can be thought as collective motion of all its constituent nucleons, for even-Z and even-N nuclei we see properties that can be explained by thinking of the nucleus as collective vibrational and rotational modes of a deformed sphere.

A model that can predict the properties of the nucleus independently of the mass is still needed as both the shell and collective models are idealisations of the nucleus and do not consider the intrinsic interactions of the nucleons. In these models the dynamics of the nucleus are dictated by the position and collective behaviour of their constituents.

More recent models are usually a combination of several models including the shell model [37][38], deformations models [39], *ab-initio* calculations [40], chiral effective field theories [41], and Monte Carlo methods [42]. These new approaches are providing improved predictions and adjust well to new experimental data.

Another model through which the nucleus can be described is as a cluster of sub-elements, in particular, alpha particles. The idea of clustering was hinted at

the observation of alpha decay, because this meant an alpha particle was preformed within the nucleus before emission, implying there must be some sort of substructure [43] when thinking of the Gamov model for alpha decay.

This mentality would mean that certain types of nuclei such as ^{8}Be,^{12}C,^{16}O... could be described solely by the clustering of alpha particles. ^{4}He nuclei (alpha particles) show a higher binding energy (28.3 MeV) than their N $\neq$ Z nuclei neighbours. This leads to intrinsic shapes of the clustered nuclei.

2.2.2 Nuclear clustering

In early nuclear cluster theory, the proposed nuclear shapes were simple geometric crystal-like structures. As time passed the description of the nucleus became more complex due to the more rigorous quantum mechanics description as well as the computational power available to carry out model calculations. Although the nuclear shell model has had incredible success, clustering does not arise from it and it is more related to more standard nuclear deformations [44].

Experimental techniques also evolved, leading to more precise measurements. The combination of these developments continues to give us a better understating of the nuclear structure.

Hafstad and Teller [43] found that there is a linear correlation between the binding energy and the number of bonds in the most compact geometric configurations in the alpha conjugates. The possibility of compact ground states led Ikeda *et al.* [45] to reason that the level of clusterisation increases as the energy of the nucleus increases. This idea is captured in figure 2.7 also known as an *Ikeda diagram*.

This effect is caused because the difference in masses between the nucleus and the free alpha particles is regained. He predicted the ^{16}O could exhibit ^{12}C+alpha structures above the corresponding alpha decay threshold at 7.16 MeV or even, at higher excitation energies (>14.44 MeV) exhibit four alpha structure.

The so-called "$core + \alpha$" model is supported by the work of Brink and Castro

in reference [46] in which they predict that the phase change from neutrons and protons, to core+alpha, occurs when the nuclear mass density falls bellow 1/3 of its normal value.

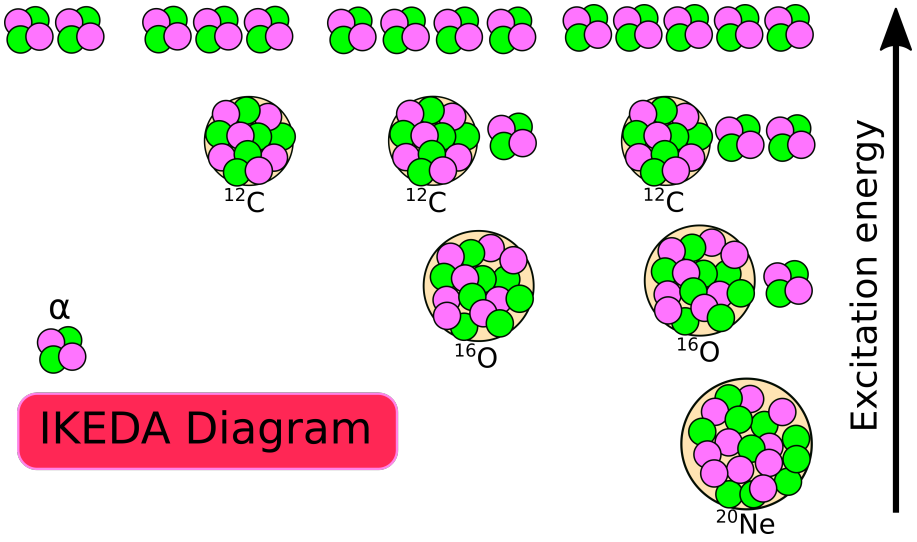

Figure 2.7: Ikeda diagram showing the idea of clusterisation in nuclei.

More modern developments include calculations for electromagnetic transition rates for these vibrational and rotational models using the Skyrme formalism [47][48][49]. Models for ^{16}O still need input from experimental data to improve their predications.

2.2.3 Rotational Bands

A rotational band is a series of nuclear states connected by their relation between energy and angular momentum as well as their similitude in shape. In order to associate nuclear states to rotational bands it is necessary to perform experiments that provide us with information about the energy of nuclear states and their angular momentum. In figure 2.8, this association is shown for ^{16}O nucleus.

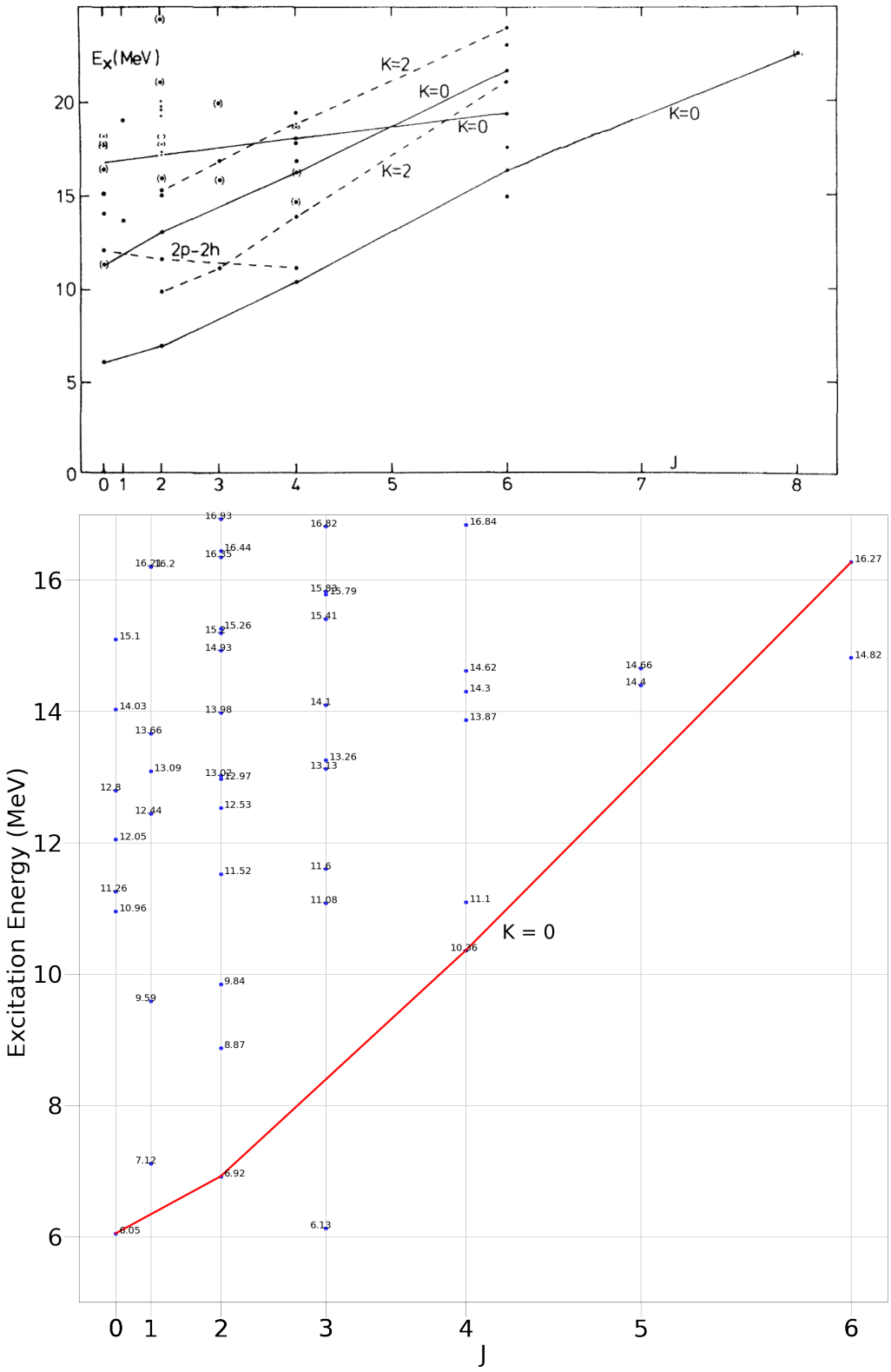

Figure 2.8: Top: Experimental rotational bands from the ^{16}O nucleus taken from reference [50]. Each dot represents an excited state, the lines connecting the states show the relationship between these states *i.e.* the rotational band they are part of. The linear trend they exhibit is noticeable, following equation 2.5.
Bottom: A more detailed version of the graph, where the line in red represents the rotational band of the states studied in this work

The idea of rotational bands was first generated in the fifties by Bohr and Mottelson [51][52][53][54]. The nucleus can be seen as a collection of sub-elements, these sub-elements can present coherent movement and one of the possible degrees of freedom is rotation as a group.

The idea can be understood using non-quantum models due to the similarities with the classical rotor. An important notion, is that rotational excitation in quantum mechanics cannot be defined for a symmetry axis because this would only represent a shift in phase of the wave function.

One of the first attempts to connect the ideas of clusterisation and rotational bands was made by Morinaga in reference [55]. This work predicts the connection for the 0^+ band-head state at 0^+ at 6.06 MeV, and how the 2^+ state at 6.91 MeV should lie close in energy in the ^{16}O nucleus. Only deformed (non-spherical) nuclei can have a moment of inertia in the quantum mechanical description and can be described using only one total moment of inertia. The eigenvalues for the rotational Hamiltonian $\hat{H}_{rot} = \frac{\mathbf{R}^2}{2\tau}$ are:

$$E_I = \frac{\hbar^2}{2\tau} I(I+1) + E_0, \tag{2.5}$$

where $\mathbf{R}$ is the collective angular moment operator [56], τ is the moment of inertia and it depends on the shape and internal structure of the system as well as the axis of rotation, E_I is the eigenenergy of the state, E_0 is the energy of the first element in the band (band head) and I is the angular momentum of the state. The moment of inertia can be calculated by measuring the energies of a rotational band's energy states, and this information can then be used to infer the properties of the rotational band.

The ^{16}O nucleus has closed proton and neutrons shells, meaning that the expected symmetry is spherical, but as the nucleus starts to excite, the degeneracy is broken and one way to describe it is by seeing it as a deformed spheroid (as shown in figure 2.9).

In the case of ^{16}O, E_0 is 0 MeV for the ground state rotational band as the nucleus is even-even. In the ground-state rotational band only even spins are observed and the wave function can be expressed as $\Psi(J,K,M) \propto \mathscr{D}(\alpha,\beta,\gamma)[1+(-1)^J]$, where $\mathscr{D}$ is the function of collective motion and it depends on the Euler angles which describe the orientation of a body in space based on its rotations. For a rotational symmetric nucleus, only two of these angles are required.

The expected decay cascade is $8^+ \rightarrow 6^+ \rightarrow 4^+ \rightarrow 2^+ \rightarrow 0^+$ [56] and this has been proved up to the 6^+ state [57].

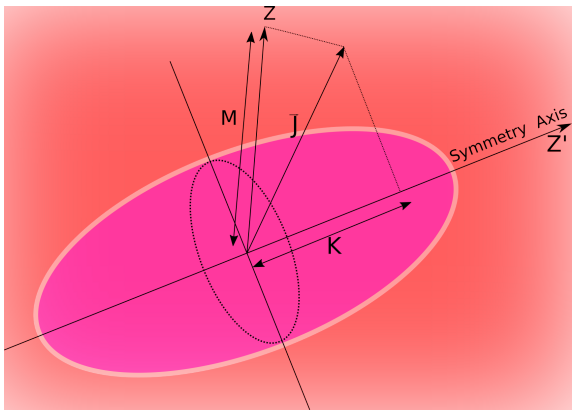

Figure 2.9: Approximation of a deformed nucleus with the symmetry axis in Z'. $\vec{\mathbf{J}}$ is the total angular momentum, K is the projection on the symmetry axis and M is the projection of $\vec{\mathbf{J}}$ on the laboratory axis Z.

To study the properties of a nucleus it is necessary to "dissect" the nucleus using the right probe. These probes are the emissions from the excited nucleus including alpha particles, electrons, positrons, gamma radiation and neutrons. In this work, the focus is the detection of gamma rays and the alpha particles emitted from an excited state in ^{16}O.

2.3 Gamma Emission

Gamma emission occurs when a nucleus in an excited state emits a photon, typically in the 0.1 to 10 MeV energy region. This phenomenon is caused by the change in the electromagnetic field generated by nucleons, due to nuclear excitations.

To study this phenomenon it is useful to utilise the multipole momentum description of the charge distribution. Radiation of electromagnetic fields can be explained by electromagnetic fields by varying the multipole moments, as from electromagnetism it is clear that different multiple orders will have different angular distribution. Thus, through measurement of the angular distribution of the emitted radiation, the multipole order of the emitted radiation can be identified. Taking L as the index of the multipole radiation such as 2^L is the order of the multipole ($L = 1$ is dipole, L=2 quadrupole, etc.).

The $2^L - pole$ radiation emission can be explained by the Legendre polynomials in a convenient frame of reference, it is important to note that when two or more gamma rays are emitted consecutively, the relation becomes more complex as explained in D. Hamilton's work in reference [58]. The probability of decay is described in quantum mechanics by the matrix element of the multipole operator between the element I_i and I_f:

$$m_{fi}(\sigma L) = \int \Psi_f^* m(\sigma L) \Psi_i dv = \mid \langle E_f J_f m_f \mid m(\sigma L) \mid E_i J_i m_i \rangle \mid^2, \tag{2.6}$$

where σ denotes the type of transition, E for electric, M for magnetic and L represents the multipole of the transition. The radiated power from a multipole is:

$$P(\sigma L) = \frac{2(L+1)c}{\epsilon_0 L[(2L+1)!!]^2} \left(\frac{\omega}{c}\right)^{2L+2} [m_{fi}(\sigma L)]^2, \tag{2.7}$$

where $m(\sigma L)$ is the amplitude of the electric or magnetic moment and each emitted photon has energy $\hbar\omega$. Thus, dividing equation 2.7 by the energy of each photon leads to the probability per unit of time for photon emission:

$$\lambda = \frac{P(\sigma L)}{\hbar\omega} = \frac{2(L+1)c}{\hbar\epsilon_0 L[(2L+1)!!]^2} \left(\frac{\omega}{c}\right)^{2L+1} [m_{fi}(\sigma L)]^2 \tag{2.8}$$

To simplify the calculation, an assumption can be made that the transition is due

to a single proton moving from one state to another in the shell-model description, and that the radius of the nucleus can be approximated by $R = R_0 A^{\frac{1}{3}}$. These simplifications lead to the Weisskopf single-particle estimates and they are used to provide an estimate of the rate of the electromagnetic transitions, instead of a pure theoretical calculation. The estimates have two major conclusions:

1) Lower multipole transitions are dominant,

2) Electric transitions are more likely to happen than magnetic for the same multipole order.

Measuring the energy and the decay rate of the gamma rays is not enough to extract all the information from the nuclear state that generated the gamma ray, as the emission is not only governed by the Legendre polynomials but also by spherical harmonics, meaning the measurement of the angular distribution of these gamma rays can provide information about the order of the multipole transition.

In the classical multipole radiation description, oscillating charges and currents can transmit energy and angular momentum. In the quantum description this is also true but for the angular momentum transfer the emitted photon needs to carry a definite angular momentum. For the multipole operator of order L the angular momentum transferred is $L\hbar$. This can be explained through the $Y_{LM}(\theta, \phi)$ term which is associated with the angular momentum.

From the conservation of total angular momentum the initial angular momentum I_i is equal to the total angular momentum transferred, L, plus the angular momentum of the final state I_f:

$$\vec{\mathbf{I_i}} = \vec{\mathbf{L}} + \vec{\mathbf{I_f}}, \tag{2.9}$$

where the vectors I_i, I_f and L need to form a closed triangle, meaning that the values of L are restricted. The biggest value L can take is $I_i + I_f$ and the smallest value is $|I_i - I_f|$.

To determine the type of emitted radiation the relative parity of the initial and final state is needed. If the parity does not change then the parity of the transition must be even. On the other hand if the parity changes, the transition is odd. Electric and magnetic transitions of the same multipole order have different parities:

$$\pi(ML) = (-1)^{L+1},\ \pi(EL) = (-1)^{L}.$$

By knowing this result, selection rules for electromagnetic transitions can be obtained:

$$|I_i - I_f| \leq L \leq I_i + I_f$$

$$\Delta\pi = no\ \&\ L_{even} : \text{Electric},\ L_{odd} : \text{Magnetic}$$

$$\Delta\pi = yes\ \&\ L_{odd} : \text{Electric},\ L_{even} : \text{Magnetic}$$

Until now it is supposed that $L \neq 0$ thus excluding monopole transitions. In the case where $I_i = I_f = 0$ there are no possible electromagnetic transitions. However there exist a few even-even nuclei that have 0^+ first excited states which according to the selection rules cannot decay by emitting a gamma ray. These states instead decay though a process called internal conversion or if the excitation is above the energy threshold of $2\mathrm{m_e c^2}$ a pair of electron-positron can be emitted.

Electromagnetic fields from the excited nucleus can excite the electrons in the atom shells, and this process can de-excite the nucleus. The excitation can lead to electromagnetic emission from the atom which will be X-rays from weakly bound electrons filling the vacancy in the inner shell.

While internal conversion will be a possible de-excitation channel for all excitation states, it is most favoured for low-energy transitions and when no other possible decay is possible *i.e.* below particle emission threshold or for $L = 0$. Consider as an example, the first energy excited state in ^{16}O at 6.049 MeV with $J^\pi = 0^+$. The Q-value for alpha emission is -7.161 MeV, while for proton and neutron emission

the values are -12.127 MeV and -15.663 MeV respectively. The ^{16}O nucleus cannot decay via gamma emission as $I_i = I_f = 0$. This state can either de-excite by emitting a high energy electron from the atomic shell or, much more probably, by emitting an electron-positron pair.

To calculate the effect of internal conversion of a given gamma transition it is common to calculate the Internal Conversion Coefficients which are measure of the contribution as a fraction of internal conversion for a given gamma transition. If we are studying a gamma transition of 5.9 MeV from an excited state in ^{16}O and use the calculator provided by reference [59] we can see that only a 1.728×10^{-3} fraction of the total gamma rays emitted would arise from internal conversion. As this effect is relatively low compared to the gamma emission, calculations for the Transition probabilities will not be considered, for further calculations on this work.

2.3.1 Experimental Electromagnetic Transition Probabilities

The total transition probability $P(level)$ of a nucleus is defined as the sum of the possible transition probabilities P_d, including electromagnetic and particle emission as:

$$P(level) = \sum_d P_d \tag{2.10}$$

For a specific excited energy level with mean life τ (s), the transition probability is:

$$P(level) = \tau^{-1} \tag{2.11}$$

The partial gamma transition probability $P_\gamma(\sigma L)$ is a calculation connecting the total transition probability $P(level)$ and the relative intensities of the possible channels of decay:

$$P_\gamma(\sigma L) = P(level)\frac{N_\gamma(\sigma L)}{\sum_d N_d}, \tag{2.12}$$

where $\sum_d N_d$ is the sum of every possible transition probability decay channel normalised with the intensity of the transition intensity N_γ we are calculating. To calculate the reduce transition probability which are defined only for gamma transitions of a certain multipolarity B(σL):

$$B(\sigma L; I_i \to I_f) = \frac{L[(2L+1)!!]^2\hbar}{8\pi(L+1)} \left(\frac{\hbar c}{E_\gamma}\right)^{2L+1} P_\gamma(\sigma L; I_i \to I_f) \tag{2.13}$$

where E_γ is the energy of the gamma ray in MeV, $B(\sigma L; I_i \to I_f)$ is in $e^2(fm)^{2L}$ and the decay rate $P_\gamma(\sigma L; I_i \to I_f)$ is in s^{-1}. This work is focused on transitions of the type E2. For completeness, a table of $B(\sigma L; I_i \to I_f)$ for both **E**lectric and **M**agnetic transitions at different multipolarities is presented. More tabulated values can be found in reference [60].

$$B(E1; I_i \to I_f) = 6.288 \times 10^{-16} E_\gamma^{-3} P_\gamma(E1; I_i \to I_f)$$
$$B(E2; I_i \to I_f) = 8.161 \times 10^{-10} E_\gamma^{-5} P_\gamma(E2; I_i \to I_f)$$
$$B(E3; I_i \to I_f) = 1.752 \times 10^{-16} E_\gamma^{-7} P_\gamma(E3; I_i \to I_f)$$

$$B(M1; I_i \to I_f) = 5.687 \times 10^{-14} E_\gamma^{-3} P_\gamma(M1; I_i \to I_f)$$
$$B(M2; I_i \to I_f) = 7.381 \times 10^{-8} E_\gamma^{-3} P_\gamma(M2; I_i \to I_f)$$
$$B(M3; I_i \to I_f) = 1.584 \times 10^{-1} E_\gamma^{-3} P_\gamma(M3; I_i \to I_f)$$

One can imagine a state that can decay by emitting one gamma by an E2 from a 6^+ to 4^+ transition or one alpha, equation 2.12 then looks like:

$$P_\gamma(E2) = \frac{P(level)}{\frac{N_\gamma}{N_\gamma} + \frac{N_\alpha}{N_\gamma}} \tag{2.14}$$

It is notable that if the intensity of measured gammas N_γ is relatively small compared to the intensity of measured alphas N_α, the total $P_\gamma(E2)$ will decrease and so the B(E2). Then the reduced transition probability then looks like:

$$B(E2; 6 \to 4) = 8.161 \times 10^{-10} E_\gamma^{-5} P_\gamma(E2; 6 \to 4) \tag{2.15}$$

These equations connect the experimental values (intensities N_γ and N_α) with the values from theoretical calculations. One common method to compare the experimental and theoretic values is the factor F defined in equation 2.16, A value close to one would show a good agreement between experiment and theory, this factor is useful to compare between different models.

$$F = \frac{B(\sigma L)_{experiment}}{B(\sigma L)_{theory}} \tag{2.16}$$

It is common to report reduced transition probabilities in Weisskopf units, to calculate this we divide the measured value by the corresponding value in energy, multipolarity and type of transition Weisskopf estimate, this also helps to measure the "collectiveness" of a transition as a large number would indicate more particles were involved in the transition rather than the single nucleon de-excitation Weisskopf consideration.

2.3.2 Gamma Emission from Clustered states

In a clustered state, more particles are involved in the emission of a gamma ray, as the charge inside the nucleus produces a deformed electromagnetic field. This results in an enhancement of the probability of decay by emission of gamma rays.

Until now, gamma emission has only been considered as the result of the deexcitation of a single nucleon. However, in clustered states single nucleon can not be in excited states as they are part of the formed alpha particles that forms the deformed nucleus. The deformation of the nucleus causes a rearrangement of the electromagnetic field within the nucleus, meaning that if the nucleus were to decay by gamma emission, more particles are involved in the transition making the transition stronger and increasing the probability of decaying by gamma.

In the microscopic view of the wave function, a collective state is the superposition of many single particle wave functions with their phases in correlation. The

strengthening of the collective transition probability is caused by the effect of the phase correlation between single particle wave functions.

To exemplify this enhancement, an example is taken from reference [60], two simplifications will be assumed:

- We consider a collective state to be a mixture of four single particle wave functions with equal amplitudes:

$$a_1 = a_2 = a_3 = a_4 = 0.5 = \sqrt{0.25}; \qquad \sum_{i=1}^{4} a_i^2 = 1 \tag{2.17}$$

- The gamma-ray matrix elements corresponding to the reduced single particles between the initial and the final states are equal to $\langle E_f J_f m_f | \, m_{s.p.}(\sigma L) \, | E_i J_i m_i \rangle$.

With these simplifications and having the phase in correlation:

$$m_{fi}(\sigma L) = (2I_f + 1)^{-1} | 4 \times 0.5 \, \langle E_f J_f m_f | \, m_{s.p.}(\sigma L) \, | E_i J_i m_i \rangle \, |^2. \tag{2.18}$$

$$m_{fi}(\sigma L) = 4(2I_f + 1)^{-1} | \, \langle E_f J_f m_f | \, m_{s.p.}(\sigma L) \, | E_i J_i m_i \rangle \, |^2. \tag{2.19}$$

From equation 2.19 we can see a 4 fold enhancement of the transition probability in this example.

Although there is an enhancement in collective transitions, the theoretical calculations are completely dependent on the overlap of the initial and the final wave functions which are model-dependant.

2.4 Interaction of gamma-rays with matter

There are three major different ways gamma radiation can interact with matter: **Compton scattering** happens when the gamma ray is scattered by an atom and a recoil electron is produced, the resulting gamma ray and electron share the original energy of the incident gamma ray which allow further interactions with the material.

In **photoelectic absorption** the gamma ray is completely absorbed and a *photoelectron* is ejected by the outer shells from the atom, with the kinetic energy of this photoelectron being equal to energy of the original gamma ray minus the binding energy of the photoelectron to the original shell.

When the gamma rays have energy greater than 1.022 MeV they can create a pair of electron-positron by converting some of its energy into matter through a process called **pair production**. After an electron-positron pair is created; the left over energy from the original gamma ray is divided into the pair as kinetic energy and the recoil nucleus. For most practical calculations, especially in thick materials where multiple interactions happen, the energy taken by the recoiling nucleus is often negligible. However, in precision experiments or certain applications, it would need to be taken into account. After the positron losses its energy due to electromagnetic interactions and comes to rest it annihilate with an electron, producing a pair of opposite co-linear 0.511 MeV gamma rays.

The type of interaction depends on the Z number of the absorber and the energy of the incident gamma ray. In figure 2.10 the relative areas where each interaction are more dominant is shown.

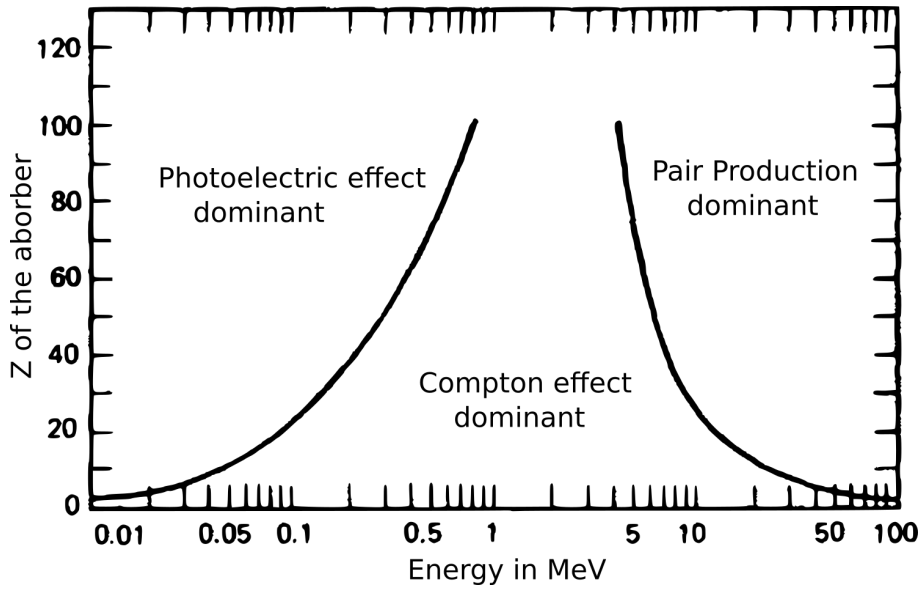

Figure 2.10: Figure adapted from reference [61], the lines separating areas show where the probability of interaction of a given interaction is equal

2.5 Detection Efficiency

Efficiency is defined as the conversion of some type of *event* into another type of *event*. In our case, detection efficiency is the ratio of conversion between the emitted particles by a nuclear reaction to detection in an experiment. The detection efficiency depends on several factors including: the materials of the detector, its geometry, type of radiation, energy and possible interactions.

In section 2.4 the specific mechanism of how gamma rays can possibly interact with a material and producing secondary emissions that can lead to its detection (this is further discussed in the next section). But not all of these gamma rays will interact with the material though, some will just traverse the volume of the material without interacting thus not being detected. The detection efficiency is divided in two sections, the absolute efficiency:

$$\epsilon_{abs} = \frac{\text{particles detected}}{\text{particles emitted}} \tag{2.20}$$

and the intrinsic efficiency:

$$\epsilon_{int} = \frac{\text{particles detected}}{\text{particles incidents on the detector}} \tag{2.21}$$

These quantities are related by a geometric factor shown in equation 2.22, the division between the full coverage of a sphere containing the material emitting the rays and the solid angle covered by the material used as the detector Ω, usually the emitting material is small enough to be considered as a consider it as a point in space.

$$\epsilon_{int} = \epsilon_{abs} \times \frac{4\pi}{\Omega} \tag{2.22}$$

These quantities allow us to calculate the number of particles that were emitted by a source or a nuclear reaction by extracting the number of detected particles in an experiment.

2.6 Gamma spectroscopy

The study of the energies and cataloguing of gamma rays is called gamma spectroscopy, the tools to study them involve techniques called detectors and as discussed in section 2.4, gamma rays can interact with matter in three distinct ways. In certain materials the secondary emissions can be detected and then converted into organised data to investigate the origin of the gamma rays, these materials are perfect candidates to become detectors.

In an experiment the choosing of the detector is crucial, as the geometry and the chemical composition are critical to maximise the efficiency of measurement. The type of interaction will produce different responses in a detector. In section 3.5 the specific mechanism of detector of our array is discussed.

The photoelectric effect will produce a single electron from interacting with an atom from the detector, if we were to measure the energy distribution of these electrons after a mono-energetic beam of gamma rays, it will produce a single peak in its energy spectrum, as all of the energy from the incident gamma is converted into kinetic energy for the recoil electron. This type of interaction usually occurs at very low energies of the incident gamma ray.

Compton scattering will produce a continuum spectrum of detected energies as all angles are possible for the recoil electron. This feature in the spectrum is called Compton continuum. By conservation of energy and momentum we can calculate the energy of the gamma ray after the interaction, as shown in equation 2.23:

$$E^{'} = \frac{E_0}{1 + \left[\frac{E_0}{m_e c^2} \times (1 - \cos(\theta))\right]} \tag{2.23}$$

where $m_e c^2$ is the resting mass of the electron, E_0 is the original energy of the gamma ray, $E^{'}$ is the energy of the scattered gamma and θ is the angle at which the electron was emitted. We can note two interesting results from this equation:

When $\theta \approx 0$, the recoil electron is left with almost no energy and the scattered

gamma will have most of the energy from the original gamma ray. This gamma ray is likely to interact again with another atom in the material. The case $\theta \approx \pi$, is when the recoil electron takes the maximum energy that can take from the interaction leaving the secondary gamma ray with less energy.

The recoil energy of the electron is given by: $E_e = E_0 - E'$. At $\theta \approx \pi$, the electron takes all the possible transferable energy from the interaction, this will manifest in the detected energy spectrum (see figure 2.11) as the end point for the Compton continuum and it is called the Compton edge. The difference between this feature and the *full energy peak* when the energy of the incident gamma is much greater than $m_e c^2$ tends to a constant value of 0.256 MeV.

Pair production, on the other hand will manifest in a detected energy spectrum as one extra or two extra peaks separated from the full absorption peak to a distance of 0.511 MeV and 1.022 MeV, depending on the actual size of the detector, a small detector is more likely to let both peaks escape where as in a medium or big sized detectors, these gamma rays have more volume to interact and be detected.
If only one of these secondary gamma rays escape is called a *single escape peak* and if both escape its called a *double escape peak*. When the total energy of the gamma is absorbed by the detector it is called a *full energy peak*.

Detection of gamma rays involves a usually involves a combination of these effects.

A typical energy spectrum considering all of the interactions discussed is shown in figure 2.11, where we can notice how multiple interactions can happen in the detector.

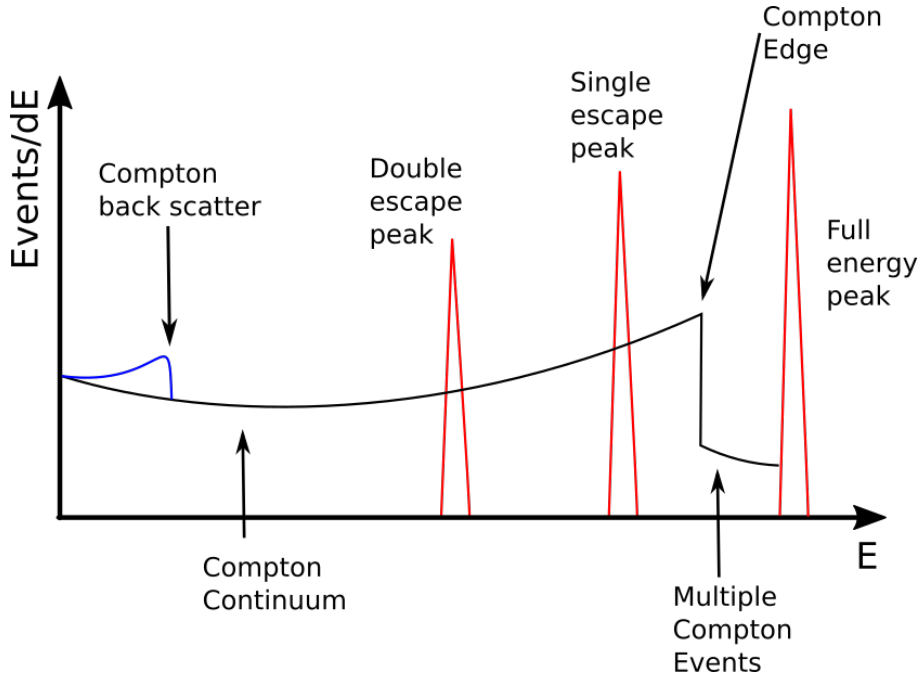

Figure 2.11: Representation of a typical gamma spectrum in a medium sized detector.

Another interaction that can affect our spectrum is Compton back-scatter, when gamma rays are scattered outside the detector and then scattered back into it, they will produce a feature in the spectrum around 200 keV, but it does depend on the initial energy.

2.7 Alpha Emission

This is one of the possible process a nucleus can undergo to de-excite itself. Classically, alpha emission is forbidden, but now is known to be possible through quantum tunnelling. Alpha particles are good candidates to release energy from an excited nucleus due to the relatively high binding energy compared with its neighbouring nuclei. In order for alpha to escape the nucleus it needs to overcome the Coloumb repulsion.

The Q-value for alpha emission is greater than other possible decay channels (proton, neutron, other helium isotopes, etc.), other types of particle disintegration

are possible but the probability is low compared with the alpha disintegration.

The energy of the alpha particle is dictated by the final state in which the daughter nucleus is populated, in alpha spectroscopy this is noted by α_0 if the ground state is populated, α_1 if the first excited state is populated and so on.

Identifying the populated states in the daughter nucleus is no easy task and it takes some detective work usually in combination with other techniques such as correlated particles, time of flight, and gamma spectroscopy to extract all the possible information about the excited nucleus.

2.8 Interaction of Charged particles with matter

Charged particles mostly interact by Coulomb forces with matter, as when a particle enters an absorbing medium, it will immediately be affected by the field generated the electrons of its atoms. Depending on the proximity of the charge particle to the atoms in the material and the energy, the electrons can be excited or completely ripped from the atom. This energy transfer slows down the particle and if there are enough collisions the particle can be stopped and absorbed entirely.

It is possible for charged particles to go through an absorber medium without losing all of its energy, but it does depend on the original energy of the charged particle, the atomic number of the material and its thickness.

The energy loss of a particle going though a medium can be studied using the Bethe-block semi-empirical formula:

$$-\left\langle \frac{dE}{dx} \right\rangle = \frac{4\pi}{m_e c^2} \cdot \frac{nz^2}{\beta^2} \cdot \left(\frac{e^2}{4\pi\varepsilon_0} \right)^2 \cdot \left[\ln\left(\frac{2m_e c^2 \beta^2}{I \cdot (1-\beta^2)} \right) - \beta^2 \right] \tag{2.24}$$

where x is the distance travelled in the medium by the charged particle, E is the energy of the particle, $\beta = \frac{v}{c}$, c is the speed of light in vacuum, m_e is the mass of the electron, e is the charge of the electron, n is the medium density I is the mean

excitation potential[3] and ϵ_0 is the vacuum permittivity. In reality this formula is only an approximation, and to calculate accurately the energy loss experienced by a charged particle in a medium, tables of experimental data and computational approximations are used.

Charged particle detectors increase their efficiency with their volume as the probability of the particle to deposit all of its kinetic energy within the material increases with the length of the material. But in there is a limit on how big a detector can be before other effects affect the detection of charged particles.

Let us consider gas detectors such as proportional counters or Geiger-Müller [61] by creasing the volume of the detector generally increases the probability that a charged particle will interact within the detector, thereby increasing the efficiency. However, if the detector becomes too large, issues like longer electron drift times, increased capacitance, and other factors can degrade the signal-to-noise ratio or the detector's timing resolution.

In Scintillation Detectors, a larger volume of scintillating material increases the likelihood of a charged particle interacting and producing scintillation light, which can increase efficiency. But, larger volumes might also mean that some of the produced light photons have to travel longer distances to reach the photodetector (like a photomultiplier tube). This can lead to more light absorption and scattering, potentially reducing the amount of light collected.

Another example are the Semiconductor Detectors in wich Increasing the volume (thickness) can increase the efficiency for detecting high-energy particles that might otherwise pass through a thinner detector without interacting. However, increasing the volume can also increase the electronic noise and reduce the energy resolution of the detector.

A combination of multiple detectors of different thicknesses can be used to archive a complete detection of charged particles without sacrificing energy or time resolu-

[3]This value correspond to a correction that considered the speed of incident particle with the speed of electrons in the atomic shell its values can be found in [62] for different materials

tion or adding the benefit of distinguishing the type of particle by the energy loss in each detector. The materials, size, number and geometry of detector are a key concept when designing an experiment.

2.9 Branching ratio

The branching ratio is defined as the probability of decaying by one process in respect to another. If an energy state is above the α-particle threshold, the probability of de-exciting by gamma emission drops drastically as it is more efficient to lose the excess energy by emitting an α-particle. It noticeable that gamma transitions are not forbidden meaning that they can still occur but with a relative low probability or a relatively small branching ratio compared with α emission, usually below 1 in a 100000 for excitation energies above the alpha particle threshold [57].

Chapter 3

Experimental Methods

"The ship wherein Theseus and the youth of Athens returned had thirty oars, and was preserved by the Athenians down even to the time of Demetrius Phalereus, for they took away the old planks as they decayed, putting in new and stronger timber in their place, insomuch that this ship became a standing example among the philosophers, for the logical question of things that grow; one side holding that the ship remained the same, and the other contending that it was not the same."
-Theseus By Plutarch, 75 A.C.E.

Translated by John Dryde

The experimental methods described in this section correspond to the latest iteration of the experiment which led to the measurement of the gamma branching ratio and the reduced transition probability B(E2) from the reaction of interest. Previous iterations of this experiment ,as well as data from them, are presented to explain the upgrades of the detection array.

3.1 Reaction of interest

The reaction of interest of this work is formation the compound ^{16}O nucleus caused by the fusion of an incident alpha particle and a ^{12}C target to produce excited into the 16.275 MeV, $J^{\pi} = 6^{+}$ level [57].

From this energy level, the most likely decay channel is alpha-decay, but gamma-decay is also possible, following the decay rules described in section 2.3.

Moreover, there is a possible electromagnetic transition to the 10.356 MeV $J^{\pi} = 4^{+}$ energy level. From this state, the ^{16}O nucleus would have enough excess energy to decay into an alpha particle and a ^{12}C nucleus in the ground state. A depiction of the reaction can be found in figure 3.1.

The 10.356 MeV $J^{\pi} = 4^{+}$ can also decay by gamma emission to three other states, but the branching ratios are comparably low with respect to alpha emission. The states and the relative intensities of these transitions are presented in table 3.1 from data in reference [57]:

Final Energy State [MeV], J^{π}	Energy [MeV]	Relative Intensity to α-emission
6.9171(6), 2^{+}	3439(3)	2.4×10^{-6}
6.12989(4), 3^{-}	4225(3)	3.84×10^{-8}
0.0, 0^{+}	10352(3)	2.16×10^{-10}

Table 3.1: Possible gamma decays from the 10.356 MeV $J^{\pi} = 4^{+}$ energy level of ^{16}O.

In order to populate the energy excitation state of interest with an alpha beam with energy E_{Beam}, the available energy of the system needs to be calculated using the centre of mass energy equation 3.1,

$$E_{available} = E_{CM} + Q = E_{Beam}\frac{M_{C_{12}}}{M_{C_{12}} + M_{\alpha}} + Q. \tag{3.1}$$

This will allow the beam energy to be calculated and by using LISE++ [63] the required target thickness can be obtained in order to determine the viability of this

reaction.

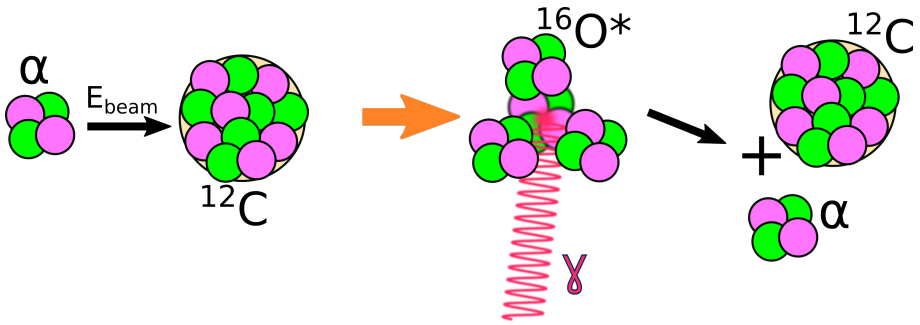

Figure 3.1: Schematic of the reaction of interest and the decay of interest.

3.2 Particle Identification Techniques

It is useful to use Catania plots as a technique to visualise the data from a nuclear experiment, in order to determinate specific energy levels of the remnants from nuclear reactions.

It is possible to generate these graphs by using conservation of energy and momentum. To illustrate how to produce a Catania plot, let's consider the reaction $\alpha + ^{12} C \rightarrow \alpha + ^{12} C^*$, where an alpha particle is inelastically scattered by a ^{12}C nucleus then detected at an angle θ and at energy E_α , leaving the ^{12}C at an excitation level of $Ex_{^{12}C}$. From the conservation of energy we get:

$$E_{beam} = E_{C^{12}} + E_\alpha + Ex_{^{12}C}, \tag{3.2}$$

Re-arranging, we obtain:

$$E_{beam} - E_\alpha = E_{C^{12}} + Ex_{^{12}C}. \tag{3.3}$$

The quantity $E_{C^{12}}$ can be calculated from the conservation of momentum described in appendix A, as the particle is not usually detected. Thus:

$$E_{beam} - E_{\alpha} = \frac{1}{m_C}\frac{\mathbf{p}_C^2}{2} + Ex_{^{12}C}, \tag{3.4}$$

and making $\frac{1}{m_C}\frac{\mathbf{p}_C^2}{2} = E_{reconstructed}$,

$$E_{beam} - E_{\alpha} = E_{reconstructed} + Ex_{^{12}C}. \tag{3.5}$$

To generate a Catania plot, $E_{beam} - E_{\alpha}$ is plotted as the y-coordinate and $E_{reconstructed}$ is plotted as the x-coordinate. The different energy levels are given by the term $Ex_{^{12}C}$ which is the intercept with the y-axis

This technique is thoroughly described and used by S. Pirrie in reference [64].

As a consequence of this, a series of straight line loci will be present on the Catania plot, the slope of which corresponding to the reciprocal of the mass of the reconstructed particle and the y-axis intercepts will correspond to the excitation energy level. This last point means that states in the same nucleus with different excitation energies will form separate loci.

This technique can separate events by type of interaction and by projectile and target nucleus.

3.3 Detection Array

The detection system consists on ten Hamamatsu Photomultiplier tubes coupled with $LaBr_3$ ∅38.1 mm×50.08 mm crystals [65] and two W1-micron [66] Double-sided Silicon Strip Detector telescopes (65 μm + 500 μm).

The front of the $LaBr_3$ crystals are covered by a thin layer of aluminium and they connect to the photomuliplier by a ∅38.1 mm × 5 mm glass optical guide which works as an optical coupling(together with silicon optical grease).

The diametrical area of each detector housing is shielded with a layer of lead to avoid detection of scattered gamma rays from other detectors in the array. This

also increases the probability of the detected gamma rays being fully absorbed by the crystal, as gamma rays (particularly those of high energy as of interest here, *i.e.* with several MeV) can Compton scatter back into the crystal from the lead.

The positions of the $LaBr_3$ detectors are shown in figure 3.2, and the mount can accommodate up to 20 detectors. The solid angle covered by one detector can be easily calculated by using equation 3.6:

$$\Omega = 2\pi \left(1 - \frac{d}{\sqrt{d^2 + a^2}}\right) \tag{3.6}$$

where d is the distance from the centre of the chamber to the face of the detector and a is the area of the crystal. The detectors cover a fraction of the total solid angle 0.111 ± 0.001.

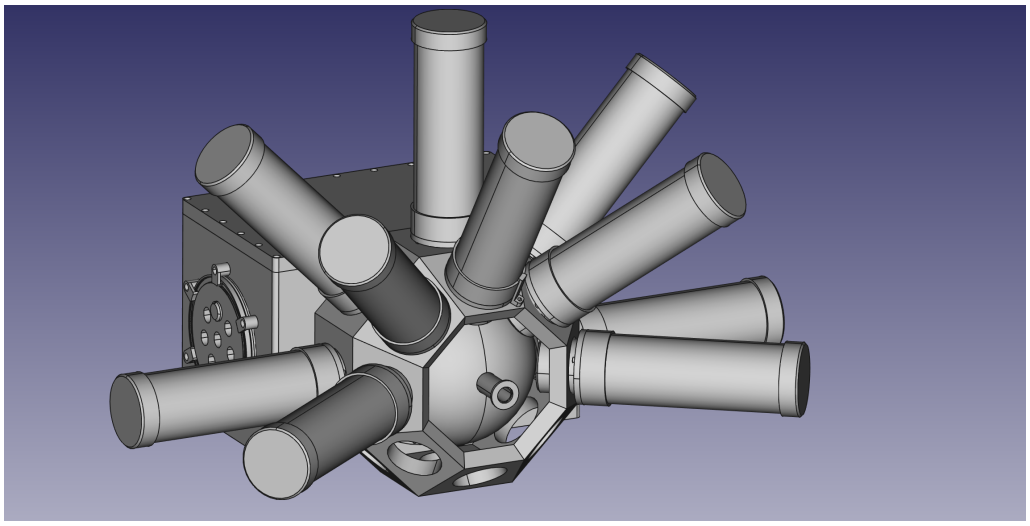

Figure 3.2: Three-D render of the outside of the reaction chamber with ten $LaBr_3$detectors (crystals+photomultiplier tubes in aluminium housing) mounted as in the experiment.

The DSSDs were mounted in a custom support that fits in place inside the chamber, as shown in figure 3.3. To position the target in place, a support was built by the mechanical workshop at the School of Physics and Astronomy of the University of Birmingham. As the beam needs to be conditioned and tuned each day (a more detailed explanation can be found in section 3.9), it is necessary to remove the tar-

get from the path of the beam. In previous iterations of the experiment this meant breaking the vacuum of the chamber, removing the target, vacuum the chamber, conditioning the beam, breaking the vacuum a second time and placing the target and run the experiment. This process required at least one hour in for each vacuum cycle which meant over 15% to 25% of beam time was lost.

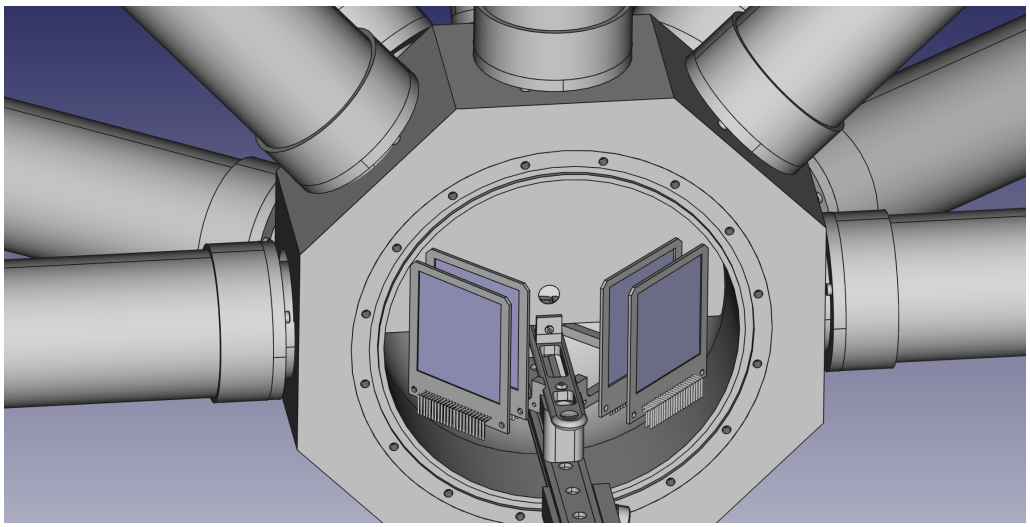

Figure 3.3: Placement of the DSSD telescopes inside the chamber.

To minimise the lost beam time, a new target holder system was created by using a Thorlabs Linear Translation Stage piezoelectric motor [67] which allowed movement and monitoring of the position of a newly designed three target holder from the outside of the vacuum system. A 3D render of this can be seen in figure 3.4. The motor could move only once in vacuum as the piezoelectric components could not dissipate the generated heat, although this was not a problem for the experiment as the position from open to target only needed to be changed once per day of beam time.

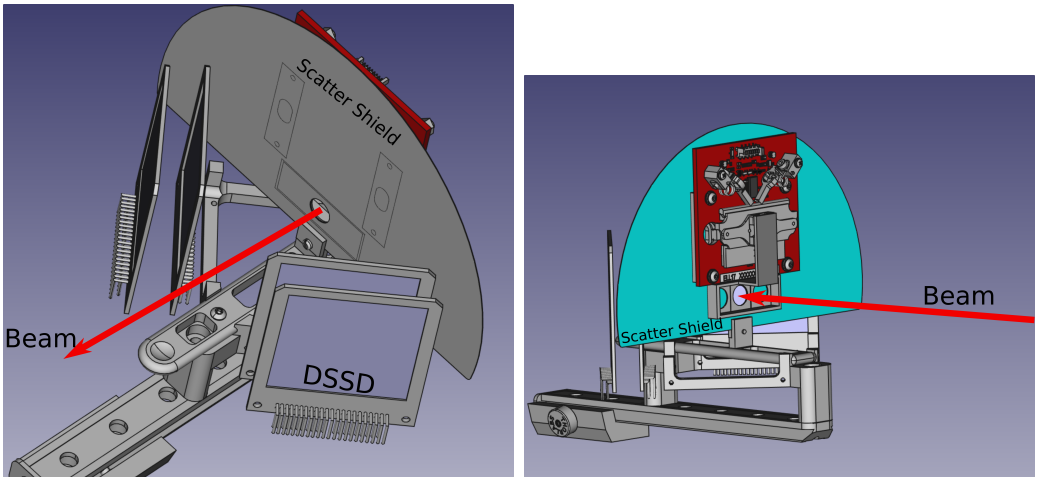

Figure 3.4: Three-D render of the target holder and the scatter shield position.

The DSSD telescopes were placed at 45° and −45° with respect to the laboratory frame of reference, the distance from the target to the face of each telescope was 45 mm.

The face of the detector was perpendicular to the reaction point, but the mount position has an offset of 6.34 mm with respect to the middle of the detector.

The distance from the front telescope detector to the one on the back was 10 mm.

A schematic of the detector placements and collimator system is shown in figure 3.5.

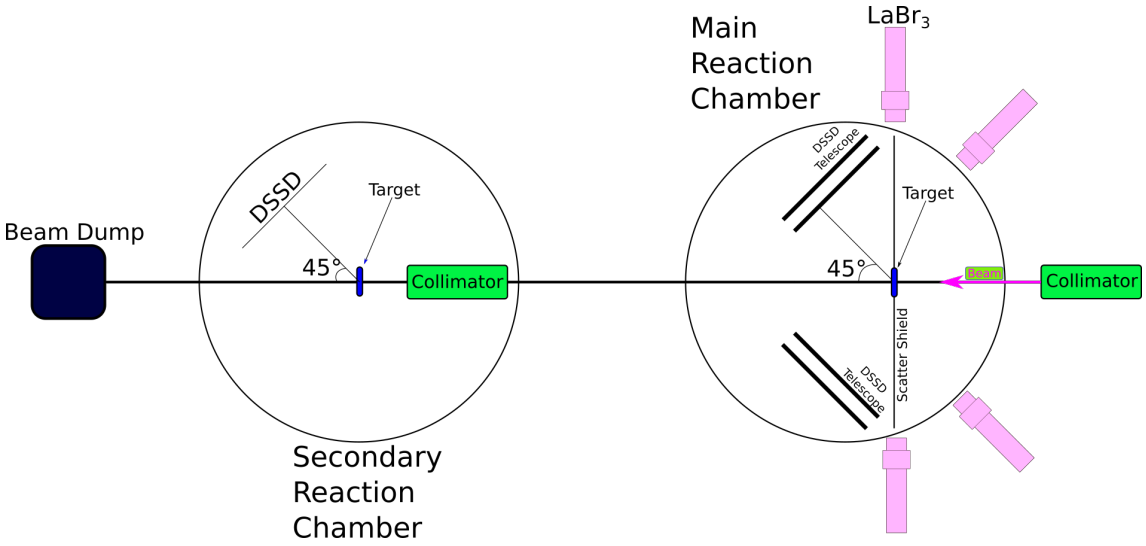

Figure 3.5: Top view of the detection and collimator systems (not to scale). A beam dump is a device to stop the beam completely, in this case it is a Faraday cup to monitor the beam current as well as as well as being used to find the optimal parameters for beam alignment.

3.4 Double-sided Silicon Strip Detector: DSSD

DSSDs are part of the semiconductor detector family. They consist of n-type and p-type doped semiconductors. A reverse bias voltage[1] is applied to these detectors to create a charge depleted region, in which electrical pulses are created through the interaction of ionising radiation. These pulses are created due to the effect of exciting electrons from the valence band to the conduction band, the magnitude of the pulse is proportional to the energy of the incident particle.

[1] Apply positive voltage to the n-type part of the material.

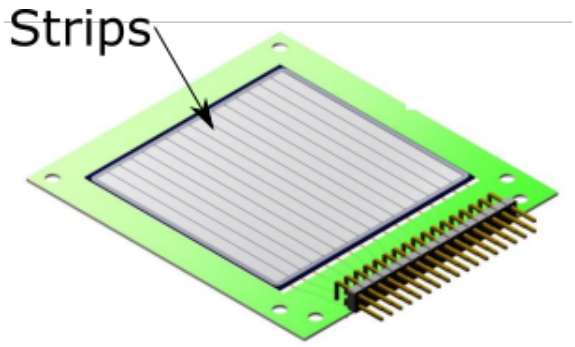

Figure 3.6: The Micron Semiconductors Ltd. W1 type DSSD. Taken from reference [66].

The main advantage of using two DSSDs in a telescope array is to distinguish particles by the energy they deposit in each detector. As mentioned in section 2.8, charged particles can have enough energy to go though a material. This is known as punch-through, and in this case the the particle will still deposit some of its energy. If another thick detector were positioned behind with a greater thickness the particle could be identified as the energy deposition will depend of the Z of the material, the A and Z of the particle and the kinetic energy.

3.4.1 Calibration

The proportional relationship between the pulses created when a particle loses energy in the sensitive volume of the detector is characterised by using α-emitters. The most typical source to use in the calibration of DSSDs for nuclear structure measurements is a combination of ^{239}Pu, ^{241}Am and ^{244}Cm. These sources emit alpha particles at 5.155 MeV, 5.486 MeV and 5.805 MeV respectively. There are more alpha emissions from these isotopes but the intensities are relatively low compared to those mentioned above [68].

These detectors tend to have a linear energy-signal relationship, and in this work the range of energies varies from around 1 to 12.5 MeV, so the calibration of the detectors can be performed reliably using a 3-α source. Figure 3.7 shows an example of a typical 3-α source spectrum.

In the latest iteration of the experiment it was necessary to calibrate 128 channels of charge particle detector signals corresponding to four detectors with 32 strips (16 on the front and 16 orthogonal strips on the back). Calibrating these channels once or twice per day by hand was impractical and with a large probability of human error. An auto-calibrator program was written in order to automate the process.

The program reads in the raw data file as input, finds the peaks, fits a Gaussian curve to each and then fits a linear function of centroid against known energy. The coefficients for each spectrum (strip) fit were written in a data file to be used for later analysis

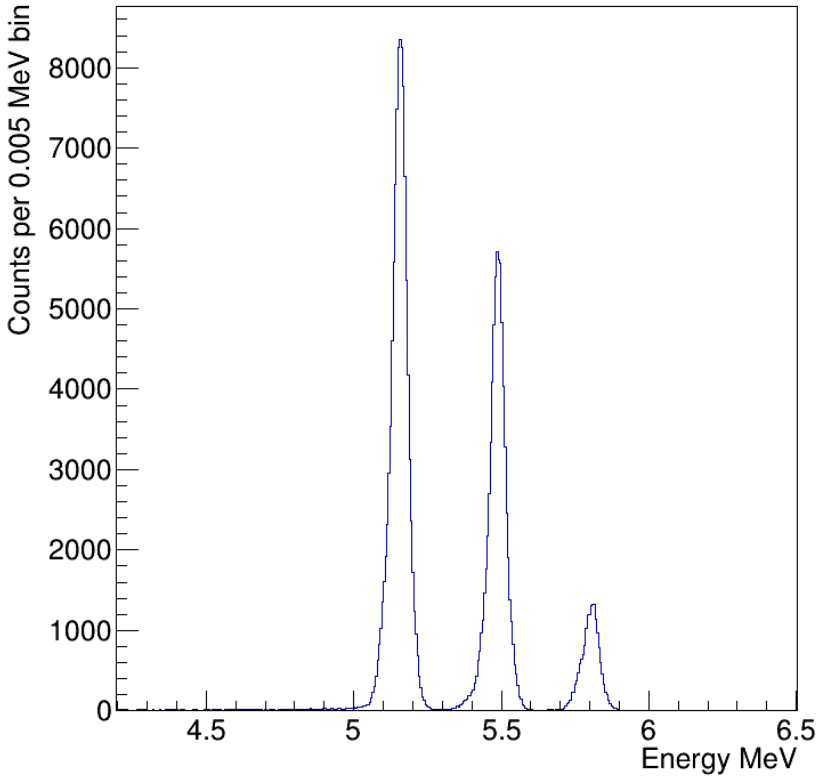

Figure 3.7: Example of a typical 3-α source spectrum, taken during the calibration process for this experiment. This calibration process was done for all 128 channels.

3.5 $LaBr_3$ Detectors

$LaBr_3$ is part of the inorganic scintillator crystal family. In general, inorganic scintillator crystals are formed in high temperature ovens. They possess high stopping power due to high density and high atomic number, as well as high luminosity per unit of absorbed energy (often characterised in photons per MeV) which makes them common in gamma spectroscopy.

These detectors have an exceptionally good light output (165 % better than NaI crystals) in comparison to other crystals which gives rise to their superior resolution [65].

As mentioned in section 2.4 there are three possible ways gamma rays can interact with matter, and these interactions usually create a fast electron. This electron then interacts with the electronic band structure of the crystal structure promoting electrons from the valence band to the conduction band, leaving a trace of secondary particles from interactions.

The electronic band structure is responsible for the scintillator mechanism, as it describes the possible energy range an electron can have (allowed bands) and the bands that cannot be populated (forbidden).

Electrons in the conduction band can move freely within a crystal. In metals, the valence band and the conduction band are superposed, allowing for free movement of electrons. In contrast, in an insulator (such as a scintillator crystal) or in a semiconductor, these bands are separated by a forbidden energy gap, restricting the flow of electrons.

When excited electrons in the conduction band of the scintillator de-excite and return to the valence band, a photon is emitted. This process tends to be inefficient and impurities, known as activators, are added to modify the electronic band structure. The energy of the newly created photon is not enough to excite the crystal making the crystal transparent to its own radiation. This process is shown in figure 3.8.

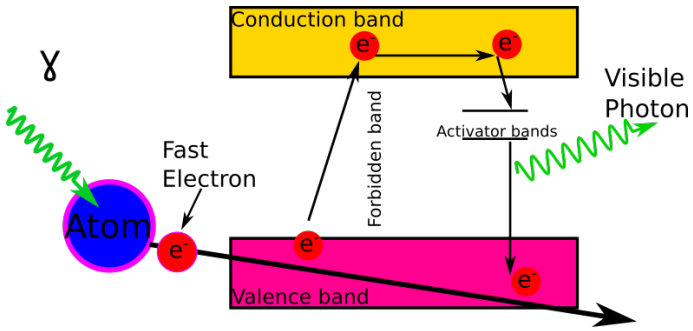

Figure 3.8: Schematic drawing of the gamma absorption and scintillation mechanism for inorganic scintillators.

3.5.1 Photomultiplier tubes

The $LaBr_3$ crystals are coupled to photomultipliers. The principle of photomultiplier tubes resides in the creation of electrons in a photocathode. The electrons produced are then accelerated by several dynodes, each held at an increasingly positive potential. At each dynode stage the number of electrons increases resulting in a cascade effect. The signal, at least for energies below 2 MeV, is proportional to to the energy of the incident radiation.

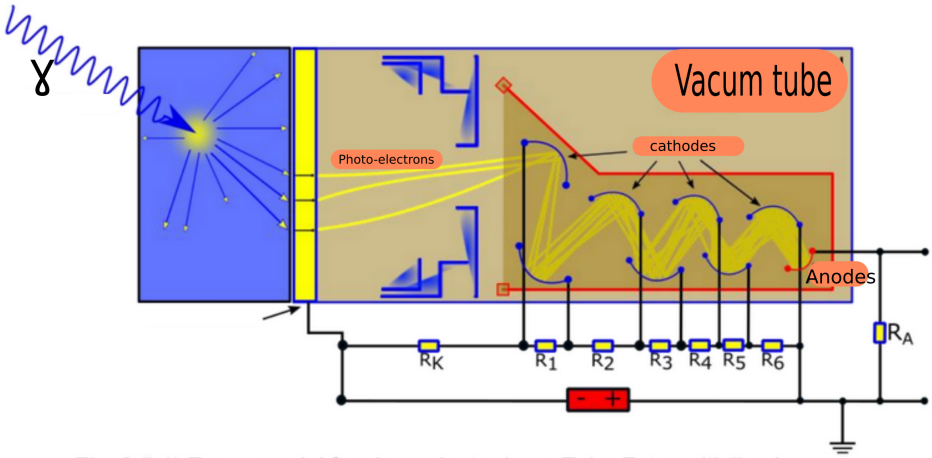

Figure 3.9: Schematic of a photomultiplier tube. Adapted from reference [69].

Gamma detectors are usually calibrated by standard sources (e.g. ^{60}Co, ^{137}Cs, ^{22}Na) but the energy of the gammas from these sources is usually below 2 MeV.

Along with this, at energies above 2 MeV, the response of the detectors (including the photomultiplier tubes) tend to deviate from linearity. Another effect to consider is variation on the gain of the photomultiplier tube as it can change due to thermal perturbations, voltage instabilities, etc.

3.5.2 Calibration

To calibrate the scintillator detectors, gamma rays from nuclear reactions that occurred during the experiment were used. These reactions included inelastic excitation of ^{12}C leading to the first excited state at 4.438 MeV as well as excitation of oxygen contaminants populating the 6.135 MeV level in ^{16}O. In both cases, the energies are high enough to give rise to full-energy peaks as well as single- and double-escape peaks.

The resulting alpha particles from inelastic reactions scatter at a specific angle and energy which allows them to be isolated in specific regions in the Catania plots; the location of the scattered alpha particles enables software coincidence gates to be set to produce clean gamma spectra corresponding to specific nuclei in order to calibrate the $LaBr_3$ detectors.

To improve the selected area, the data from the experiment were compared with the simulations, discussed in the next chapter.

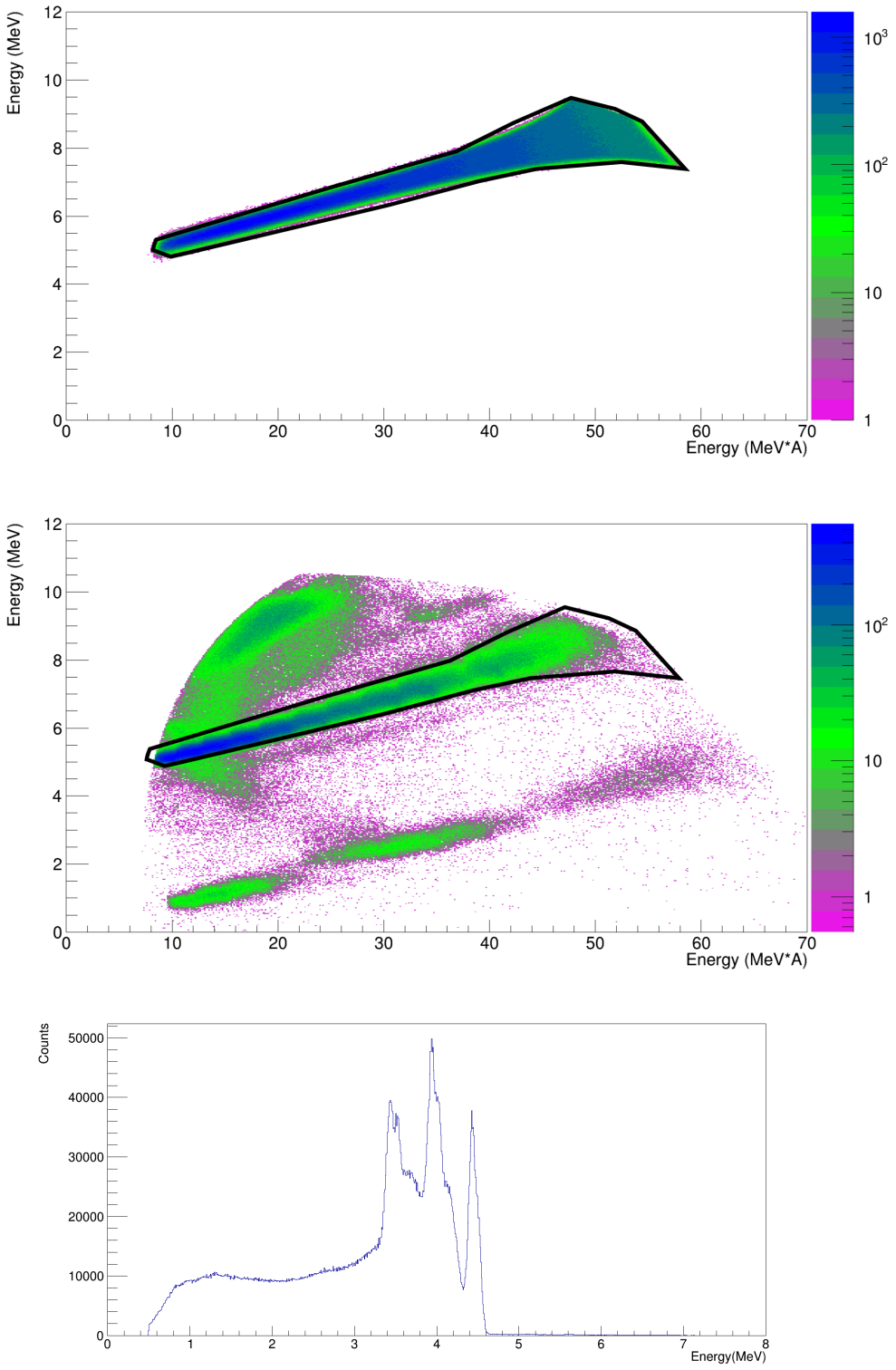

Figure 3.10: Top: simulation of the 4.438 MeV state in ^{12}C to select the area for the graphical gate.
Middle: Using experimental data a Catania plot is generated with the geometric region selected for the 4.438 MeV ^{12}C.
Bottom: Gamma spectrum associated with the decay from the aforementioned state. The full energy peak and both escape peaks were used to calibrate the detector.

A calibration program was written in Python using the Jupyter-lab Notebook computational environment [70] which enabled a graphical interface. The program was used to load the individual gated spectra from each day and each channel, remove the background and run a peak finding routine. The program enabled the parameters obtained (and horizontal spectrum range displayed) to be adjusted. Each detector was individually calibrated with a 2^{nd}-order polynomial corresponding to a channels-to-energy function. These coefficients, as well as the uncertainties were written to text files for further processing. An example of the user interface is shown in figure 3.11.

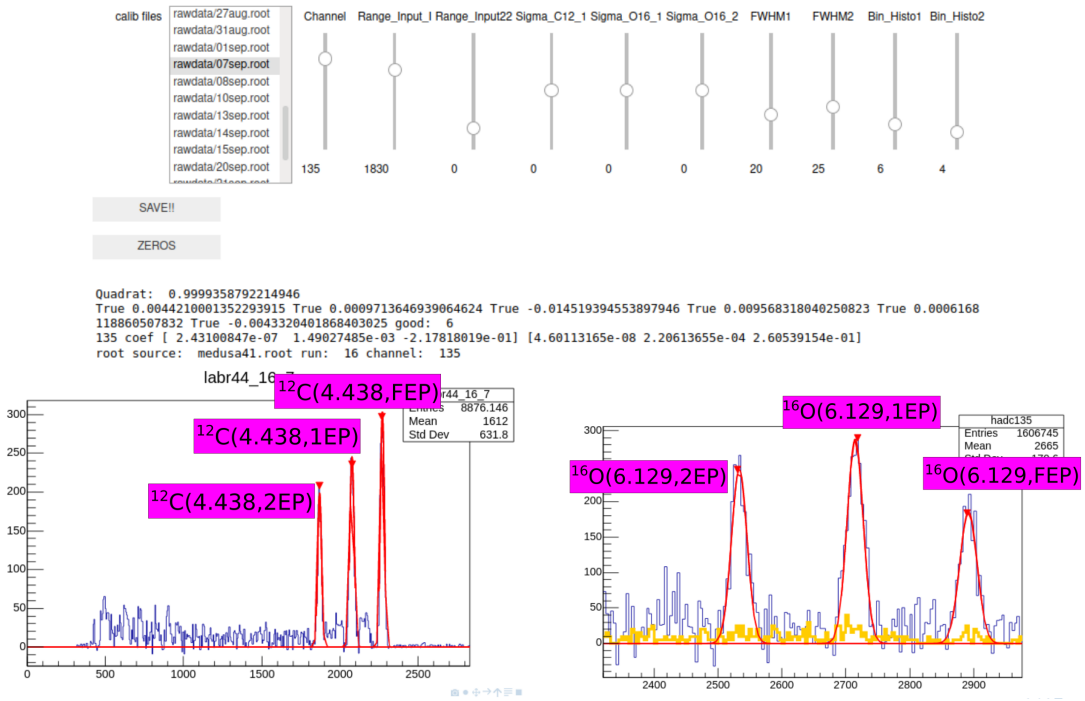

Figure 3.11: Graphical interface of the gamma calibration program, peak identification labels show the peaks used for each detector calibration. **FEP** refers to full energy peak and **1EP, 2EP** are first escape peak and second escape peak respectively.

3.6 Doppler broadening

When a gamma ray is emitted by a moving nucleus, it will present a shift and broadening of energy that will depend on the velocity of the nucleus, the angle of

measurement and the energy of the gamma. These two effects are known as the Doppler shift and Doppler broadening respectively.

To calculate the shift equation 3.7 is used:

$$E_{Dopp} = E_0 \frac{\sqrt{1-\beta}}{1-\beta\cos(\theta)}, \tag{3.7}$$

where θ is the angle of detection, E_0 is the original energy of the gamma ray and $\beta = v/c$.

As the detectors cover a finite solid angle, the detector would be able to detect a continuous shift in the measured gammas, this range of Doppler shifted energies causes the energy spectra to Doppler broaden.

If E_{Dopp} is plotted for a 5.9 MeV gamma with $\beta = 0.01$, a small effect can be observed (shown in figure 3.12). This effect is so small that it would fall within the uncertainty associated with the resolution of the detectors.

The experiment was designed such that the alpha beam particles had just enough kinetic energy to populate the desired state, thus leaving little remaining energy to contribute to the Doppler shift of the compound nucleus ($\beta < 0.01$).

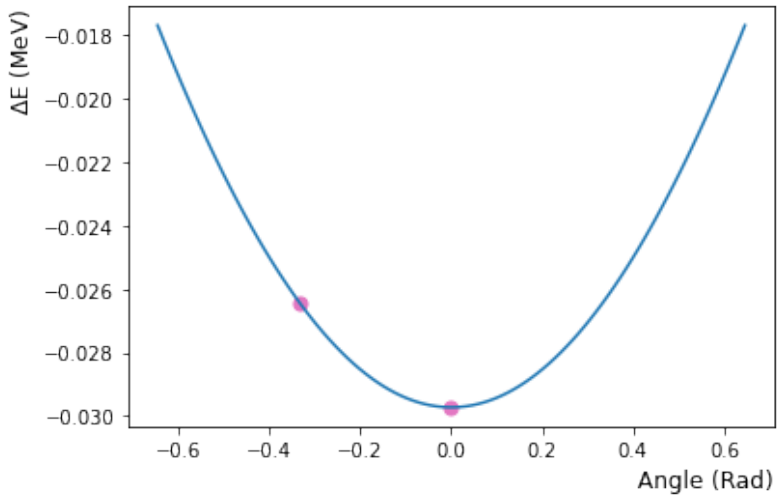

Figure 3.12: Doppler shift for β =0.01, dots represent the relative angles of the $LaBr_3$ detectors from the beam perpendicular axis.

3.7 Data acquisition and Electronics

Data acquisition was handled using the *Multi Instance Data Acquisition System* (MIDAS) [71]. This system enabled the storing of data from the experiment in an event-by-event manner. An event is defined as the group of signals that are digitised in a set amount of time known as the gate, which in this case also triggers the acquisition process. An event can be composed of several hits in one or more detectors; these signals are said to be coincidence when they are detected in a smaller time frame than the time window or gate.

Not all events that trigger the system are of interest,as some of these events may be caused by electronic noise, voltage variations, cable interference, random cosmic background events and nuclear reactions that are not relevant for this experiment; these events can overflow the acquisition system, or generate an excessive amount of triggering, but they can be mitigated by electrically isolating the cables or checking the detectors are correctly plugged in.

Another type of event occurs with signals that are above the discriminator threshold and therefore generate a trigger, but that are below the ADC threshold and thus don't get digitised. Therefore, they don't appear in the data, but do cause dead-time which is the time it takes a signal to be digitised. These events are known as *Bad events*.

Good events on the other hand correspond to signals coming from nuclear reactions of interest and are above the ADC threshold of detection. The ratio between *good events* and *bad events* is usually a good measurement to probe for good performance of the data acquisition system.

A veto signal is also useful to avoid the overflow or buffering of events, stops the system receiving more events during the digitisation of an event, this process can take up to 60 microsceconds, an example of this process is shown in figure 3.13.

This system requires two types of signals in order to convert the energy and time information from the detectors into sorted data in a file. First, the analog signal

from the detectors which contains information about the energy and time of the particles involved in each event; the second type are the logic pulses.

Logic pulses let the system know which events will be saved or vetoed; these signals also control the time when the system is open to receive information from the detectors and can be adjusted. A wide time gate might let information be saved that is not relevant or contain information about two or more events and a narrow gate might not let all the information from an event be saved.

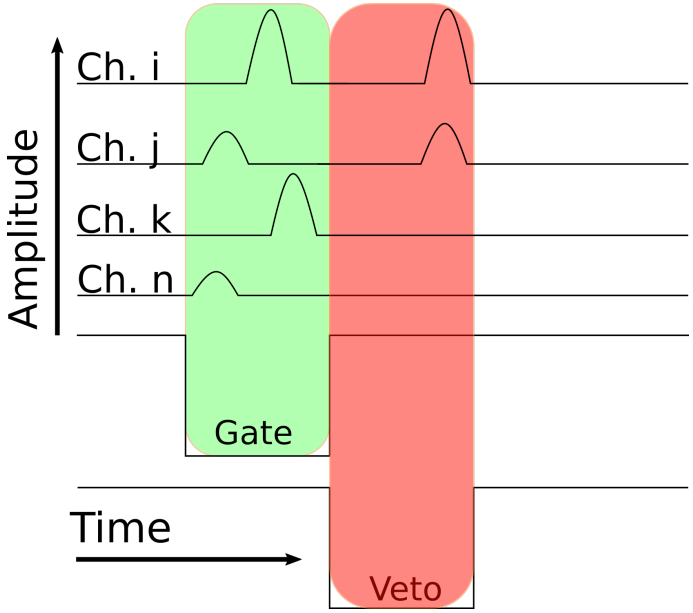

Figure 3.13: In this example, let us imagine an alpha particle being inelastically scattered by a ^{12}C nucleus, exciting it to the 4.438 MeV energy level. After the interaction the ^{12}C nucleus decayed by emitting one gamma ray detected in channel k, the alpha particle hit the left DSSD telescope on vertical strip i and horizontal strip j, a cosmic ray produced a signal in the gamma detector in channel n. The amplitude of these signals will be digitised and saved to file as a single event.
If an alpha particle then elastically scatters off of a ^{12}C nucleus just after the first interaction and happens to hit the same DSSD strips, this only activates channels i and j, but these signals will not be digitised as they arrived during the veto time on the acquisition system.

The detectors produce an analog signal proportional to the energy deposited in it. These signals then are pre-amplified, amplified by Nuclear Instrumentation Modules (NIM) and then converted into a digital set of data; while the logic gate signal is active in the acquisition system.

By knowing the relative positions of the detectors to the reaction point, the angle can be calculated, additionally by using a **Time to Digital** module the relative time between the detected charged particles and gamma rays can be extracted. This information is saved to disk to be further analysed.

The diagram of the electronics chain that makes the data acquisition possible is illustrated in figure 3.14.

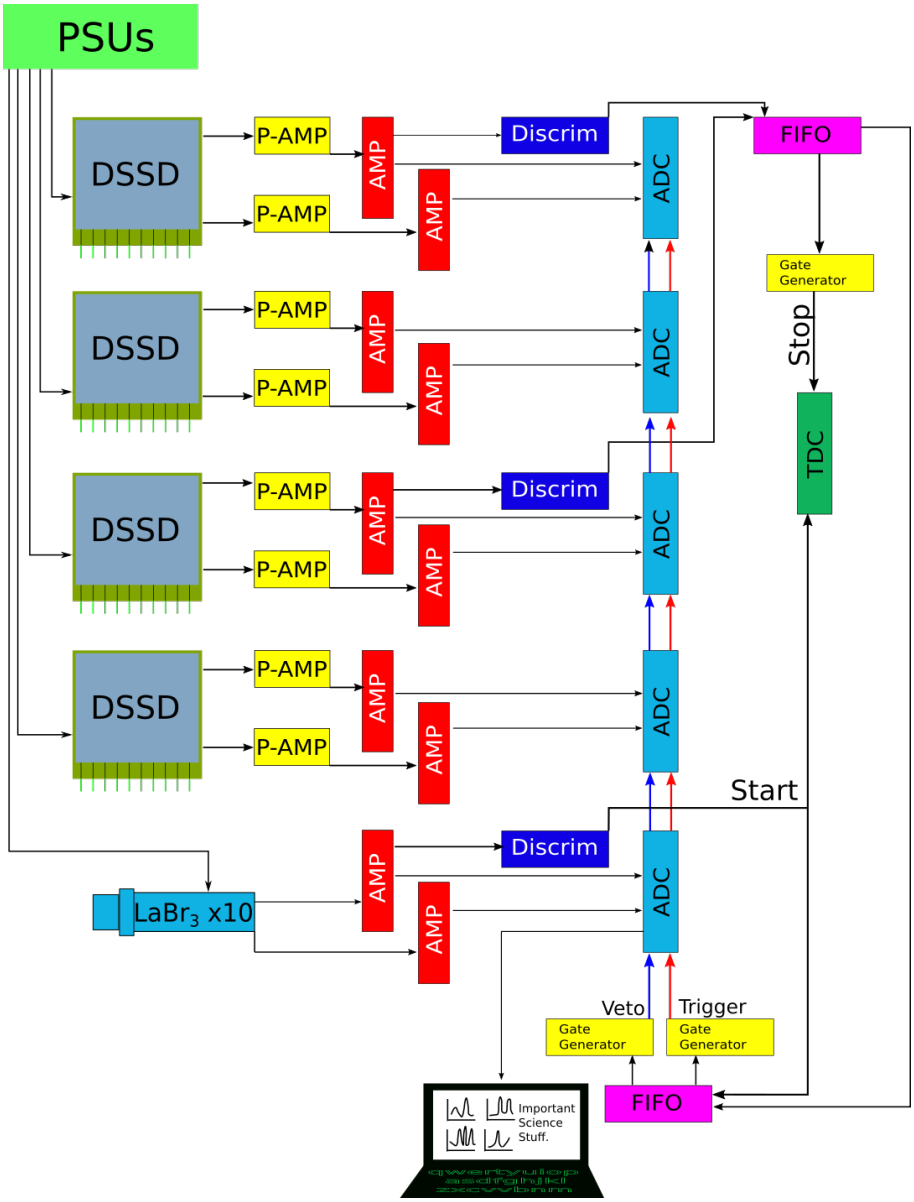

Figure 3.14: Block diagram of the electronics chain used for the signals process for the data acquisition. Below a is a list detailing each module used.

- AMP: Caen N568E 16 Channel Programmable Spectroscopy Amplifier [72].
- P-AMP: Mesytec MPR-16 16 channel preamplifier [73].
- Discrimin: Caen V895 16 Channel Leading Edge Discriminator [74].
- ADC: Caen V785 32 Channel Multievent Peak Sensing ADC [75].
- TDC: Caen V775 32 Channel Multievent TDC [76]
- FIFO: Teledyne Lecroy 428F Quad linear Fan-In/Fan-Out [77].
- Gate Generator 222 NIM Dual Gate and Delay Generator [78].
- PSU: Caen N1470 4 Ch Reversible 8 kV at 3 mA (8 W) NIM HV Power Supply Module [79].

In order to visualise the information from the MIDAS data-acquisition program in real-time, user code was written in the Sunsort data analysis package [71]. These two programs are integrated, Sunsort can read the data from the MIDAS memory location where it is buffered. This allows checking for gain displacements, broken strips, bad events and it is very useful to examine the quality of the data with respect to the physics goal. One of the disadvantages of this system, is the output data file as it is not as compatible with other programs used in this work other than Sunsort. A decoder to convert this file into a ROOT readable file was written so compatibility was not an issue.

The ROOT framework [80][81] offers a lot of flexibility and tools that make the analysis easier, macros can be written in C++ or python [82]. It has a large community along with frequent updates, offers support for multi-core processing, has built-in graphics, as allowing the use of jupyter-notebooks which are a powerful tool for the data fitting and analysis [70].

3.8 The MC40 Cyclotron

A cyclotron is a type of particle accelerator that uses a magnetic field to produce a Lorentz force $\vec{F}$, on charge particles resulting in an acceleration:

$$\vec{F} = q[\vec{E} + (\vec{v} \times \vec{B})], \tag{3.8}$$

where $\vec{F}$ is the resulting force, $\vec{v}$ is the velocity vector of the particle and $\vec{B}$ and $\vec{E}$ are the magnetic and electric fields respectively. It is important to note that the acceleration of the particle in the field is perpendicular to the field $\vec{B}$. A typical cyclotron schematic is shown in figure 3.15.

The MC40 Cyclotron at the University of Birmingham is primarily used as a tool to produce medical isotopes for imaging, and it routinely generates beams of protons, deuterium, helium-3 and helium-4. The range of available energies depends

on the particles that will be accelerated. For helium-4 particles the accelerator can operate between 10 MeV and 40 MeV. The nature of the acceleration produces a pulsed output beam.

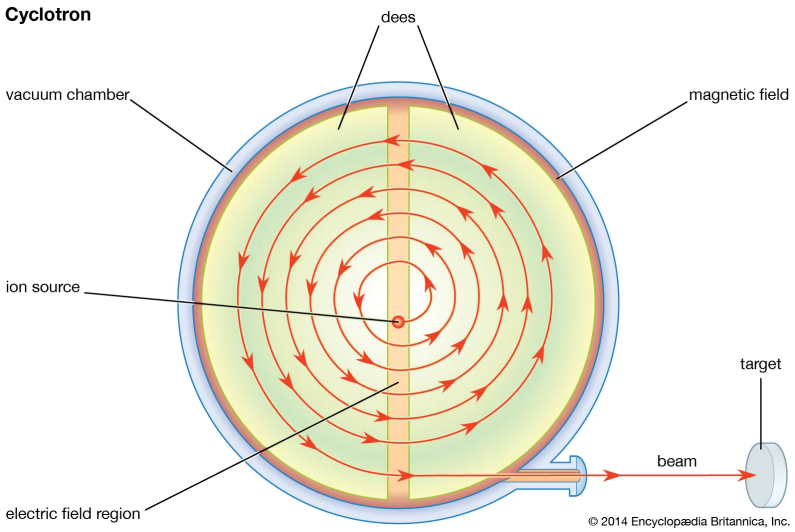

Figure 3.15: Diagram of a typical cyclotron, taken from reference [83].

3.9 Beam transport, current, and energy

Once the particles are out of the accelerating stage it is necessary to transport them to the reaction chamber. The beam tends to diverge, so in order to focus it, several quadrupole magnets are used. This is known as ion optics, as they are analogous to optical lenses. These lenses can focus the beam to decrease scattering from the chamber and beam-pipe components. To change the direction of the beam high-field dipole magnets are used, which work by applying a perpendicular a magnetic field perpendicular to the beam axis. The resulting force is described by equation 3.8 when $\vec{E} = \vec{0}$.

The number of nuclear reactions are proportional to the number of incoming particles, and a high current might saturate the detectors or damage them. The beam current needs to be monitored to avoid these problems. To monitor the current, an ammeter is connected to the target. The target and the scatter shield were in electrical contact and so the measured current corresponded to the sum of both

particles hitting the shield and the target. A current of around 0.065 nA was found to be optimal. This represent around 2×10^8 alpha particles per second.

The energy of the incident particles can be measured by plotting the energy of the detected particles against angle of the detection, E_d vs θ. From the equations in appendix B, kinematic lines corresponding to different masses and excitation energy levels can be drawn over this plot. The beam energy used to calculate the kinematic lines can be adjusted to match the measured energy profiles. In figure 3.16, this process is performed for the main detector chamber (see figure 3.5), a large spread of energy can be observed, caused by the target thickness.

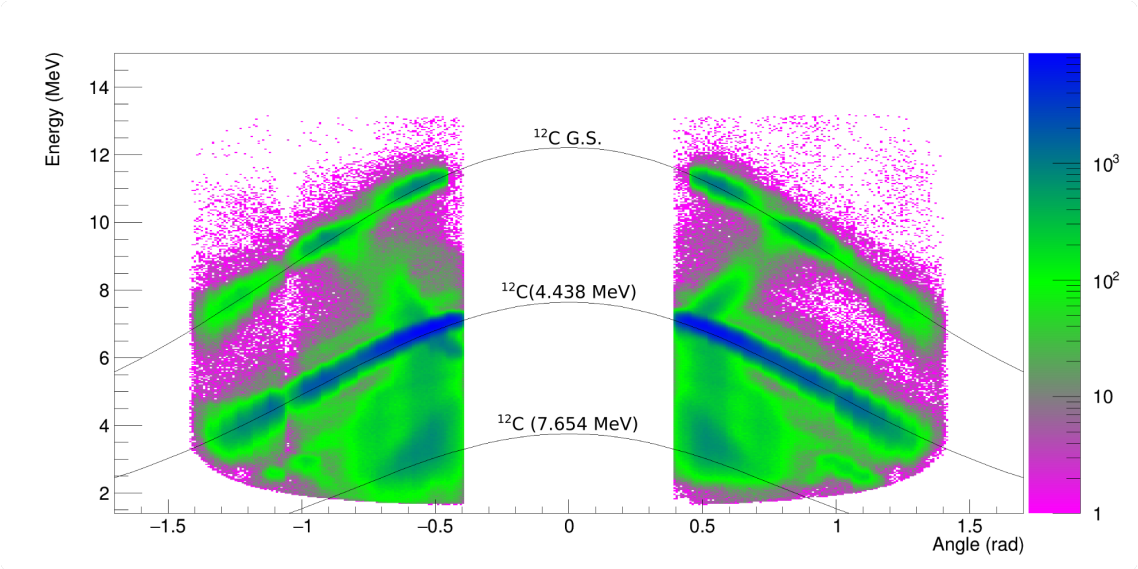

Figure 3.16: Kinematics lines for the reaction leading to different excitation energies superimposed on the data and presented as a E_d vs θ plot.

Cyclotrons tend to have a larger energy spread spread compared to other types of accelerators as the output energy depends on the number of orbits and extraction radius of the particles. To improve the beam energy measurement, an extra detector was added to the system: a Micron Semiconductors Ltd W1 with a nominal thickness of 500 μm, and at a distance of 122.5 mm from the target and at an angle of 45° respect to the beam axis. A thin gold target of thickness 1.2 mg cm^{-2} was used to scatter the beam in the secondary reaction chamber as shown in figure 3.5.

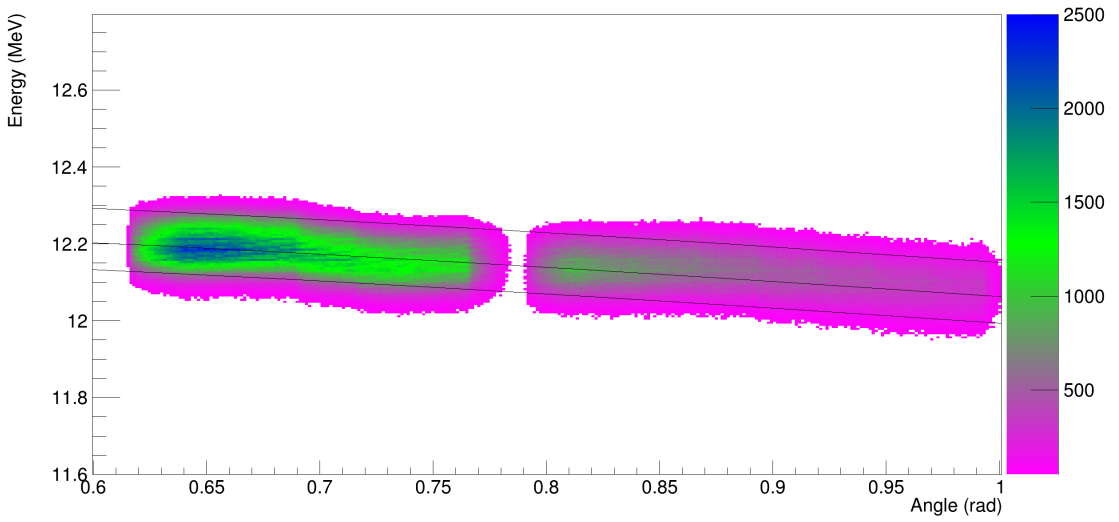

Figure 3.17: Kinematics lines for the reaction $^{197}\mathrm{Au}(\alpha,\alpha)^{197}\mathrm{Au}$ superimposed on the E_d vs θ plot. The middle line is use to calculate the beam energy and the upper and lower lines are references to visually inspect the energy profile in the plot.

To calculate the energy spread caused by the variations of energy in the cyclotron, the projection of energy at a given range of angles is plotted, in this case the range from 0.717 to 0.717+0.05 rad was chosen and this projection is shown in figure 3.18, along with a Gaussian curve fit. The spread of energy is caused mainly by the resolution of the detector and electronics, the energy spread caused by the energy loss and the energy spread caused by the accelerator. The variance of the beam energy considering all of these contributions can be expressed as [84]:

$$\sigma^2_{total} = \sigma^2_{Accel} + \sigma^2_{detector} + \sigma^2_{foil}, \tag{3.9}$$

with $\sigma_{total} = 50.5 \pm 0.25$ keV. The intrinsic energy resolution of this kind of silicon detector is around 25 keV according to reference [85], but the detector resolution worsens during the experiment as charged particles (primarily delta electrons[2]) created by the impact of the beam in the target and the chamber hit the detector, in spite of those effects and the fact that the detector was not exposed to large currents, the energy resolution will be taken as 25 keV.

[2]A delta electron is a fast electron produced by the interaction of charged particles with matter

The spread caused by the foil was calculated by a Monte-Carlo simulation program and found it to be 20 keV at that particular angle range.

From these two quantities and the total energy spread the energy spread of the beam was found to be:

$$\sigma_{Accel} = 39 \pm 4\,\text{keV}, \tag{3.10}$$

which is consistent with the literature in reference [86]. This value it is only to be taken as a starting point close to the actual value, to measure the energy resolution a more precise measurement needs to be performed.

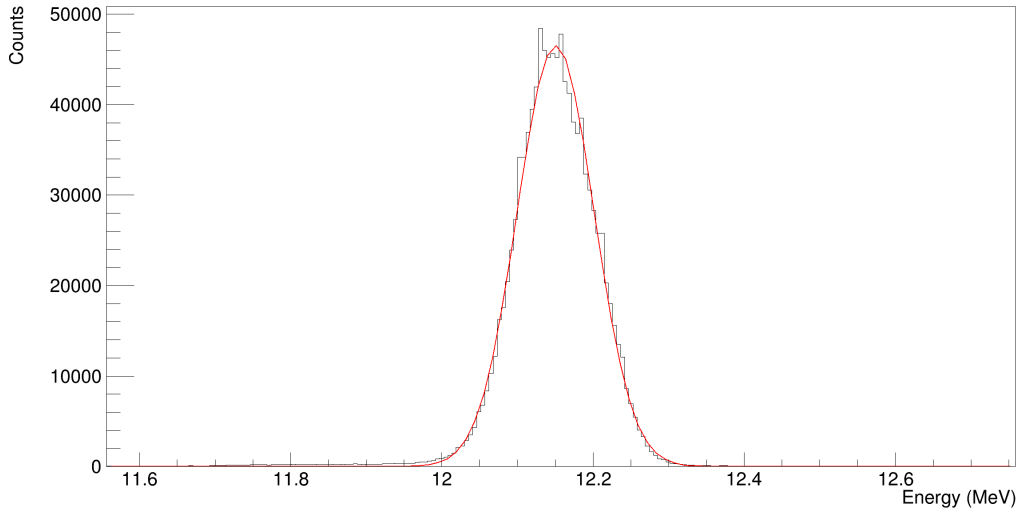

Figure 3.18: Energy projection of figure 3.17 at range 0.717 to 0.717+0.05 rad.

Beam energy was found to be $E_{beam} = \mathbf{12.29 \pm 0.04\ MeV}$. The energy was monitored throughout the experiment and the value remained stable.

3.10 Target

A thin target made of a carbon microleaf [87] with a nominal thickness of 0.5 $\text{mg}\,\text{cm}^{-2}$ was used as a target in this experiment. There are two considerations to select the optimal target thickness:

- The compound nucleus reaction needs to have enough energy available to populate the 16.275 MeV $J^{\pi} = 6^{+}$ excitation energy level in ^{16}O. The energy available for the compound nucleus depends on the beam energy and the Q-value of the reaction. Taking equation 3.1 and making $E_{available} = 16.275$ MeV, allows the calculation for the beam energy in order for the reaction to take place.

- From section 2.8, it is clear that alpha particles will lose energy when they interact with the target material. The incoming beam energy needs be calculated to compensate for this. It is custom to calculate the resonance energy at half the thickness of the target as it simplifies data analysis. These conditions requires the beam energy to be around 12.3 MeV.

The reported uncertainty for the material thickness is ±30%. By using a 3-α source the thickness of the target foil can be measured more precisely by measuring the energy lost by the emitted particles. The 3-α source was placed in a support which held the target in front of it, followed by a DSSD, as shown in figure 3.19.

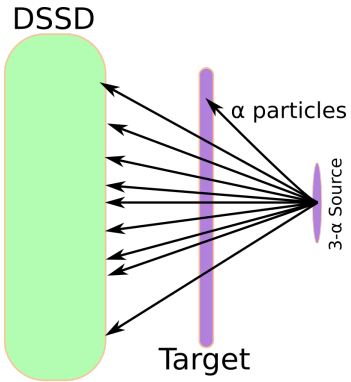

Figure 3.19: It is noticeable that α-particles are emitted radially and the amount of material traversed by the particles will depend on the angle of emission by factor of $1/\cos(\theta)$ where the angle θ is the angle with respect of the alignment axis. By selecting (in the software analysis) only the strip on the DSSD directly in front of the detector and in-line with the alpha source, the thickness of the target was measured.

An initial 3-α spectrum was recorded and calibrated. Once the detector was calibrated, the carbon foil was positioned and a second spectrum was recorded.

These spectra can be seen in figure 3.20. As the alpha particles travel inside the target, some of their energy will be lost. This produces a shift in energy of the original peaks. The results from this measurement are presented in table 3.2.

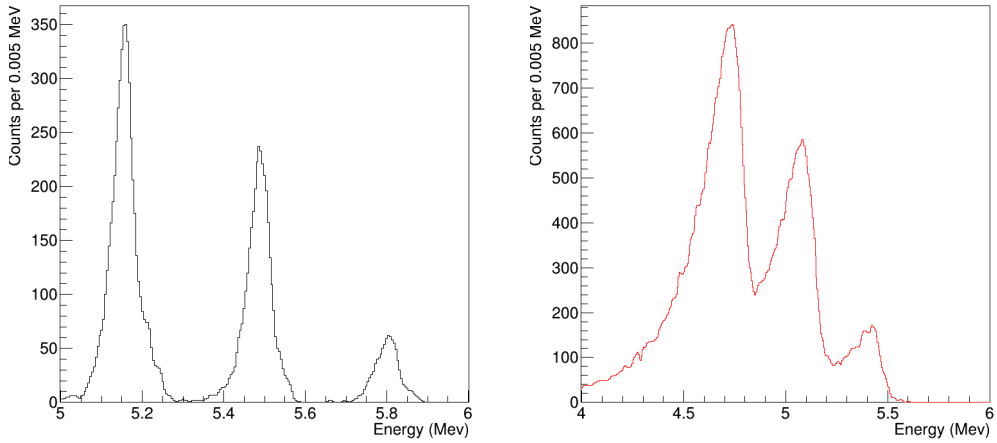

Figure 3.20: Comparison between the energy spectrum from the 3-α source before(left) and after(right) the target was position in front.

Isotope	E_i	E_{Meas}(MeV$\pm$0.002)	Corresponding thickness($mg\ cm^{-2} \pm 0.001$)
^{239}Pu	5.155	4.736	0.520
^{241}Am	5.486	5.077	0.520
^{244}Cm	5.805	5.421	0.518

Table 3.2: Energy-loss measurements and target thickness determination.

The exit energy of the α particle was calculated using the physics calculator in LISE++ [63].

As mentioned in section 3.9, the beam is not completely parallel to the alignment axis and some particles will scatter with material from the chamber and beam-line components. These scattered particles can interfere with the measurement, hence, a scatter shield was place in front of the DSSD telescopes to decrease the incident rate of such events on the detectors. This shield is shown in figure 3.4.

3.10.1 Effective Thickness Calculation

The products of the nuclear reactions are created inside the target causing them to traverse a certain amount of material before being detected. Traveling outside the target will not cause a great effect as the whole chamber is under vacuum. The travel path length the target causes the measured energy to be lower as mentioned in section 2.8. To compensate for this effect and correct the energy it is necessary to calculate the amount of material travel by the particle prior to being detected.

It is impossible to determine where the reaction took place in the target so it is customary to set the point of interaction as the middle of the target. The amount of material traversed is related to the nominal thickness of the material and the angle of detection as shown in 3.21. From the diagram the relationship between measured angle and distance travelled in the target can be found in equation 3.11:

$$t_e = \frac{t}{\cos(\theta)}. \tag{3.11}$$

It is notable that at 90^o there is a discontinuity, which comes from the fact that the function is calculated assuming an infinitely long target, but for the scope of this work this approximation is enough, as there is no detection at 90^o.

The process of the energy-loss correction from the effective thickness is explored in section 4.3.

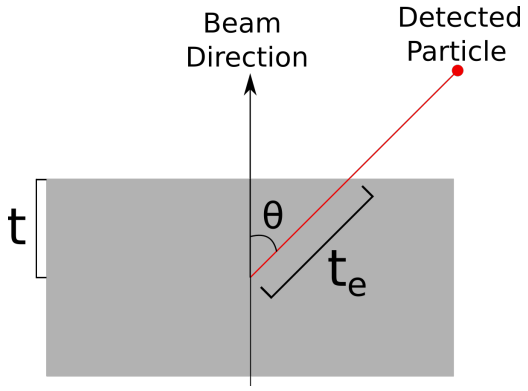

Figure 3.21: Schematic of a particle escaping the target at an angle θ. Here, t is half of the nominal thickness of the target used and t_e is the effective thickness for final state particle traverses following a reaction when detected at an angle θ.

Chapter 4

Simulations

"Do I believe, for example, that by using magic I could fly? No. How would you get around gravity? Impossible. Do I believe that I might be able to project my consciousness into a very, very vivid simulation of flying? Yeah. Yes, I've done that. Yes, that works."

-Alan Moore

To understand the data from the experiment, it is convenient to write Monte-Carlo simulations, to study the efficiency of radiation detection, fitting data and understanding the underlying phenomena in a controlled situation.

This work used the combination of three programs to create the simulations needed to understand the data:

- **GEANT4** [88] toolkit for response of materials when interacting with gamma radiation.
- **ATIMA** [89] for ion energy loss in materials.
- A two body kinematic equation solver to recreate the aftermath of two nuclei interacting written for this project.

To combine these elements, the multi-threaded program called **sudor** was written.

This program combined the output of each element and managed the CPU cores to run the program in a time efficient manner. In the next sections all of these parts are detailed.

4.1 GEANT4 simulations

GEANT4 (G4) is a powerful and versatile toolkit to simulate radiation interactions with matter [90][91][92]. It uses a combination of equations and compilations of real data to accurately simulate the passage of radiation through matter. G4 simulations are used in high [93][94] and low [95][96] energy physics, medical [97], space [98] and astrophysics [98] applications, etc. [99].

The validation of G4 simulation capabilities have been extensively studied in the literature such as the work in references [100][101][102].

As mentioned in section 2.4, gamma rays can interact with matter in one of three different processes, this would be impossible to simulate from scratch in the time-frame of this work.

The 16.275 MeV state of interest has a large energy spread, Γ (=420 keV [57]), and this will produce a broad gamma energy transition when decaying and can not be approximated as a mono-energetic source. This effect will produce a gamma spectrum which is not as simple as the ones mentioned in 2.6 and for this reason a G4 simulation is indispensable in order to extract the information from this experiment.

The validation of G4 simulations made for $LaBr_3$ detectors has been extensively studied in references [102][103][104].

In work presented in these references, a comparison between experiments and the simulations are performed, validating the capabilities regarding material response and detection efficiency. Because of this, the work presented here does not focus on validating G4 simulations, but rather G4 is taken as a suitable and accurate tool to simulate the events generated in this experiment

To start a G4 simulation the declaration of the geometry of the detector is first, then its material composition and that of its surroundings and its position in a virtual space called *world*. To define an actual detection volume, the declared detection material needs to be set as a *sensitive volume*.

A definition of the physics models needs to be included; the choice of physical effects depends on the type of radiation and the materials with which it interacts as well as the energy ranges of the particles. A complete list of the library models can be found in reference [105]. In this work the libraries included are: **G4EmStandardPhysics** and **G4EmPenelopePhysics**. These two libraries handle the process of interactions between gamma and matter discussed in section 2.4.

The parameters for particle emission need to be declared too, these include emission distribution, energy and type of particles. Note that these simulations only included gamma rays up to 8 MeV.

After these steps, it is necessary to define the number of emitted particles. The data are saved in ROOT in the form of spectra to be used later in other programs. A detailed G4 starter guide can be seen in [88].

In the simulations written in this work, the $LaBr_3$ detectors were recreated in G4 considering the thin aluminium covering, optical guide connecting to the photomultiplier tube, the lead shielding around them and the hemi-spherical aluminium structure of the reaction chamber. A render inside G4 of the chamber is shown in figure 4.1.

G4 simulations allow users to study the effect of the detector and its surrounding materials to better fit experimental data. An example of this is shown in 4.3 where the expected features of gamma interactions with a detector are noticeable *i.e.* full absorption peak (photo-peak), escape peaks, Compton edge and Compton continuum. With the inclusion of more materials in the detection array, effects such as the back-scatter peak ($\approx$ 200 keV) appear.

One of the most noticeable features is the peak at 511 keV, which is due to the

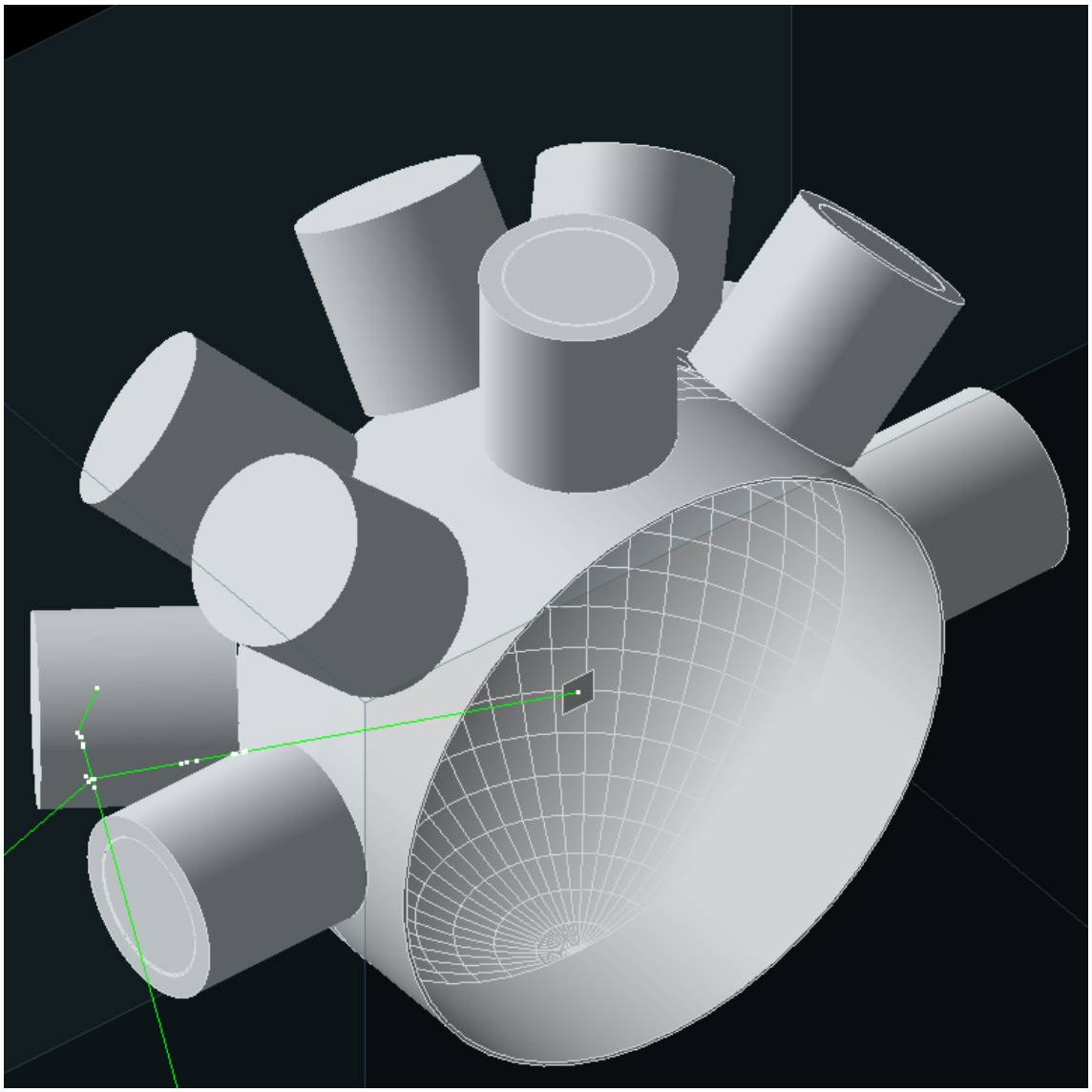

Figure 4.1: GEANT4 render of the simulated chamber. An emitted gamma ray can be seen interacting with a $LaBr_3$ crystal, this interaction shows the importance of G4 simulations for this experiment as the gamma ray can interact through different processes inside the crystal.

high energy gamma rays interacting with the lead detector shield, producing $e^+ - e^-$ pairs. However, because of the cylindrical symmetry of the lead shielding system, only one of the 511 keV gammas is detected. This effect is shown in figure 4.2. The process of pair production can only occur when the energy of the original gamma ray is above the energy threshold of 2x511 keV.

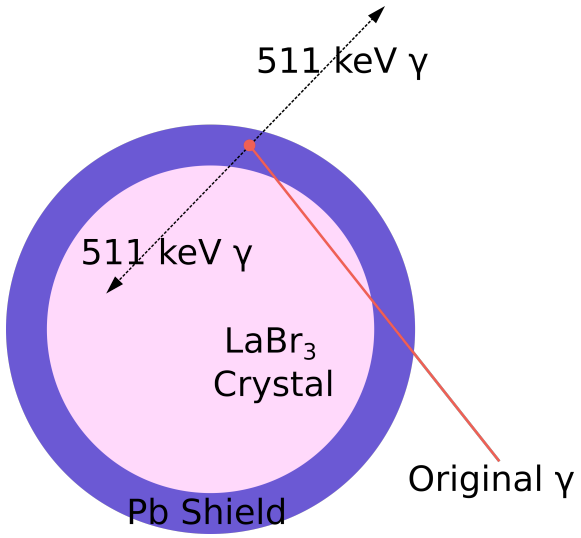

Figure 4.2: Gamma ray interacting with the lead shield of a detector producing a $e^+ - e^-$ pair followed by a back-to-back 511 keV γ-pair from the position annihilation. Due to the geometry of the lead shield, there is a high probability of only one of these gammas being detected and contributing a 511 keV peak to the spectrum.

It is noticeable that the detector is more efficient at low energies making it easier for these secondary gammas to be more prominent. This interaction is faster than the time window of detection defining the length of an event and these gammas will be detected.

Events where **only one** alpha particle plus **only one** gamma ray are emitted in coincidence, are the main focus of this experimental work. To properly recreate this in the simulations, only one of the $LaBr_3$ crystals is set as a **sensitive volume**, then the number of events detected is corrected by a factor of a ten, as there are ten detectors in the experiment.

Taking all crystals in the simulations as **sensitive volumes** would result in events that could have had several interactions with the materials and energy being

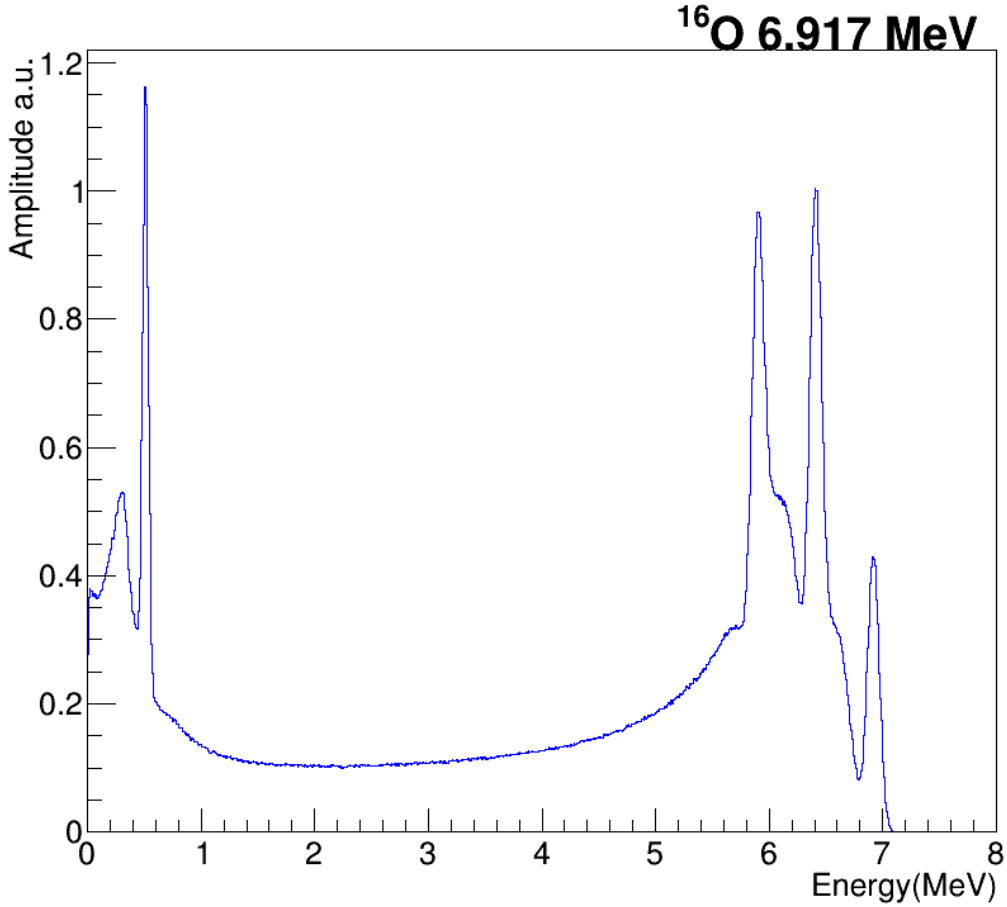

Figure 4.3: Simulated spectrum of the 6.9171 MeV $J^{\pi} = 2^{+}$ state decay to the ground state in ^{16}O with realistic material response from the detection array. As the original energy of the gamma is much greater than $m_e c^2$, features such as single and double escape peak and multiple Compton events can be seen, as well as, the peak at 0.511 MeV which comes from gamma rays interacting with the lead shield. There is also a prominent backscatter peak around 200-400 keV.

deposited in several detectors. This would introduce more contributions to the Compton continuum and a peak at 1022 keV corresponding to the sum of two 511 keV gamma rays that reached one or two crystals. These events would not correspond to a real recorded datum from the experiment.

4.1.1 Electronic Modules Response

In general the output spectra from G4 will not include the photomultiplier tube nor the response of the electronics modules, this is added later in the simulations to match the data from the experiment. To add this response to the simulations, the total resolution of the array after combining the energy calibrated spectra from all run-days, was used. A plot of the total resolution of the array can be seen in figure 4.4. The energy peaks that were chosen for this measurement are:

- 3.415 MeV from double escape peak of 4.438 gamma from ^{12}C*
- 3.927 MeV from single escape peak of 4.438 gamma from ^{12}C*
- 4.438 MeV from full energy peak of 4.438 gamma from ^{12}C*
- 5.107 MeV from double escape peak of 6.129 gamma from ^{16}O*
- 5.618 MeV from single escape peak of 6.129 gamma from ^{16}O*
- 6.129 MeV from full energy peak of 6.129 gamma from ^{16}O*

to remove the contribution from them being on top of the Compton continuum the background removal option was used in ROOT. This tool uses the methods described in references [106][107][108].

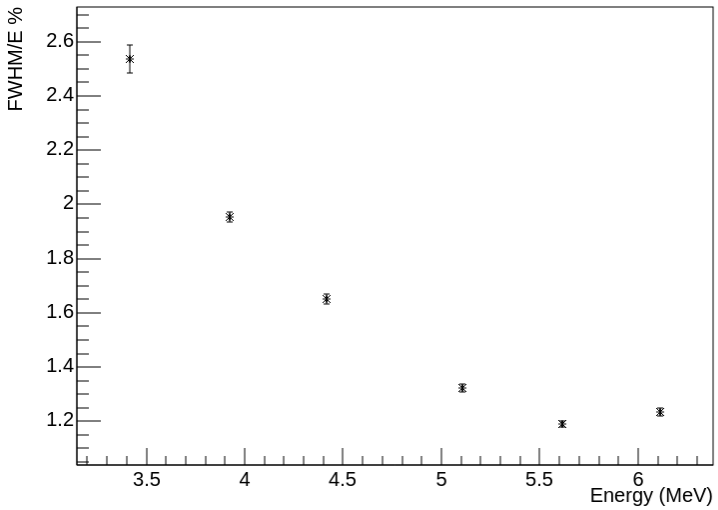

Figure 4.4: Resolution at full peak energy. The last datum falls from the trend the resolution follows, but this is mainly due to low statistics of that particular state, the detector becomes less efficient at higher energies and the oxygen mass in the carbon target is a contaminant, so its actual contribution to the composition of the target is unknown.

The last datum of the resolution is not considered for the energy resolution function as it falls from the expected trend and it represents an statistical anomaly. As mentioned in section 3.5 the gain might shift during an experiment performed over several weeks, furthermore, the experiment was conducted over the span of 2 months. However, the resolution of the detector should not change as it is intrinsic to it.

To verify this, the resolution was measured every day. In figure 4.5 there is no unreasonable change in the resolution in most days with the exception of run day 21. This is likely caused by the low statistics of that particular day and the fact that a background estimator was used to isolate the peak, however this was not the usual trend and the resolution remained stable during all measurements, making the total resolution measurement reliable for most of the chosen peaks.

While the resolution measurement represents a worse resolution compared to the usual literature value [102] for $LaBr_3$ crystals, it is notable that this experiment was not focused on measuring the resolution nor was the measurement ideal for that

type of investigation.

Note that the 6.129 MeV peak from ^{16}O originates from an oxygen contaminant in the target, which means that the detection of these gamma rays depend on an uncontrolled variable. This effect makes the measurement of the resolution non-optimal in that region of energies as the event count is relatively low in each detector.

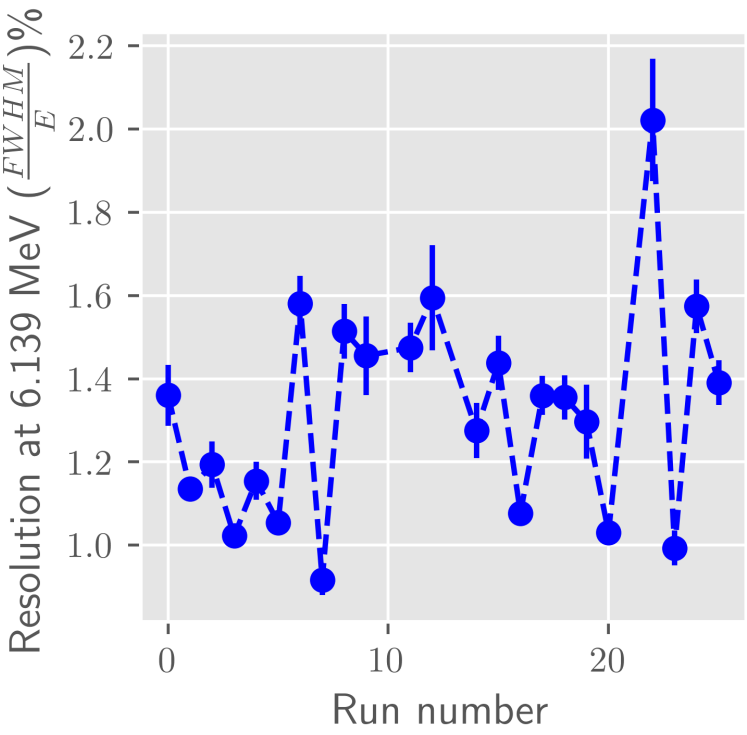

Figure 4.5: Tracked resolution at full peak energy in all runs of the experiment.

4.2 Efficiency of the array

The idea of G4 simulations to calculate the efficiency of a detector has been extensively studied, notably in hyper-pure germanium detectors [109] and in $LaBr_3$ [102]. It is useful to have a tool to study the efficiency of a material without performing an actual experiment which can be difficult as widely used reference sources such as ^{22}Na, ^{60}Co, ^{137}Cs, etc. do not emit at higher energies ($\gtrsim$ 1.4 MeV).

To generate higher energy gammas, in general, nuclear reactions need to be used. Note there are some sources that emit gammas in the 2-3 MeV region but these

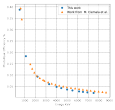

Figure 4.6: Comparison between simulations performed in this works and the measurements reported in reference [102]. The trend and values are in close agreement.

tend to be short lived isotopes. A very detailed explanation of high-energy gamma measurements using reactions is given in reference [102]. The disadvantages of such an approach are that experiments can be costly both in time and money.

One method to validate the simulations of this work is to compare them with the ones in Citmala's *et al.* [102] work. The $LaBr_3$ crystals used in the present work are slightly smaller and, therefore, in this experiment a small reduction in the efficiency is expected compared to that reported in reference [102] where the cylindrical $LaBr_3$ crystals used had dimensions: ∅50.08 mm×50.08 mm. The energies of the simulated gamma rays were: 511, 1100, 2200, 3300, 4000, 4438, 5000, 5500, 6129.89, 6500, 6917.1 and 7500 keV. In figure 4.6 a comparison between Citmala's *et al.* and the simulations in this work is shown.

4.3 ATIMA

ATIMA (ATomic Interaction with MAtter) is a widely used program to calculate the energy loss of charged particles through matter. It was developed at GSI [89] and while the program itself does not have a formal citation in a peer-reviewed journal, the methods and calculations have been extensively validated as reported in reference [110]. While GEANT4 is capable of calculating energy-loss of charged particles in media, it was more practical and direct to use ATIMA. The program was modified for this work (in order to automate the production of energy loss tables). The output file is a table (for each particle and material) with energies in MeV and ranges in mg cm^{-2} for the specific ion in the material. These tables are then used by the program **sudor** to calculate the energy loss using the method described in the section "Interaction of Heavy Charge Particles" in reference [61]. A schematic of how the energy loss that needs to be subtracted is obtained is shown in figure 4.7.

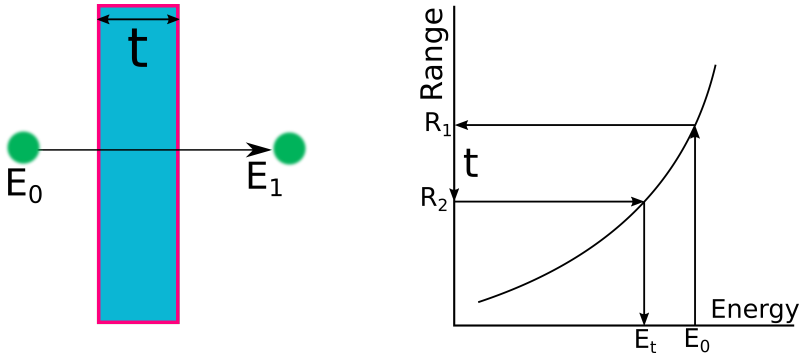

Figure 4.7: If a particle with energy E_0 passes through a material of thickness t, the energy loss is calculated by subtracting the thickness t from the original range R_1 resulting in range R_2, from the table it is possible to calculate the energy at that specific range. The routine written for this part of the analysis calculated the inverse function and then made an interpolation to improve the results.

In figure 4.8, the range data at different energies for alpha particles moving in carbon can be seen. These data were obtain from ATIMA V1.41 and used in the energy loss calculations for the detected events.

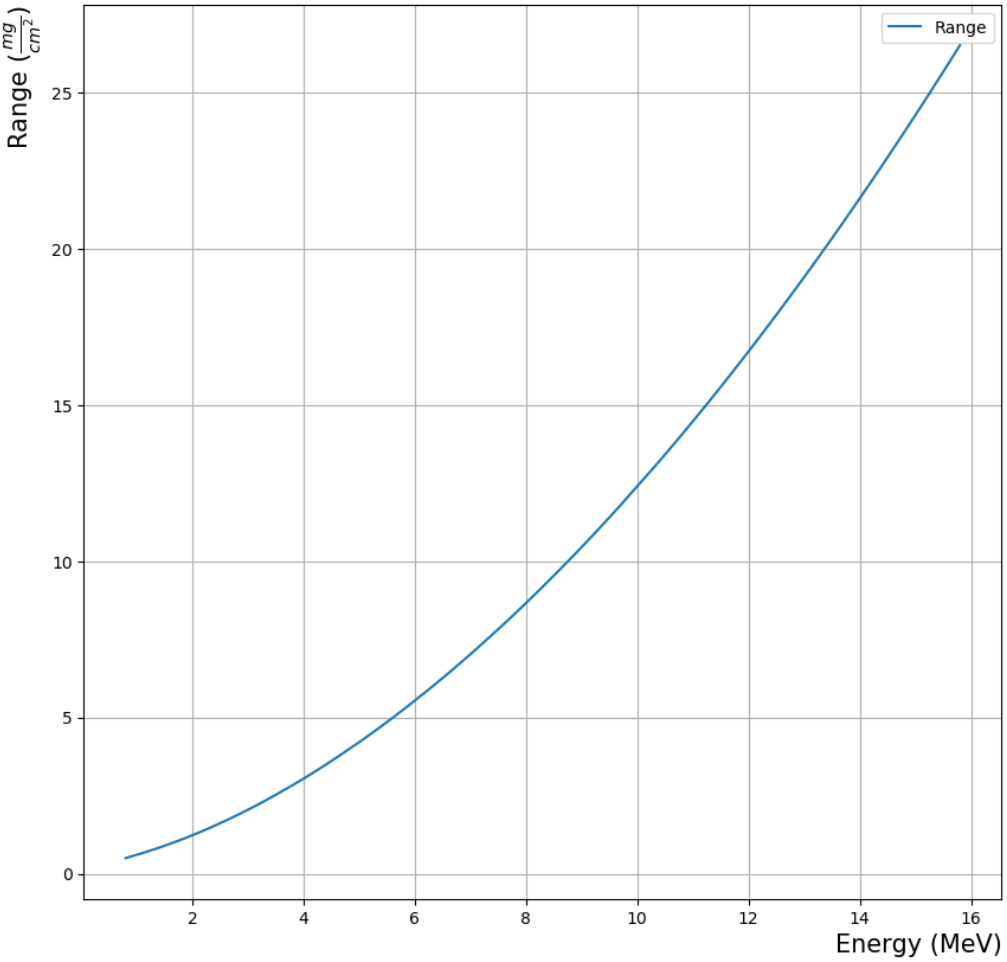

Figure 4.8: Calculated ranges for alpha particles moving in carbon.

4.4 Alpha+gamma correlation simulations

While G4 is exceptionally capable of creating the precise material responses when interacting with radiation, it is limited in the creation of simulations where two or more particles are in correlation. Consequently, another Monte-Carlo simulation program was written.

This program takes the material response spectra from G4 and, by solving the kinematics of particle interactions discussed in appendix B, creates simulated events that can then be used to compare with the experimental data to aid the extraction of information from the experiment. The simulations included the effects of: beam energy smearing due to energy loss and beam energy variations, a random interaction

deep inside the target as well as beam divergence and detector resolution.

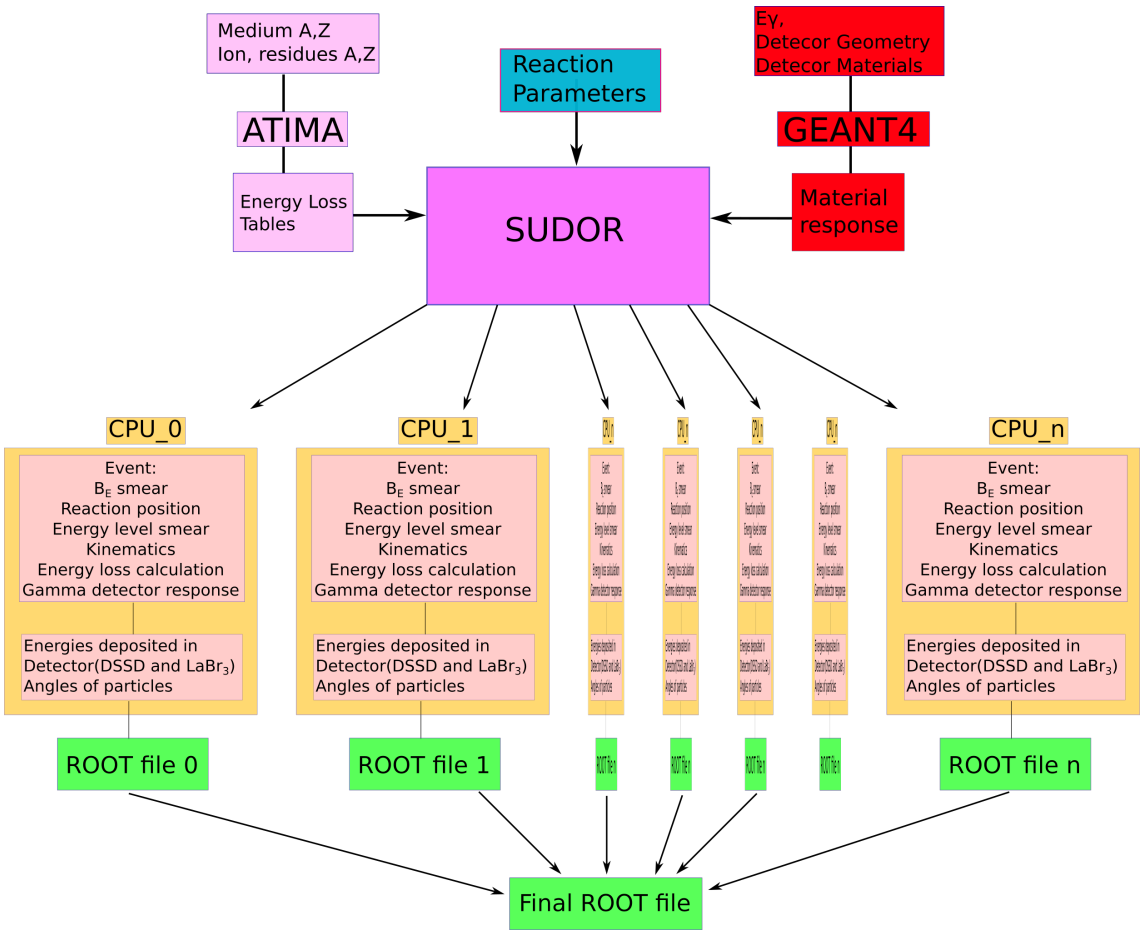

Figure 4.9: Components flow chart of the simulation process.

This program was written to specifically isolate the regions where the charged particles are in a Catania plot or an E vs θ graph. These geometric regions are then used to set conditions called *gates* on the real data in order to isolate gamma events.

G4 only generates material response spectra, these spectra are used as Response Probability Functions **RPF** and every simulated reaction takes one as an input parameter in order to generate the gamma events.

This method not only produces correlated $\alpha - \gamma$ events but also adds a realistic material response, both in the charged particle detectors and the gamma detectors.

In figures 4.10 and 4.11 the simulated 4.438 MeV 2^+ state in ^{12}C presented on a Catania plot is compared with the data from the experiment. A similar comparison is done for the inelastic scattering reaction $^{16}\mathrm{O}(\alpha,\alpha)^{16}\mathrm{O}^*$ populating the 6.129 MeV

and 6.921 MeV states of ^{16}O. These data show a good agreement between simulated charged particles and detected particles with respect to their position and energy.

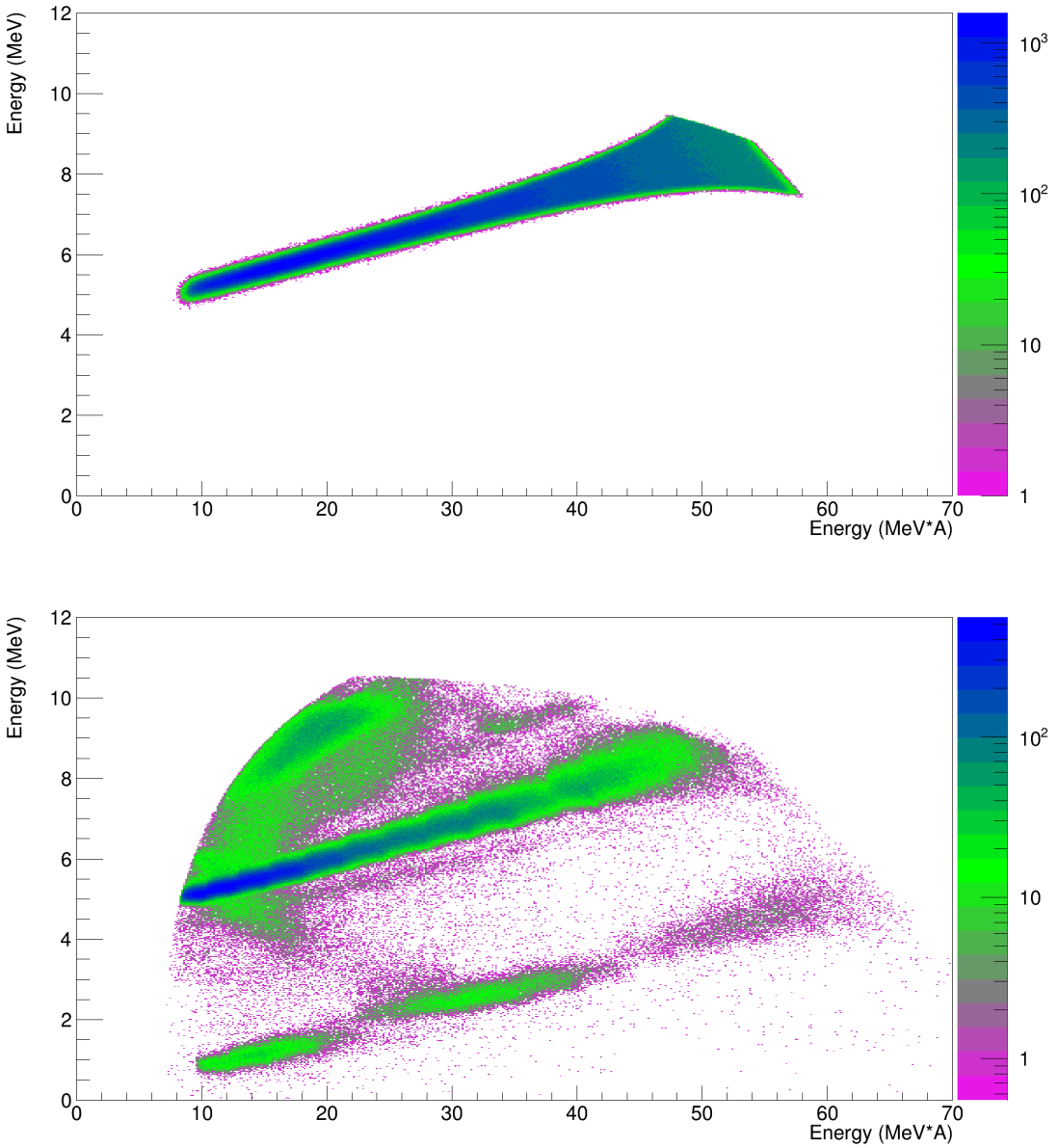

Figure 4.10: Comparison of simulated data (top) and real data (bottom) corresponding to the 4.438 MeV 2^+ state in ^{12}C.

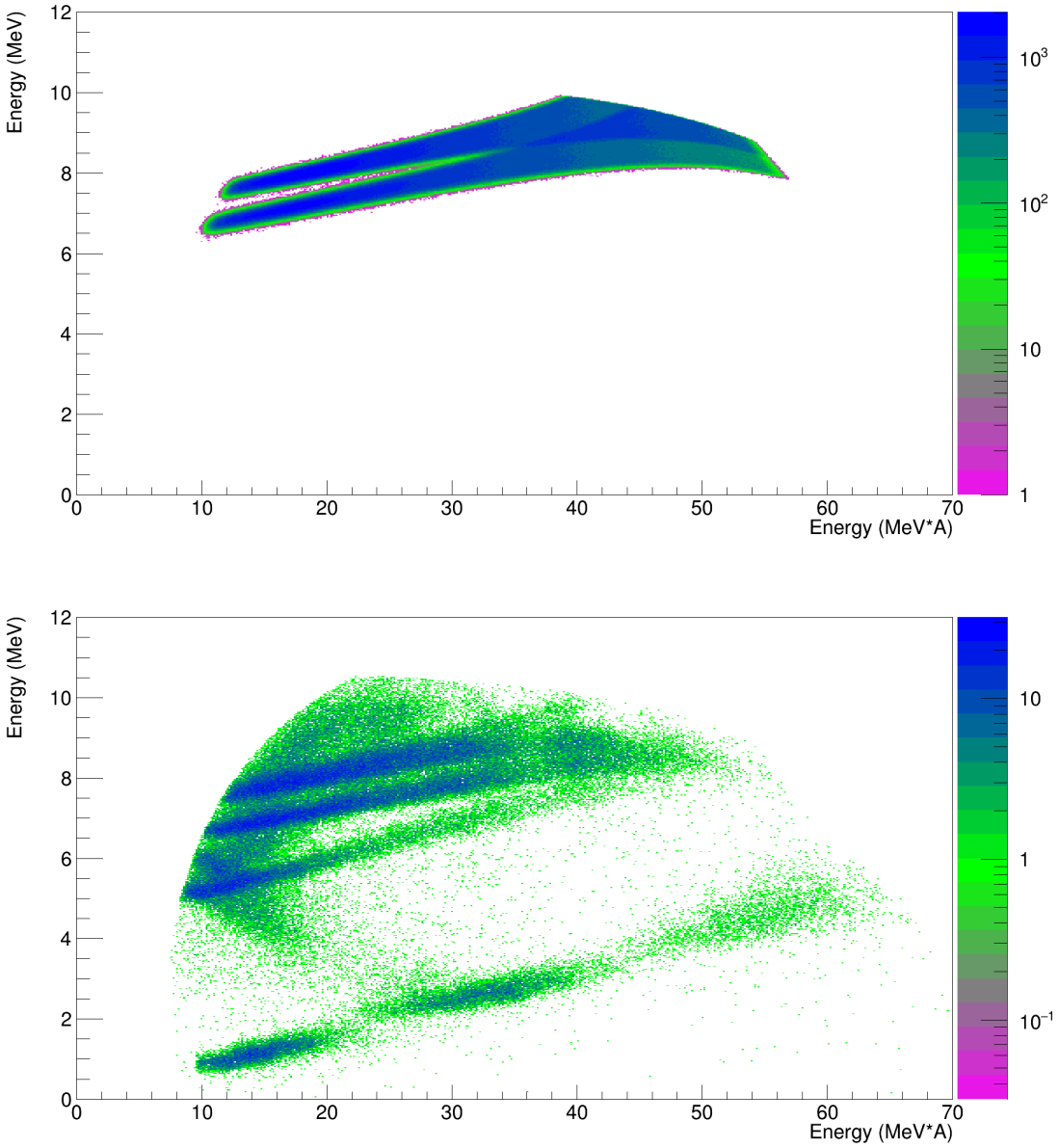

Figure 4.11: Comparison of simulated data (top) and real data (bottom) corresponding to the 6.129 MeV and 6.921 MeV states of ^{16}O

Chapter 5

Analysis and Results

It's a funny thing, ambition. It can take one to sublime heights or harrowing depths. And sometimes they are one and the same.
-Emily Kaldwin

To calculate the branching ratio and transition probabilities from the data, it is necessary to separate the recorded events generated by the emissions from the reaction of interest from the rest of the data. This is done by a graphical technique involving the Catania plot generated by the experimental data. The correlated gamma spectra generated from the regions on the Catania plot can be seen as the linear combination of energy spectra from known decays and the spectrum of the transition of interest.

From graphical gates in the Catania plots it is possible to generate correlated gamma spectra to the specific gated regions so the alpha-gamma events are correlated one to one.

In this experiment, several nuclear reactions have identical angle and energy of

detection in the Catania plot (detected alpha particles), as well as, in some cases energy of the detected gamma. But as more events are recorded, features in the gamma spectrum appear that are specific to the gamma energy spectra of those decays. The complete gamma spectrum of a gated region in the Catania plot then can be seen as the linear combination of the gamma decay spectra of those reactions regions on the Catania plot.

To find the amplitude of each gamma spectra, a program in python was written. The program takes, as inputs, a gamma spectra from a gated Catania plot, and a set of simulated gamma spectra that correspond to the possible reactions inside the gated regions on the Catania plot.

The regions on the Catania plot are chosen by simulating the experiment in **sudor** and selecting the geometric regions corresponding to each reaction as an individual gate on the Catania plot, as previously explained in chapter 4.

The result of the fitting program are amplitudes of each gamma spectra contribution, the individual spectra is then scaled and the integral of the scaled spectra is taken as the number of detected gamma events in the experiment.

After finding the number of emitted events from the energy transitions the branching ratios and B(E2) can be calculated. The complete procedure of this is described in this chapter.

5.1 Regions of Interest in the Catania Plot

An event from the reaction $\alpha + ^{12}C \rightarrow ^{16}O^{*} + \gamma \rightarrow \alpha_0 + ^{12}C_{g.s.}$ corresponds to an entry in the data files with a single hit in the $LaBr_3$ array and a single hit on one of the DSSDs telescopes and one count on the TDC. These types of events are not unique to the reaction of interest, as inelastic excitation reactions produced events with the same pattern of information. Events from the following reactions:

$$\alpha + ^{12}C \rightarrow \alpha + ^{12}\mathrm{C} + \gamma(4.438MeV)$$

$$\alpha + ^{16}O \rightarrow \alpha + ^{16}\mathrm{O} + \gamma(6.129MeV)$$

$$\alpha + ^{16}O \rightarrow \alpha + ^{16}\mathrm{O} + \gamma(6.917MeV)$$

will produce the same type of event as the ones from the reaction from interest. Not only that, but the simulations showed an overlap between the energy and angle of detected α particles as shown in figure 5.1.

By only analysing the Catania plot it is impossible to distinguish events from the reaction of interest. As described in section 3.5.2 it is possible to generate gamma spectra corresponding to alpha events in the Catania plot. If several reactions overlap in the Catania plot, then their corresponding gamma spectra would be overlapped too. The gamma spectrum of a Catania plot region can be seen as the linear combination of all of the associated reactions in that Catania plot area. The overlap in the gamma spectrum is more manageable as it is uni-dimensional.

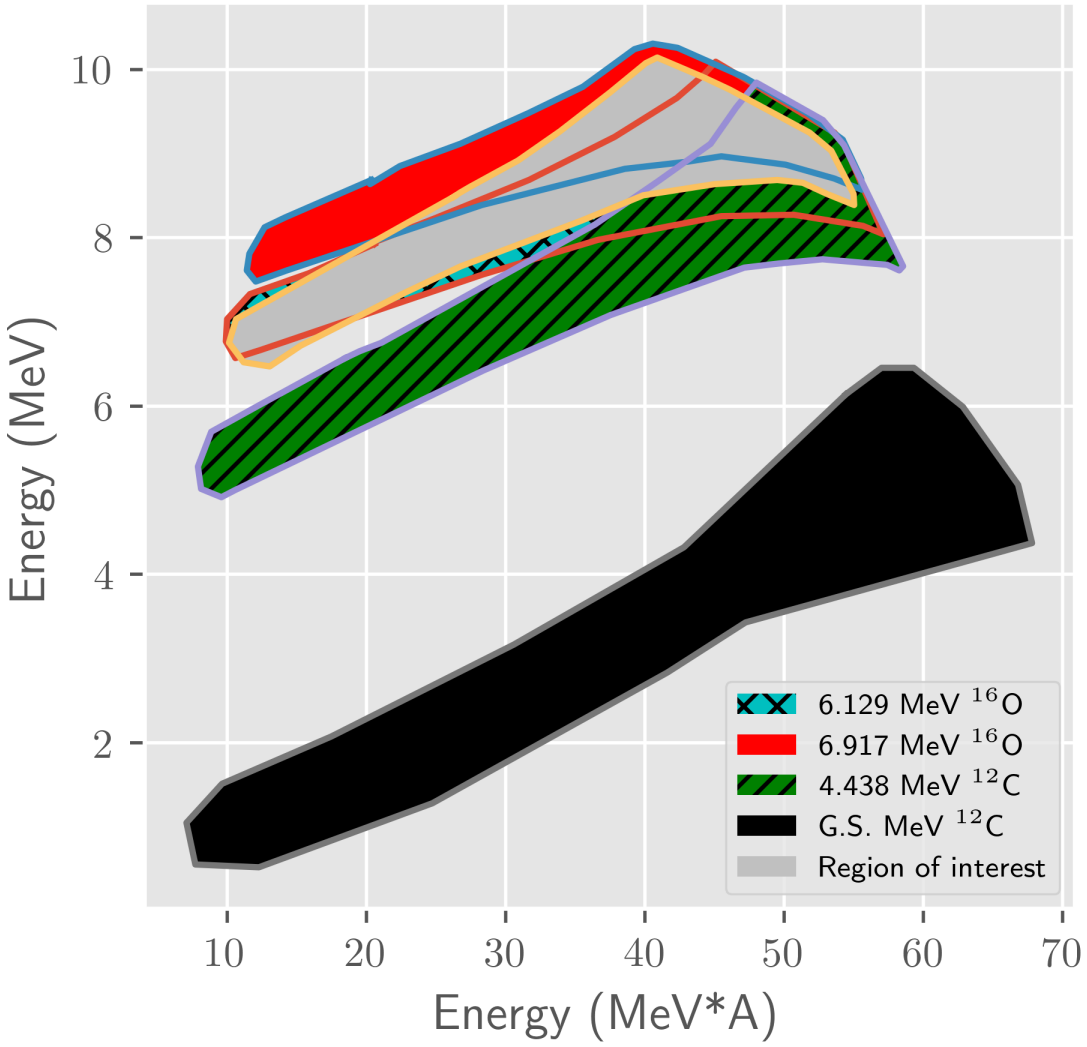

Figure 5.1: In the Catania plot any overlap between states is noticeable and is caused by factors like the proximity of the detector to the target and the energy smearing due to the thickness of the target. The overlap on the Catania plot will create overlapped gamma spectra.

5.2 Gamma Spectra Fitting

From the experimental data it is impossible to distinguish a unique locus on the Catania plot where events corresponding to the reaction of interest of this work are. These are comparatively fewer events of this kind.

By simulating the expected reactions presented in section 5.1 an overlap between these states and $\alpha +^{12} C \rightarrow^{16} O^* + \gamma \rightarrow \alpha +^{12} C_{g.s.}$ can be identified. The gamma

spectrum from the region of interest then has a contribution of six different spectra listed bellow:

- Gamma background from the experiment
- 6.129 MeV gamma from ^{16}O
- 6.917 MeV gamma from ^{16}O
- 4.438 MeV gamma from ^{12}C
- 5.919 MeV gamma from the ^{16}O (16.275 MeV, $J^{\pi} = 6^{+}$)
- 4.53 MeV unidentified gamma, seen only by some detectors.

The 4.438 MeV and the 4.53 MeV lie closely on the complete gamma spectrum, it is believed that the 4.53 MeV gamma ray comes from the interaction from the beam with the chamber as only some detectors were able to detect the 4.53 MeV. A gain shift was discarded as it would affect all of the spectrum which was not seen as shown in figure 5.2.

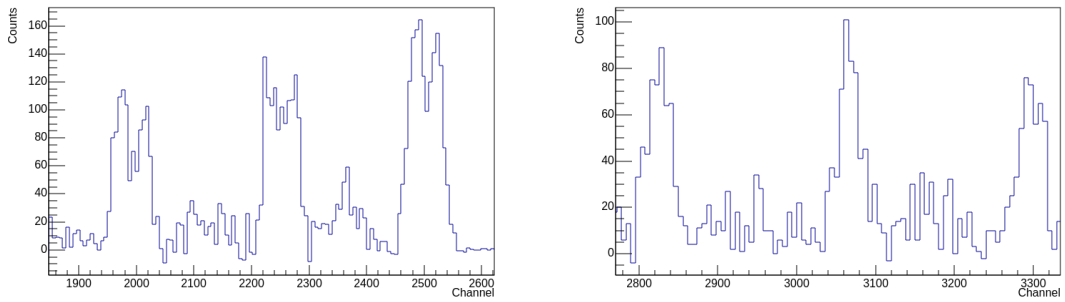

Figure 5.2: These spectra are extracted from the calibration program, their background and Compton contributions are removed using a ROOT tool [106][107][108]. The spectrum on the left corresponds to the 4.438 MeV and the 4.53 MeV gamma peaks, it is notable that there are two peaks for the full energy peaks and the corresponding escape peaks. The spectrum on the left correspond to the full energy peak and escape peaks from the 6.129 MeV gamma from ^{16}O and it is clear that there is no double peaking, ruling out a gainshift.

Only half of the detectors presented double peaking and they were connected to the same amplifier which was changed twice during the experiment. All the electronic chain from those detectors was carefully inspected. There appears to be

a correlation between the detection of two peaks in the region of 4.4 MeV with the position of the detectors as four of them lie in the same plane as shown in figure 5.3:

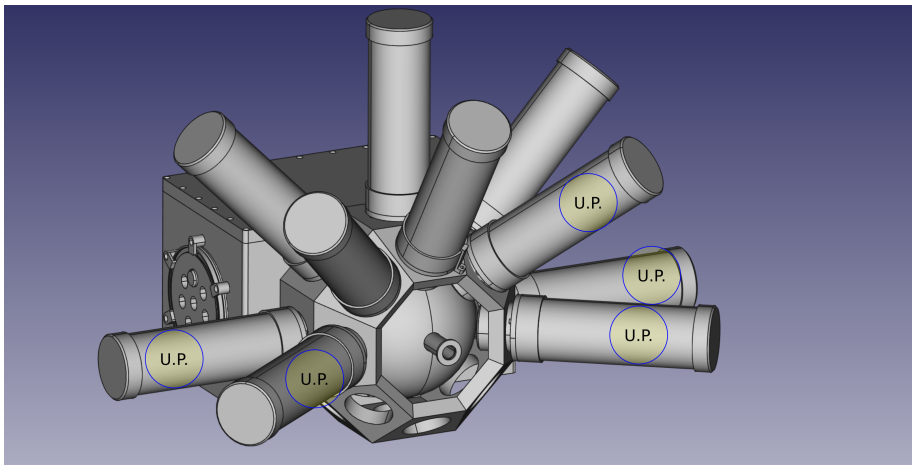

Figure 5.3: Computational image render of the detection array showing the detector which presented double peaking with the legend U.P. for unidentified peak.

The double peaking observed in some detectors was taken into consideration during the spectrum fitting of the reaction of interest. However, since it represented only a gamma decay at a well-defined energy, it did not pose a problem for the measurement.

To calculate the contribution of each state, a fitting program was written in python to run in a jupyter-notebook. The program takes, as input, the experimental spectrum and spectra from the simulated events corresponding to each contribution in that particular Catania plot gate. As each spectra comes from a high-count simulation (to reduce uncertainty for individual bins), the amplitudes from these spectra are several orders of magnitude greater than the experimental data, so a normalisation is performed. The normalisation coefficients are calculated from manually adjustments parameters in the data, provided by a graphical interface written for the program. The program then fits a linear combination of these normalised spectra to the experimental data of the form:

$$A_t(E) = \sum_{\omega} C_\omega f_\omega(E), \tag{5.1}$$

where $A_t(E)$is the resulting combination of the sum of all spectra and C_ω are the individual coefficients for each gamma spectrum $f_\omega(E)$. These coefficients C_ω are then used to scale each spectra and then, they are integrated to obtain the number of detected events. All of the simulated spectra used to fit the area where the Catania plot gate are set for the reaction can be found in appendix C. There is a contribution of background spectra to all of the possible loci on the Catania plot, composed by true random events[1]. To calculate it, it is necessary to find a region on the Catania plot where any associated gamma would be energetically forbidden. The region of $\alpha + ^{12}C \rightarrow \alpha_0 + ^{12}C$ is considered, as it does not excite the ^{12}C nucleus thus it should not have any associated gamma.

Any associated gamma event from the Catania plot gate on this region proceeds from another source. This spectrum is called Background$_{g.s.}$ (shown in appendix C).

To calculate the background contribution to any gamma spectrum from gating on the Catania plot, it is necessary to calculate the area of that specific region and then compare it to the area of the $\alpha + ^{12}C \rightarrow \alpha_0 + ^{12}C$. The ratio between these two areas function as a scaling factor for Background$_{g.s.}$. The scaled background spectrum is then subtracted from the gamma spectrum. Subtracting the background is better for the fitting routine as more parameters make it unstable.

Let us take the example of the region corresponding to the reaction $\alpha + ^{12}C \rightarrow \alpha + ^{12}C + \gamma(4.438MeV)$, generate its gamma spectrum and call it spectrum$_{4.438}$. The area of the region in the Catania plot associated with this reaction is 59.04 in arbitrary area units. The region corresponding to the $\alpha + ^{12}C \rightarrow \alpha_0 + ^{12}C$ is 91.22 in the same arbitrary units. This results on a scale factor of 0.64, if the scaled Background$_{g.s.}$ is subtracted from the gamma spectrum$_{4.438}$ (see figure 5.4), features corresponding to background effects will disappear and the resulting spectrum would fit better with the ideal spectrum discussed in section 2.6.

[1] A true random gamma event is a gamma ray produced by another nuclear reaction or cosmic event that reached the detector within the time of the gate.

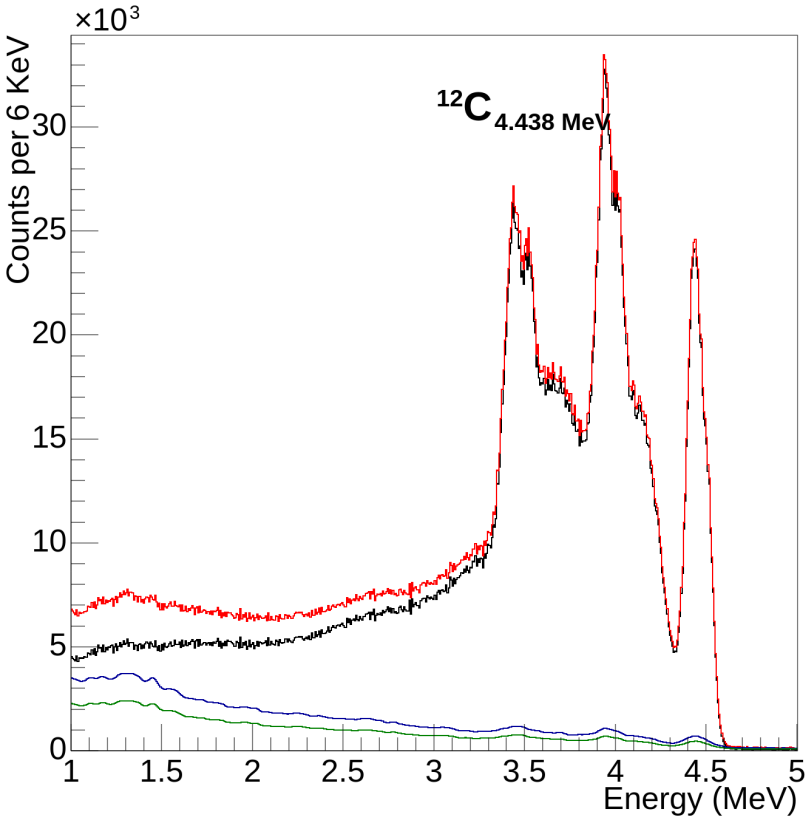

Figure 5.4: Red: Gamma spectrum from the Catania gate corresponding to the reaction $\alpha + ^{12}C \rightarrow \alpha_1 + ^{12}C + \gamma(4.438MeV)$. Blue: Background$_{g.s.}$. Green: scaled Background$_{g.s.}$. Black: Resulting spectrum from the subtraction, it is notable how features, specially around the 1 to 1.6 MeV are not present in this spectrum.

The fitting program outputs, are the coefficients for each contribution, as well as, the uncertainties associated of each coefficient. To extract the total number of detected gammas of each state it is necessary to integrate the scaled spectra.

The results for the region on the Catania plot corresponding to the reaction of interest are presented in table 5.1, and the fitted spectrum is shown in figure 5.5.

If a new fit is done using the same gated region on the Catania plot corresponding to the reaction of interest, using the same set of spectra as before but removing the gamma spectrum from the reaction of interest, leaving the coefficients fixed from the previous fit, then the χ^2/DoF=8.745, which represents a worse fit.

Another fit can be done using the same gated region on the Catania plot cor-

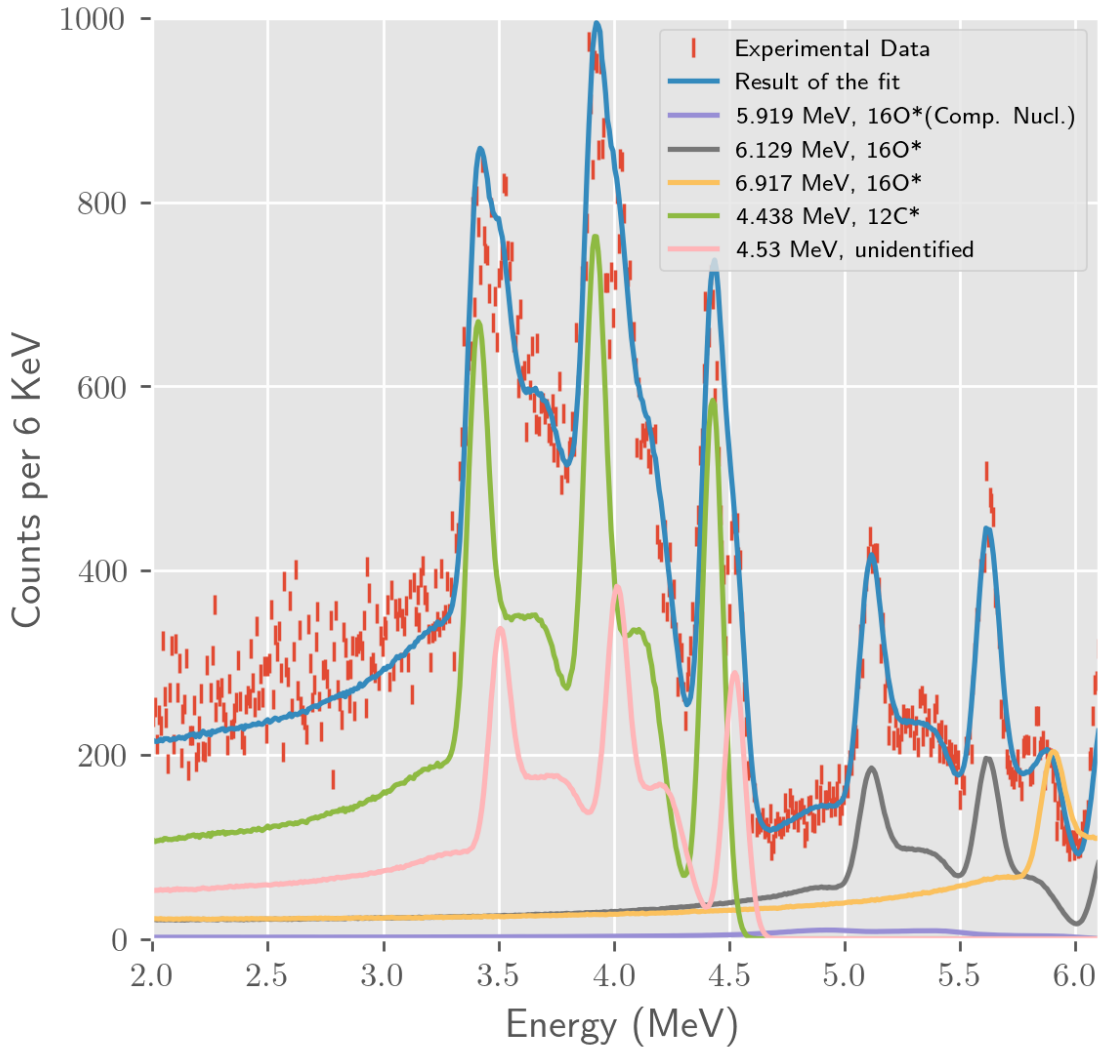

Figure 5.5: Contribution from all the overlapped simulated gamma spectra can be seen in this figure, as well as, the resulting fit composite of all of them to fit the experimental data. The calculated χ^2/DoF=1.50. DoF represent the degrees of freedom in the fit, in this case, a histogram, thus the degrees of freedom are the number of bins

Gamma Energy(MeV)	Relative Contribution (a.u.)	Integral (detected events)
4.438	0.25 ± 0.014	121308.19
4.530	0.251 ± 0.013	61038.12
6.129	18.344 ± 0.6078	74506.70
6.917	8.752 ± 0.8256	20040.76
5.919	0.537 ± 0.3904	2786.24

Table 5.1: An important concept to consider is the relative contribution is just a scale parameter for normalised spectra, it does not mean a direct contribution from that particular state. The relation with its uncertainty will dictate the uncertainty on the integral of each spectra and the calculation of emitted events

responding to the reaction of interest, using the same set of spectra as before but excluding the reaction of interest gamma spectrum, this time allowing the coefficients to adjust, results on $\chi^2/DoF = 1.7$. This value is close to the χ^2/DoF when the energy spectrum from the reaction of interest is considered, but it still represents a worse fit to the experimental data.

The number of events each state contributes to the total spectrum are extracted, by integrating each fitted spectrum. To obtain the relation between emitted and detected gammas, a simulation in GEANT4 at the specific energies of the reaction of interest was written, and it was carried out. For a variety of detected events, the number of emitted events was found. This allowed the mathematical relation between these quantities to be obtained, i.e. the efficiency relation.

A linear relation between the detected gamma rays and the emitted was found. This relation also contains the correction of only considering one of the crystals to be sensitive in the GEANT4 simulations as mentioned in section 4.1.

The determination of how many particles are emitted is not only affected by the detected particles and detector efficiencies but also by the that the state of interest might not be fully energetically populated by the energy of the beam. To expand on this, recall that the calculation in section 3.9 where the beam energy was found to be at 12.29 MeV, however, the reaction of interest can occur at any depth within

the target. If the reaction occurred at the front surface of the target, the compound nucleus would have all the kinetic energy of the beam available. The total available energy for this case, using equation 3.1, is 16.377 MeV, and the resonance is centred at 16.275 MeV ($\Gamma = 0.420$ MeV), meaning that the beam can only populate 59.6 $\pm$ 4.10 % of the state's full energy distribution. There is no lower-bound limit for the energy as the alpha particle might lose all of its energy inside the target. This result is calculated by approximating the state energy distribution as normal distribution, centred at 16.275 MeV and with a FWHM = 0.420 MeV. If the curve is integrated from 0 to the maximum energy of 16.377 MeV the portion of the populated energy can be obtained, this method is shown in figure 5.6:

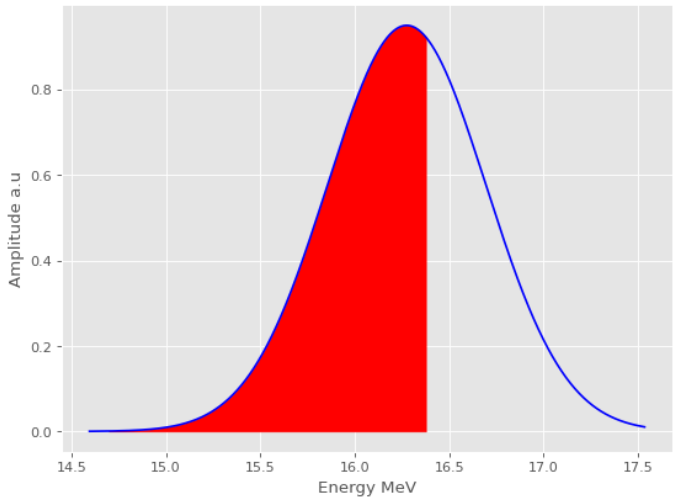

Figure 5.6: The shaded area represents the energy population of the state in the reaction studied in this work.

The uncertainty of the integral is of the order of magnitude of $\approx 10^{-11}$, the major contribution to the uncertainty is the beam energy spread.

The relation between emitted and detected considering all factors is:

$$N_{Emitted} = (22.73 \pm 0.03) N_{det} + (29924.59 \pm 16016.33), \tag{5.2}$$

where $N_{Emitted}$ is the number of emitted events and N_{det} is the number of detected events. A plot of these data and the linear fit are shown in figure 5.7. It is important

to note that even at zero N_{det}, there are emitted events in the formula. This effect is caused by two factors, one being the detector not covering all the solid angle and secondly, the detector not being fully efficient.

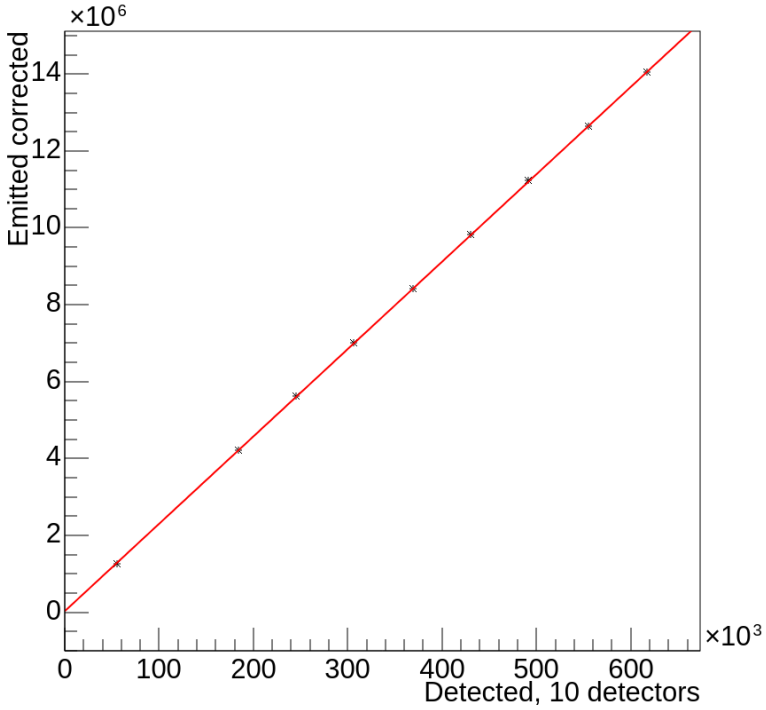

Figure 5.7: Relation between simulated emitted vs. detected events in the $LaBr_3$ array.

From these two techniques the number of gammas emitted by the reaction of interest can be extracted. To calculate the alpha-gamma branching of the compound nucleus reaction it is necessary to consider the events corresponding to the reaction:

$$\alpha +^{12} C \rightarrow^{16} O^* + \gamma \rightarrow \alpha +^{12} C_{g.s.},$$

and from the reaction:

$$\alpha +^{12} C \rightarrow^{16} O^* \rightarrow \alpha +^{12} C_{g.s.}.$$

The kinematic equations in appendix B show the reaction: $\alpha +^{12} C \rightarrow^{16} O^* \rightarrow$

$\alpha +^{12} C_{g.s.}$ is indistinguishable from $\alpha +^{12} C \rightarrow \alpha +^{12} C_{g.s.}$, as the $Q-$value for the formation of the compound nucleus is the same for the break-up. To measure this, a 2-D graphical gate is set-up on the Catania plot corresponding to this reaction and integrated over the area.

As the DSSDs do not cover all possible angles of emission a geometric efficiency correction is needed to obtain the total emitted events ($T_{g.s}$).

From appendix B it is predicted all alpha emission angles are possible in the reaction. But to calculate the geometric efficiency for the DSSDs is not as easy as to apply equation 3.6, as this formula is for detectors with circled face. This geometric efficiency correction factor is thus calculated by a user written Monte-Carlo simulation, where it was calculated that a fraction of 0.0519 ± 0.0001 of the full emission sphere was covered by the detectors. It is important to note that a factor of 1 would mean the full 4π sr solid angle was covered by the DSSDs.

The total number of events detected in the region on the Catania plot corresponding to the reaction $\alpha +^{12} C \rightarrow \alpha +^{12} C_{g.s.}$ was : $N_{g.s.} = 4.284 \pm 0.002 \times 10^8$, and the corrected number of events with the geometric efficiency correction is: $\Gamma_{g.s} = 1.310 \pm 0.00201 \times 10^9$.

By integrating the spectrum of the transition of interest, a total of $N_\gamma = (2.78214 \pm 2.0193) \times 10^3$ gamma rays were detected. Using equation 5.2, the total number of emitted gammas is $\Gamma_{^{16}O^*} = (9.32 \pm 4.86) \times 10^4$.

From $\Gamma_{g.s}$ and $\Gamma_{^{16}O^*}$ the branching ratio of gammas to alphas in the ^{16}O (16.272 MeV $J = 6^+$) decay is calculated to be:

$$B.R. = \frac{\Gamma_{^{16}O^*}}{\Gamma_{g.s}} = 1.1298 \pm 0.5897 \times 10^{-5}$$

from the equations in section 2.3.1 then the reduced transition probability B(E2) is:

$$B(E2; 6^+ \rightarrow 4^+)_{w.u.} = 3.316 \pm 1.736_{w.u.}, \tag{5.3}$$

or using e^2fm^4 units:

$$B(E2; 6^+ \rightarrow 4^+) = 7.942 \pm 4.158\ e^2fm^4. \tag{5.4}$$

The relatively large uncertainty on the detected gamma rays comes mostly from low rate of gamma detection from the state of interest. Despite this fact, it is possible to set an upper limit on the branching ratio and to the $B(E2; 6^+ \rightarrow 4^+)$ of the 6^+ to 4^+ transition and this is the first such measurement.

In order to test the method used in this work to calculate the branching ratio and consequently the $B(E2; 6^+ \rightarrow 4^+)$, lets consider the inelastic reactions:

- $\alpha + ^{12}C \rightarrow \alpha + ^{12}\mathrm{C} + \gamma(4.438MeV)$,
- $\alpha + ^{16}O \rightarrow \alpha + ^{16}\mathrm{O} + \gamma(6.129MeV)$,

These reactions do not have enough energy to excite the ^{12}C or the ^{16}O nuclei above the alpha particle threshold. If an alpha particle is detected from either of these reaction, it implies there must be a gamma ray that was emitted from the same reaction. This means that the branching ratio between alpha and gammas from these reactions then must be close to one. The results of this analysis is presented in table 5.2:

Reaction	Detected Gammas	Detected Alphas	Branching ratio
$(\alpha_1, ^{12}C)$	$(4.383\pm0.144)\times10^7$	$(1.3772\pm0.002)\times10^7$	0.5±0.01
$(\alpha_2, ^{16}O)$	$(1.4260\pm0.042)\times10^6$	$(5.700\pm0.009)\times10^7$	0.24±0.001

Table 5.2: Branching ratio results from inelastic reactions from $(\alpha_1, ^{12}C)$ and $(\alpha_2, ^{16}O)$

While the branching ratio is not exactly one, the quantities are close (within a factor of two for ^{12}C and factor of four in the case of ^{16}O). Notably the measurement for the $(\alpha_2, ^{16}O)$ branching ratio is especially complicated as the oxygen in the target is a contaminant. This suggests that the alpha-gamma branching ratio is reliable

within a factor of two and transferable to study more reactions where correlated particles are involved.

5.3 Theory comparisons

A comparison between this result and theoretical values was possible due to private communications with Dr.Chris Halcrow[2] who calculated the theoretical values presented in this work.

If both initial and final states are thought to be rotational tetrahedral states *i.e.* tetrahedral arrangements of four alpha particles, then the $B(E2; 6^+ \rightarrow 4^+) = 0$, this is because the tetrahedron has no quadrupole moment, meaning that there can be no $E2$ transition. This would suggest that the tetrahedral interpretation of this rotational band might be flawed (although the current results are consistent with 0 at 2-3 standard deviations). Using a simple rigid body analysis, there are spin 4 and spin 6 "square-like" states (a square of alpha particles, rotating).

In the rigid body analysis, a tetrahedron cannot decay into a square, so the only non-zero transition is between the square states:

- 6^+ tetrahedron $\rightarrow$ 4^+ tetrahedron: B(E2) = 0
- 6^+ tetrahedron $\rightarrow$ 4^+ square: B(E2) = 0
- 6^+ square $\rightarrow$ 4^+ tetrahedron: B(E2) = 0
- 6^+ square $\rightarrow$ 4^+ square: B(E2) = $\frac{9}{143}$ $|Q|^2$ = 20 $e^2\,fm^4$

The quantity Q is the quadrupole moment and $|Q^2|$ can be fitted using different methods. In this work it is assumed that the 0_2^+ and 2_1^+ states in ^{16}O are square-like states, then using the information in reference [57]:

$$B(E2; 2_1^+ \rightarrow 0_2^+) = 1/5|Q|^2 = 65 => |Q|^2 = 65 * 5\,e^2\,fm^4$$

If $B(E2; 6^+ \rightarrow 4^+)$ is calculated in the formalism of the Skyrme model follow-

[2]Dr. Chistopher Halcrow, chalcrow@kth.se

ing the methods described in references [47][48]. The following B(E2) for different geometric arrays are calculated:

- 6^+ tetrahedron $\rightarrow$ 4^+ tetrahedron: B(E2) = 0
- 6^+ tetrahedron $\rightarrow$ 4^+ square: B(E2) = 7.54 $e^2\,fm^4$
- 6^+ square $\rightarrow$ 4^+ tetrahedron: B(E2) = 0.46 $e^2\,fm^4$
- 6^+ square $\rightarrow$ 4^+ square: B(E2) = 1.65 $e^2\,fm^4$

a good agreement with the transition corresponding to the 6^+ tetrahedron $\rightarrow$ 4^+ square in the Skyrme model can be observed as well.

The differences in both calculations arise from the difference in the structure of quantum states. One thing to notice is that the calculated transitions are relatively small meaning that the states do not have significant overlap.

Chapter 6

Conclusions

An experiment involving the reaction:

$$\alpha + ^{12}C \rightarrow ^{16}O^{*} + \gamma(5.919MeV) \rightarrow \alpha + ^{12}C_{g.s.}$$

was performed at the MC40 Cyclotron facility at the University of Birmingham to study the branching ratio of gammas to alphas, in order to study the nuclear structure of the 16.275 MeV with $J^{\pi} = 6^{+}$ excitation level in the ^{16}O nucleus. At a beam energy of 12.29±0.04 MeV.

In order to archive the necessary statistical significance to measure the gamma to alpha branching ratio, the beam time for this experiment was ninety hours over the span of two months. This was particularly challenging during the global pandemic of COVID-19.

A novel method to analyse the data was created to extract the branching ratio of the reaction. The method involved:

- The development of a program with graphical interface to calibrate over 300 gamma energy spectra.
- Writing of an automated 3-alpha calibration for silicon detector.
- Development of a highly realistic simulation software which combines the ma-

terial response accuracy of GEANT4, energy-loss calculations of ATIMA and an in-house two-body kinematic solver to fit experimental data

- The development of a data analysis software which allowed the creation of correlated gamma spectra from geometric locus in a Catania plot composed from alpha events.

- The software design of a program which takes, as inputs, one convoluted gamma spectrum from experimental data and a set of functions which are suspected to form the convoluted gamma spectrum from real data, then it fits a linear combination of those functions and outputs the relative contributions and the integrals of said functions. This which enabled the decomposition of the gamma spectrum into the contributing components and the calculation of total gamma events detected.

- A method that uses simulations to correct for efficiency is employed to calculate the number of emitted events from the detected number of events. This method is applicable to both a gamma detection array and a charged particle detection array.

The gamma to alpha branching ratio for the 16.275 MeV, $J^\pi = 6^+$ transition to the 10.356 MeV, $J^\pi = 4^+$ energy levels in ^{16}O the was found to be:

$$B.R. = \frac{\Gamma_{^{16}O^*}}{\Gamma_{g.s}} = 1.1298 \pm 0.5897 \times 10^{-5},$$

And consequently the $B(E2; 6^+ \rightarrow 4^+)$ was calculated to be:

$$B(E2; 6^+ \rightarrow 4^+) = 3.316 \pm 1.736_{w.u.} = 7.942 \pm 4.158\ e^2 fm^4, \tag{6.1}$$

The novel method was tested by using it to measure the alpha to gamma branching ratio on the reactions:

- $\alpha + ^{12}C \rightarrow \alpha + ^{12}\mathrm{C} + \gamma(4.438MeV)$.
- $\alpha + ^{16}O \rightarrow \alpha + ^{16}\mathrm{O} + \gamma(6.129MeV)$.

which as not exciting the nucleus above the particle threshold and decaying only by gamma emission the branching ratios must be one. It was found that the branching ratios for the reactions were close to 1 suggesting a good performance of the method.

It it noticeable that the $B(E2; 6^+ \rightarrow 4^+)_{w.u.}$ for the 16.275 MeV, $J^\pi = 6^+$, reported in Weisskopf units is greater than 1 meaning that there is an enhancement with respect to the Weisskopf estimate due to the collectivity of the transition.

The data from the experiment are consistent with theoretical results, specially with the rigid body model when the ^{16}O is modelled as a square array with alpha particles on its vertices; and the transition between 6^+ tetrahedron $\rightarrow 4^+$ square states in the Skyrme model. More calculations for more models are needed to be performed, but these calculations fall from the scope of this work which was to perform the experiment.

An electromagnetic transition far above the particle threshold was measured creating a methodology to study, weak unbound resonances by gamma emission.

The $LaBr_3$ gamma detectors used in this work have only $\approx$3.5% intrinsic efficiency for 5.9 MeV gammas. This, along with a relatively small geometric coverage of the emission sphere gives rise to a large uncertainty on the gamma intensity measurement N_γ. Furthermore, the detection rate for gammas from the reaction of interest is low. The energy and angle of the alpha particles emitted by the compound nucleus overlap with three distinct states, the 4.438 MeV in ^{12}C and the 6.129 MeV, 6.917 MeV in states in ^{16}O, as well as, an unidentified 4.53 MeV gamma, which might be emitted from reaction of the beam with the reaction chamber. This complicates the analysis needed to identify the gammas of interest.

At the time of writing, this work represents one of the few direct measurements of $B(E2)$s in light nuclei above the particle threshold, and the first to measure this

reaction at this energy range. The challenge of these measurements arises from the low gamma to particle branching ratios and the high energies of the gammas.

A new measurement involving greater angular coverage inside the chamber could improve the measurement as the detection efficiency inside the chamber only depends on the solid angle covered by the detectors.

This recommendation only works if the beam is completely focus on the target as minimum divergence of the beam causes particle scattering with the chamber itself and the components inside of it. If these events are detected, the methods proposed in this work for measuring branching ratios would not work as it is based on how events can be separated in the Catania plot.

The $LaBr_3$ detectors are good balance between detection efficiency and resolution, installing more detectors would improve the measurement greatly, without any disadvantage other than having a more complicated set-up. Having a greater gamma detection coverage would also help to understand the peak around 4.52 MeV seen in some detectors, as it is possible to be caused by the angular distribution of the result of a nuclear reaction.

Aiming to have a more complete angular coverage would also allow to study the angular distribution of the emission which helps to the determination of the intrinsic nature of the excited nucleus.

Thank you for reading.

Bibliography

[1] G. Gamow. "Zur Quantentheorie des Atomkernes". In: *Zeitschrift für Physik* 51.3 (Mar. 1928), pp. 204–212. ISSN: 0044-3328. DOI: 10.1007/BF01343196. URL: https://doi.org/10.1007/BF01343196 (cit. on p. 11).

[2] Ronald W. Gurney and Edw. U. Condon. "Wave Mechanics and Radioactive Disintegration". In: *Nature* 122.3073 (Sept. 1928), pp. 439–439. ISSN: 1476-4687. DOI: 10.1038/122439a0. URL: https://doi.org/10.1038/122439a0 (cit. on p. 11).

[3] A Mayer MG and JHD Jensen. *Elementary Theory of Nuclear Shell Structure*. New York/London: John Wiley & Sons/Chapman & Hall, 1955 (cit. on p. 11).

[4] F. Hoyle. "On Nuclear Reactions Occuring in Very Hot STARS.I. the Synthesis of Elements from Carbon to Nickel." In: *The Astrophysical Journal Supplement* 1 (Nov. 1954), p. 121. DOI: 10.1086/190005 (cit. on p. 11).

[5] M. Freer and H.O.U. Fynbo. "The Hoyle state in 12C". In: *Progress in Particle and Nuclear Physics* 78 (2014), pp. 1–23. ISSN: 0146-6410. DOI: https://doi.org/10.1016/j.ppnp.2014.06.001. URL: https://www.sciencedirect.com/science/article/pii/S0146641014000453 (cit. on p. 11).

[6] Aage Bohr. "Rotational motion in nuclei". In: *Rev. Mod. Phys.* 48 (3 July 1976), pp. 365–374. DOI: 10.1103/RevModPhys.48.365. URL: https://link.aps.org/doi/10.1103/RevModPhys.48.365 (cit. on p. 11).

[7] Ben Mottelson. "Elementary modes of excitation in the nucleus". In: *Rev. Mod. Phys.* 48 (3 July 1976), pp. 375–383. DOI: 10.1103/RevModPhys.48.375. URL: https://link.aps.org/doi/10.1103/RevModPhys.48.375 (cit. on p. 11).

[8] James Rainwater. "Background for the spheroidal nuclear model proposal". In: *Rev. Mod. Phys.* 48 (3 July 1976), pp. 385–391. DOI: 10.1103/RevModPhys.48.385. URL: https://link.aps.org/doi/10.1103/RevModPhys.48.385 (cit. on p. 11).

[9] F. Hartmann. *Evolution of Silicon Sensor Technology in Particle Physics*. Springer Tracts in Modern Physics. Springer International Publishing, 2017. ISBN: 9783319644363. URL: https://books.google.co.uk/books?id=7WY9DwAAQBAJ (cit. on p. 12).

[10] A.M. Hillas. "Evolution of ground-based gamma-ray astronomy from the early days to the Cherenkov Telescope Arrays". In: *Astroparticle Physics* 43 (2013). Seeing the High-Energy Universe with the Cherenkov Telescope Array - The Science Explored with the CTA, pp. 19–43. ISSN: 0927-6505. DOI: https://doi.org/10.1016/j.astropartphys.2012.06.002. URL: https://www.sciencedirect.com/science/article/pii/S0927650512001326 (cit. on p. 12).

[11] S. R. Beane et al. "Magnetic Moments of Light Nuclei from Lattice Quantum Chromodynamics". In: *Phys. Rev. Lett.* 113 (25 Dec. 2014), p. 252001. DOI: 10.1103/PhysRevLett.113.252001. URL: https://link.aps.org/doi/10.1103/PhysRevLett.113.252001 (cit. on p. 12).

[12] S. R. Beane et al. "Light nuclei and hypernuclei from quantum chromodynamics in the limit of SU(3) flavor symmetry". In: *Phys. Rev. D* 87 (3 Feb. 2013), p. 034506. DOI: 10.1103/PhysRevD.87.034506. URL: https://link.aps.org/doi/10.1103/PhysRevD.87.034506 (cit. on p. 12).

[13] Evgeny Epelbaum. "Few-nucleon forces and systems in chiral effective field theory". In: *Progress in Particle and Nuclear Physics* 57.2 (Oct. 2006), pp. 654–741. ISSN: 0146-6410. DOI: 10.1016/j.ppnp.2005.09.002. URL: http://dx.doi.org/10.1016/j.ppnp.2005.09.002 (cit. on p. 12).

[14] Evgeny Epelbaum and Ulf-G. Meißner. "Chiral Dynamics of Few- and Many-Nucleon Systems". In: *Annual Review of Nuclear and Particle Science* 62.1 (Nov. 2012), pp. 159–185. ISSN: 1545-4134. DOI: 10.1146/annurev-nucl-102010-130056. URL: http://dx.doi.org/10.1146/annurev-nucl-102010-130056 (cit. on p. 12).

[15] Winfried Leidemann and Giuseppina Orlandini. "Modern Ab Initio Approaches and Applications in Few-Nucleon Physics with A >= 4". In: *Prog. Part. Nucl. Phys.* 68 (2013), pp. 158–214. DOI: 10.1016/j.ppnp.2012.09.001. arXiv: 1204.4617 [nucl-th] (cit. on p. 12).

[16] Sonia Bacca and Saori Pastore. "Electromagnetic reactions on light nuclei". In: *Journal of Physics G: Nuclear and Particle Physics* 41.12 (Nov. 2014), p. 123002. DOI: 10.1088/0954-3899/41/12/123002. URL: https://doi.org/10.1088/0954-3899/41/12/123002 (cit. on p. 12).

[17] K. Hebeler et al. "Nuclear Forces and Their Impact on Neutron-Rich Nuclei and Neutron-Rich Matter". In: *Annual Review of Nuclear and Particle Science* 65.1 (Oct. 2015), pp. 457–484. ISSN: 1545-4134. DOI: 10.1146/annurev-nucl-102313-025446. URL: http://dx.doi.org/10.1146/annurev-nucl-102313-025446 (cit. on p. 12).

[18] S. Binder et al. "Few-nucleon systems with state-of-the-art chiral nucleon-nucleon forces". In: *Physical Review C* 93.4 (Apr. 2016). ISSN: 2469-9993. DOI: 10.1103/physrevc.93.044002. URL: http://dx.doi.org/10.1103/PhysRevC.93.044002 (cit. on p. 12).

[19] David Jenkins. "Electromagnetic transitions as a probe of clustering in nuclei". In: *Journal of Physics: Conference Series* 436 (Apr. 2013), p. 012016. DOI: 10.1088/1742-6596/436/1/012016. URL: https://doi.org/10.1088/1742-6596/436/1/012016 (cit. on p. 12).

[20] V. M. Datar et al. "Direct Observation of the 4+ to 2+ Gamma Transition in Be8". In: *Physical Review Letters* 94.12 (Apr. 2005). ISSN: 1079-7114. DOI: 10.1103/physrevlett.94.122502. URL: http://dx.doi.org/10.1103/PhysRevLett.94.122502 (cit. on p. 12).

[21] V. M. Datar et al. "Electromagnetic Transition from the 4+ to 2+ Resonance in Be 8Measured via the Radiative Capture inHe4+He4". In: *Physical Review Letters* 111.6 (Aug. 2013). ISSN: 1079-7114. DOI: 10.1103/physrevlett.111.062502. URL: http://dx.doi.org/10.1103/PhysRevLett.111.062502 (cit. on p. 12).

[22] K. E. Rehm et al. "Branching ratio $\Gamma_\alpha/\Gamma_\gamma$ of the 4.033 MeV $3/2^+$ state in ^{19}Ne". In: *Phys. Rev. C* 67 (6 June 2003), p. 065809. DOI: 10.1103/PhysRevC.67.065809. URL: https://link.aps.org/doi/10.1103/PhysRevC.67.065809 (cit. on p. 12).

[23] S Pirrie et al. "Precision branching-ratio measurements in ^{18}O". In: *The European Physical Journal A* 57.4 (2021), pp. 1–12 (cit. on p. 12).

[24] Stuart Pirrie et al. "A method to determine branching ratios using charged particle detectors for states in 18O". In: () (cit. on p. 12).

[25] J. C. Manthuruthil, C. P. Poirier, and J. Walinga. "Nuclear Structure of Sc^{43}. II. Gamma-Ray Angular Correlations". In: *Phys. Rev. C* 1 (2 Feb. 1970), pp. 507–522. DOI: 10.1103/PhysRevC.1.507. URL: https://link.aps.org/doi/10.1103/PhysRevC.1.507 (cit. on p. 13).

[26] Niels Bohr. "Neutron Capture and Nuclear Constitution". In: *Nature* 137.3461 (Feb. 1936), pp. 344–348. ISSN: 1476-4687. DOI: 10.1038/137344a0. URL: https://doi.org/10.1038/137344a0 (cit. on p. 16).

[27] M. J. Fluss et al. "Investigation of the Bohr-Independence Hypothesis for Nuclear Reactions in the Continuum: α+Co^{59}, p+Ni^{62} and α+Fe^{56}, p+Cl^{59}". In: *Phys. Rev.* 187 (4 Nov. 1969), pp. 1449–1465. DOI: 10.1103/PhysRev.187.1449. URL: https://link.aps.org/doi/10.1103/PhysRev.187.1449 (cit. on p. 16).

[28] Lourdhu Bruno Chandrasekar, Kanagasabapathi Gnanasekar, and Marimuthu Karunakaran. "Exactly Solvable Problems in Quantum Mechanics". In: *Quantum Mechanics*. Ed. by Paul Bracken. Rijeka: IntechOpen, 2020. Chap. 2. DOI: 10.5772/intechopen.93317. URL: https://doi.org/10.5772/intechopen.93317 (cit. on p. 19).

[29] Sadegh Dehdar-behbahani and Abbas Parsaie. "Numerical modeling of flow pattern in dam spillway's guide wall. Case study: Balaroud dam, Iran". In: *Alexandria Engineering Journal* 55.1 (2016), pp. 467–473. ISSN: 1110-0168. DOI: https://doi.org/10.1016/j.aej.2016.01.006. URL: https://www.sciencedirect.com/science/article/pii/S1110016816000107 (cit. on p. 19).

[30] Gregory L. Johnson et al. "Stochastic Weather Simulation: Overview and Analysis of Two Commonly Used Models". In: *Journal of Applied Meteorology and Climatology* 35.10 (1996), pp. 1878–1896. DOI: 10.1175/1520-0450(1996)035<1878:SWSOAA>2.0.CO;2. URL: https://journals.ametsoc.org/view/journals/apme/35/10/1520-0450_1996_035_1878_swsoaa_2_0_co_2.xml (cit. on p. 19).

[31] Alfio Quarteroni. "Modeling the cardiovascular system—A mathematical adventure: Part I". In: *SIAM News* 34.5 (2001), pp. 1–3 (cit. on p. 19).

[32] B. T. Grenfell, G. Smith, and R. M. Anderson. “A mathematical model of the population biology of Ostertagia ostertagi in calves and yearlings”. In: *Parasitology* 95.2 (1987), pp. 389–406. DOI: 10.1017/S0031182000057826 (cit. on p. 19).

[33] Wolfgang Pauli. “Probleme der modernen Physik”. In: *Festschrift zum* 60 (1928), p. 30 (cit. on pp. 20, 22, 23).

[34] G. Audi, A.H. Wapstra, and C. Thibault. “The Ame2003 atomic mass evaluation: (II). Tables, graphs and references”. In: *Nuclear Physics A* 729.1 (2003). The 2003 NUBASE and Atomic Mass Evaluations, pp. 337–676. ISSN: 0375-9474. DOI: https://doi.org/10.1016/j.nuclphysa.2003.11.003. URL: https://www.sciencedirect.com/science/article/pii/S0375947403018098 (cit. on p. 23).

[35] K. M. Case and A. Pais. “On Spin-Orbit Interactions and Nucleon-Nucleon Scattering”. In: *Phys. Rev.* 80 (2 Oct. 1950), pp. 203–211. DOI: 10.1103/PhysRev.80.203. URL: https://link.aps.org/doi/10.1103/PhysRev.80.203 (cit. on p. 24).

[36] HyperPhysics. *Nuclear Shell Model*. Available from: http://hyperphysics.phy-astr.gsu.edu/hbase/Nuclear/shell.html. 2022. URL: http://hyperphysics.phy-astr.gsu.edu/hbase/Nuclear/shell.html (cit. on p. 25).

[37] P. Navrátil, J.P. Vary, and B.R. Barrett. *Large basis ab initio no-core shell model and its application to*. 2000 (cit. on p. 26).

[38] Alexander Volya and Vladimir Zelevinsky. “Discrete and continuum spectra in the unified shell model approach”. In: *Phys. Rev. Lett* 94 (2005), p. 052501 (cit. on p. 26).

[39] A. Nakada, Y. Torizuka, and Y. Horikawa. *Determination of the deformation in 12 C from electron scattering*. 1971 (cit. on p. 26).

[40] E.A. McCutchan. *Precise electromagnetic tests of ab-initio calculations of light nuclei: States in Be-10*. 2009 (cit. on p. 26).

[41] Lee and Ulf-G. MeiBner. *Lattice simulations for light nuclei: Chiral effective field theory at leading order*. 2007 (cit. on p. 26).

[42] Honma and Takaharu Otsuka. *New Generation of the Monte Carlo Shell Model for the K Computer Era*. 2012 (cit. on p. 26).

[43] L. R. Hafstad and E. Teller. "The Alpha-Particle Model of the Nucleus". In: *Phys. Rev.* 54 (9 Nov. 1938), pp. 681–692. DOI: 10.1103/PhysRev.54.681. URL: https://link.aps.org/doi/10.1103/PhysRev.54.681 (cit. on p. 27).

[44] W.D.M. RAE. "Clustering phenomena and shell effects in nuclear structure and reactions". In: *International Journal of Modern Physics A* 03.06 (1988), pp. 1343–1372. DOI: 10.1142/S0217751X88000576. eprint: https://doi.org/10.1142/S0217751X88000576. URL: https://doi.org/10.1142/S0217751X88000576 (cit. on p. 27).

[45] Kiyomi Ikeda, Noboru Takigawa, and Hisashi Horiuchi. "The Systematic Structure-Change into the Molecule-like Structures in the Self-Conjugate 4n Nuclei". In: *Progress of Theoretical Physics Supplement* E68 (1968), pp. 464–475. DOI: 10.1143/PTPS.E68.464. eprint: /oup/backfile/content_public/journal/ptps/e68/10.1143/ptps.e68.464/2/e68-464.pdf. URL: http://dx.doi.org/10.1143/PTPS.E68.464 (cit. on p. 27).

[46] D.M. Brink and J.J. Castro. "Alpha clustering effects in nuclear matter". In: *Nuclear Physics A* 216.1 (1973), pp. 109–124. ISSN: 0375-9474. DOI: https://doi.org/10.1016/0375-9474(73)90521-6. URL: http://www.sciencedirect.com/science/article/pii/0375947473905216 (cit. on p. 28).

[47] C. J. Halcrow, C. King, and N. S. Manton. "Oxygen-16 spectrum from tetrahedral vibrations and their rotational excitations". In: *International Journal of Modern Physics E* 28.04 (Apr. 2019), p. 1950026. ISSN: 1793-6608. DOI: 10.1142/s0218301319500265. URL: http://dx.doi.org/10.1142/S0218301319500265 (cit. on pp. 28, 105).

[48] C. J. Halcrow and J. I. Rawlinson. "Electromagnetic transition rates of ^{12}C and ^{16}O in rotational-vibrational models". In: *Phys. Rev. C* 102 (1 June 2020), p. 014314. DOI: 10.1103/PhysRevC.102.014314. URL: https://link.aps.org/doi/10.1103/PhysRevC.102.014314 (cit. on pp. 28, 105).

[49] J. Da Providência and C.M. Shakin. "Corrections to electromagnetic transition rates due to ground-state correlations". In: *Nuclear Physics A* 108.3 (1968), pp. 609–624. ISSN: 0375-9474. DOI: https://doi.org/10.1016/0375-9474(68)90328-X. URL: https://www.sciencedirect.com/science/article/pii/037594746890328X (cit. on p. 28).

[50] W. Bauhoff, H. Schultheis, and R. Schultheis. "Alpha cluster model and the spectrum of ^{16}O". In: *Phys. Rev. C* 29 (3 Mar. 1984), pp. 1046–1055. DOI: 10.1103/PhysRevC.29.1046. URL: https://link.aps.org/doi/10.1103/PhysRevC.29.1046 (cit. on p. 29).

[51] Aage Niels Bohr and Benjamin Roy Mottelson. "Collective and individual-particle aspects of nuclear structure". In: *Dan. Mat. Fys. Medd.* 27.CERN-57-38 (1953), pp. 1–174 (cit. on p. 30).

[52] Aage Bohr and Ben R. Mottelson. "Rotational States in Even-Even Nuclei". In: *Phys. Rev.* 90 (4 May 1953), pp. 717–719. DOI: 10.1103/PhysRev.90.717.2. URL: https://link.aps.org/doi/10.1103/PhysRev.90.717.2 (cit. on p. 30).

[53] Aage Bohr and Ben R. Mottelson. "Interpretation of Isomeric Transitions of Electric Quadrupole Type". In: *Phys. Rev.* 89 (1 Jan. 1953), pp. 316–317.

DOI: 10.1103/PhysRev.89.316. URL: https://link.aps.org/doi/10.1103/PhysRev.89.316 (cit. on p. 30).

[54] A Bohr and BR Mottelson. "On the theory of rotational spectra". In: *Soviet Atomic Energy* 14.1 (1963), pp. 36–39 (cit. on p. 30).

[55] H. Morinaga. "Interpretation of Some of the Excited States of $4n$ Self-Conjugate Nuclei". In: *Phys. Rev.* 101 (1 Jan. 1956), pp. 254–258. DOI: 10.1103/PhysRev.101.254. URL: https://link.aps.org/doi/10.1103/PhysRev.101.254 (cit. on p. 30).

[56] Ingemar Ragnarsson and Sven Gvsta Nilsson. "Rotational bands – the particle–rotor model". In: *Shapes and Shells in Nuclear Structure*. Cambridge University Press, 1995, pp. 181–205. DOI: 10.1017/CBO9780511563973.012 (cit. on pp. 30, 31).

[57] D.R. Tilley, H.R. Weller, and C.M. Cheves. "Energy levels of light nuclei A = 16 to 17". In: *Nuclear Physics A* 564.1 (1993), pp. 1–183. ISSN: 0375-9474. DOI: https://doi.org/10.1016/0375-9474(93)90073-7. URL: http://www.sciencedirect.com/science/article/pii/0375947493900737 (cit. on pp. 31, 46, 48, 76, 104).

[58] Donald R. Hamilton. "On Directional Correlation of Successive Quanta". In: *Phys. Rev.* 58 (2 July 1940), pp. 122–131. DOI: 10.1103/PhysRev.58.122. URL: https://link.aps.org/doi/10.1103/PhysRev.58.122 (cit. on p. 32).

[59] T. Kibédi et al. "Evaluation of theoretical conversion coefficients using BrIcc". In: *Nuclear Instruments and Methods in Physics Research Section A: Accelerators, Spectrometers, Detectors and Associated Equipment* 589.2 (2008), pp. 202–229. ISSN: 0168-9002. DOI: https://doi.org/10.1016/j.nima.2008.02.051. URL: https://www.sciencedirect.com/science/article/pii/S0168900208002520 (cit. on p. 35).

[60] William Dennis Hamilton and K. E. G. Lobner. *Electromagnetic interaction in nuclear spectroscopy*. North-Holland Publishing Co., Amsterdam, 1975. Chap. 5 (cit. on pp. 36, 38).

[61] Glenn F. Knoll. *Radiation detection and measurement*. English. 4th ed. Wiley New York, 2006. ISBN: 978-0-470-13148-0 (cit. on pp. 39, 45, 85).

[62] Donald C. Sachs and J. Reginald Richardson. "Mean Excitation Potentials". In: *Phys. Rev.* 89 (6 Mar. 1953), pp. 1163–1164. DOI: 10.1103/PhysRev.89.1163. URL: https://link.aps.org/doi/10.1103/PhysRev.89.1163 (cit. on p. 45).

[63] O.B. Tarasov and D. Bazin. "LISE++: Radioactive beam production with in-flight separators". In: *Nuclear Instruments and Methods in Physics Research Section B: Beam Interactions with Materials and Atoms* 266.19 (2008). Proceedings of the XVth International Conference on Electromagnetic Isotope Separators and Techniques Related to their Applications, pp. 4657–4664. ISSN: 0168-583X. DOI: https://doi.org/10.1016/j.nimb.2008.05.110. URL: https://www.sciencedirect.com/science/article/pii/S0168583X08007969 (cit. on pp. 48, 73).

[64] Stuart Pirrie et al. "Precision branching-ratio measurements in 18O". In: *The European Physical Journal A* 57 (Apr. 2021), p. 150. DOI: 10.1140/epja/s10050-021-00431-w (cit. on p. 50).

[65] Saint-Gobain. *LaBr Scintillation Crystal*. 2022. URL: https://www.crystals.saint-gobain.com/radiation-detection-scintillators/crystal-scintillators/lanthanum-bromide-labr3# (visited on 05/10/2022) (cit. on pp. 50, 57).

[66] Micron Semiconductor Ltd. *2018 catalogue Micron Semiconductor Limited*. 2018. URL: http://www.micronsemiconductor.co.uk/wp-content/

uploads/2018/03/2018-Micron-Semiconductor-Ltd-Silicon-Catalogue_Long-Form.pdf (visited on 08/21/2018) (cit. on pp. 50, 55).

[67] Thorlabs. *Thorlabs 60 mm Linear Translation Stage with Resonant Piezoelectric Motors*. 2022. URL: https://www.thorlabs.de/newgrouppage9.cfm?objectgroup_id=11736 (cit. on p. 52).

[68] Isotrak. *ALPHA SPECTROMETRY SOURCES*. 2022. URL: hhttps://www.gammadata.se/assets/Uploads/04-alpha-spectrometry-sources2.pdf (visited on 05/10/2022) (cit. on p. 55).

[69] P. Santa Rita. "MOmentum Neutron DEtector: MONDE". AV. UNIVERSIDAD Nº 3000, UNIVERSIDAD NACIONAL AUTÓNOMA DE MÉXICO, C.U., DISTRITO FEDERAL, 04510: Universidad Nacional Autonoma de Mexico, Apr. 2016 (cit. on p. 58).

[70] CERN ROOT jupyter notebook integration team. *How to use ROOT in a Jupyter notebook*. 2022. URL: https://root.cern.ch/notebooks/HowTos/HowTo_ROOT-Notebooks.html (visited on 05/10/2022) (cit. on pp. 61, 67).

[71] Steven M. Singer. *Sunsort reference manual*. 2022. URL: http://npg.dl.ac.uk/MIDAS/manual/SunSort/ (visited on 05/10/2022) (cit. on pp. 63, 67).

[72] Caen. *N568E16 Channel Programmable Spectroscopy Amplifier (Low Noise)*. 2022. URL: https://www.caen.it/products/n1168/ (visited on 05/10/2022) (cit. on p. 66).

[73] Mesytec. *Data sheet V8.006*. 2022. URL: https://www.mesytec.com/products/datasheets/MPR-16.pdf (visited on 05/10/2022) (cit. on p. 66).

[74] Caen. *V895 16 Channel Leading Edge Discriminator*. 2022. URL: https://www.caen.it/products/v895/ (visited on 05/10/2022) (cit. on p. 66).

[75] Caen. *V785 32 Channel Multievent Peak Sensing ADC*. 2022. URL: https://www.caen.it/products/v785/ (visited on 05/10/2022) (cit. on p. 66).

[76] Caen. *V775 32 Channel Multievent TDC*. 2022. URL: https://www.caen.it/products/v775/ (visited on 05/10/2022) (cit. on p. 66).

[77] Teledyne Lecroy. *428F QUAD LINEAR FAN-IN FAN-OUT*. 2022. URL: https://teledynelecroy.com/lrs/dsheets/428.htm (visited on 05/10/2022) (cit. on p. 66).

[78] Teledyne Lecroy. *222 NIM Dual Gate and Delay Generator*. 2022. URL: https://teledynelecroy.com/lrs/dsheets/222.htm (visited on 05/10/2022) (cit. on p. 66).

[79] Caen. *N1470 4 Ch Reversible 8 kV 3 mA (8 W) NIM HV Power Supply Module (USB)*. 2022. URL: https://www.caen.it/products/n1470/ (visited on 05/10/2022) (cit. on p. 66).

[80] Rene Brun and Fons Rademakers. "ROOT — An object oriented data analysis framework". In: *Nuclear Instruments and Methods in Physics Research Section A: Accelerators, Spectrometers, Detectors and Associated Equipment* 389.1 (1997). New Computing Techniques in Physics Research V, pp. 81–86. ISSN: 0168-9002. DOI: https://doi.org/10.1016/S0168-9002(97)00048-X. URL: https://www.sciencedirect.com/science/article/pii/S016890029700048X (cit. on p. 67).

[81] I. Antcheva et al. "ROOT — A C++ framework for petabyte data storage, statistical analysis and visualization". In: *Computer Physics Communications* 180.12 (2009). 40 YEARS OF CPC: A celebratory issue focused on quality software for high performance, grid and novel computing architectures, pp. 2499–2512. ISSN: 0010-4655. DOI: https://doi.org/10.1016/j.cpc.2009.08.005. URL: https://www.sciencedirect.com/science/article/pii/S0010465509002550 (cit. on p. 67).

[82] Guido Van Rossum and Fred L Drake Jr. *Python reference manual*. Centrum voor Wiskunde en Informatica Amsterdam, 1995 (cit. on p. 67).

[83] Encyclopædia Britannica. *cyclotron*. 2022. URL: https://www.britannica.com/technology/cyclotron#/media/1/148211/18064 (visited on 05/16/2022) (cit. on p. 68).

[84] Inc. Wikimedia Foundation. *Sum of normally distributed random variables*. 2021. URL: https://en.wikipedia.org/wiki/Sum_of_normally_distributed_random_variables#cite_note-3 (visited on 08/21/2018) (cit. on p. 70).

[85] Micron Semiconductor Ltd. *W1*. 2021. URL: http://www.micronsemiconductor.co.uk/product/w1/ (visited on 08/21/2018) (cit. on p. 70).

[86] R.K. Bhandari, P. Sen, and P. Mukherjee. "Correlation of time and energy resolutions in a cyclotron beam". In: *Nuclear Instruments and Methods in Physics Research Section A: Accelerators, Spectrometers, Detectors and Associated Equipment* 242.1 (1985), pp. 37–41. ISSN: 0168-9002. DOI: https://doi.org/10.1016/0168-9002(85)90887-3. URL: https://www.sciencedirect.com/science/article/pii/0168900285908873 (cit. on p. 71).

[87] GoodFellow. *GoodFellow Carbon - Microleaf*. 2022. URL: https://www.goodfellow.com/uk/en-gb/displayitemdetails/p/c-00-ml-000190/carbon-microleaf (cit. on p. 71).

[88] Geant4 Collaboration. *Book For Application Developers*. 2022. URL: https://geant4-userdoc.web.cern.ch/UsersGuides/ForApplicationDeveloper/html/ (cit. on pp. 75, 77).

[89] Hans Geissel et al. *ATIMA*. 2021. URL: https://web-docs.gsi.de/~weick/atima/ (cit. on pp. 75, 85).

[90] S. Agostinelli et al. "Geant4—a simulation toolkit". In: *Nuclear Instruments and Methods in Physics Research Section A: Accelerators, Spectrometers, Detectors and Associated Equipment* 506.3 (2003), pp. 250–303. ISSN: 0168-9002. DOI: https://doi.org/10.1016/S0168-9002(03)01368-8. URL: https:

//www.sciencedirect.com/science/article/pii/S0168900203013688 (cit. on p. 76).

[91] J. Allison et al. "Geant4 developments and applications". In: *IEEE Transactions on Nuclear Science* 53.1 (2006), pp. 270–278. DOI: 10.1109/TNS.2006.869826 (cit. on p. 76).

[92] J. Allison et al. "Recent developments in Geant4". In: *Nuclear Instruments and Methods in Physics Research Section A: Accelerators, Spectrometers, Detectors and Associated Equipment* 835 (2016), pp. 186–225. ISSN: 0168-9002. DOI: https://doi.org/10.1016/j.nima.2016.06.125. URL: https://www.sciencedirect.com/science/article/pii/S0168900216306957 (cit. on p. 76).

[93] A.E. Kiryunin et al. "GEANT4 physics evaluation with testbeam data of the ATLAS hadronic end-cap calorimeter". In: *Nuclear Instruments and Methods in Physics Research Section A: Accelerators, Spectrometers, Detectors and Associated Equipment* 560.2 (2006), pp. 278–290. ISSN: 0168-9002. DOI: https://doi.org/10.1016/j.nima.2005.12.237. URL: https://www.sciencedirect.com/science/article/pii/S0168900205026835 (cit. on p. 76).

[94] D. Costanzo et al. "The Geant4-Based Simulation Software of the ATLAS Detector". In: *2006 IEEE Nuclear Science Symposium Conference Record*. Vol. 1. 2006, pp. 5–11. DOI: 10.1109/NSSMIC.2006.356099 (cit. on p. 76).

[95] R. Lemrani et al. "Low-energy neutron propagation in MCNPX and GEANT4". In: *Nuclear Instruments and Methods in Physics Research Section A: Accelerators, Spectrometers, Detectors and Associated Equipment* 560.2 (2006), pp. 454–459. ISSN: 0168-9002. DOI: https://doi.org/10.1016/j.nima.2005.12.238. URL: https://www.sciencedirect.com/science/article/pii/S016890020502677X (cit. on p. 76).

[96] Dennis H. Wright et al. “Low and High Energy Modeling in Geant4”. In: *AIP Conference Proceedings* 896.1 (2007), pp. 11–20. DOI: 10.1063/1.2720453. eprint: https://aip.scitation.org/doi/pdf/10.1063/1.2720453. URL: https://aip.scitation.org/doi/abs/10.1063/1.2720453 (cit. on p. 76).

[97] L. Archambault et al. “Overview of Geant4 applications in medical physics”. In: *2003 IEEE Nuclear Science Symposium. Conference Record (IEEE Cat. No.03CH37515)*. Vol. 3. 2003, 1743–1745 Vol.3. DOI: 10.1109/NSSMIC.2003.1352215 (cit. on p. 76).

[98] L Desorgher et al. “Geant4 application for simulating the propagation of cosmic rays through the Earth’s magnetosphere”. In: *International Cosmic Ray Conference*. Vol. 7. 2003, p. 4281 (cit. on p. 76).

[99] V.N Ivanchenko. “Geant4 toolkit for simulation of HEP experiments”. In: *Nuclear Instruments and Methods in Physics Research Section A: Accelerators, Spectrometers, Detectors and Associated Equipment* 502.2 (2003). Proceedings of the VIII International Workshop on Advanced Computing and Analysis Techniques in Physics Research, pp. 666–668. ISSN: 0168-9002. DOI: https://doi.org/10.1016/S0168-9002(03)00538-2. URL: https://www.sciencedirect.com/science/article/pii/S0168900203005382 (cit. on p. 76).

[100] K. Amako et al. “Geant4 and its validation”. In: *Nuclear Physics B - Proceedings Supplements* 150 (2006). Proceedings of the 9th Topical Seminar on Innovative Particle and Radiation Detectors, pp. 44–49. ISSN: 0920-5632. DOI: https://doi.org/10.1016/j.nuclphysbps.2004.10.083. URL: https://www.sciencedirect.com/science/article/pii/S0920563205008066 (cit. on p. 76).

[101] J Apostolakis et al. “Progress in Geant4 Electromagnetic Physics Modelling and Validation”. In: *Journal of Physics: Conference Series* 664.7 (Dec. 2015),

p. 072021. DOI: 10.1088/1742-6596/664/7/072021. URL: https://doi.org/10.1088/1742-6596/664/7/072021 (cit. on p. 76).

[102] M. Ciemała et al. "Measurements of high-energy γ-rays with LaBr3:Ce detectors". In: *Nuclear Instruments and Methods in Physics Research Section A: Accelerators, Spectrometers, Detectors and Associated Equipment* 608.1 (2009), pp. 76–79. ISSN: 0168-9002. DOI: https://doi.org/10.1016/j.nima.2009.06.019. URL: https://www.sciencedirect.com/science/article/pii/S0168900209012170 (cit. on pp. 76, 82–84).

[103] I. Mouhti et al. "Validation of a NaI(Tl) and LaBr3(Ce) detector's models via measurements and Monte Carlo simulations". In: *Journal of Radiation Research and Applied Sciences* 11.4 (2018), pp. 335–339. ISSN: 1687-8507. DOI: https://doi.org/10.1016/j.jrras.2018.06.003. URL: https://www.sciencedirect.com/science/article/pii/S1687850718300530 (cit. on p. 76).

[104] Molnar G. L., Revay Z. Zs., and Belgya T. "Wide energy range efficiency calibration method for Ge detectors". In: *Nuclear Instruments and Methods in Physics Research. Section A, Accelerators, Spectrometers, Detectors and Associated Equipment* 489 (1-3 Aug. 2002). DOI: 10.1016/S0168-9002(02)00902-6 (cit. on p. 76).

[105] Dennis Wright: dwright@slac.stanford.edu. *LHEP Physics List Description*. 2007. URL: https://www.slac.stanford.edu/comp/physics/geant4/slac_physics_lists/ilc/LHEPlistdoc.html (visited on 05/16/2007) (cit. on p. 77).

[106] Miroslav Morháč et al. "Background elimination methods for multidimensional coincidence gamma-ray spectra". In: *Nuclear Instruments and Methods in Physics Research Section A: Accelerators, Spectrometers, Detectors and Associated Equipment* 401.1 (1997), pp. 113–132. ISSN: 0168-9002. DOI:

https://doi.org/10.1016/S0168-9002(97)01023-1. URL: https://www.sciencedirect.com/science/article/pii/S0168900297010231 (cit. on pp. 81, 94).

[107] Miroslav Morháč et al. "Efficient one- and two-dimensional gold deconvolution and its application to gamma-ray spectra decomposition". In: *Nuclear Instruments and Methods in Physics Research Section A: Accelerators, Spectrometers, Detectors and Associated Equipment* 401.2 (1997), pp. 385–408. ISSN: 0168-9002. DOI: https://doi.org/10.1016/S0168-9002(97)01058-9. URL: https://www.sciencedirect.com/science/article/pii/S0168900297010589 (cit. on pp. 81, 94).

[108] Miroslav Morháč et al. "Identification of peaks in multidimensional coincidence gamma-ray spectra". In: *Nuclear Instruments and Methods in Physics Research Section A: Accelerators, Spectrometers, Detectors and Associated Equipment* 443.1 (2000), pp. 108–125. ISSN: 0168-9002. DOI: https://doi.org/10.1016/S0168-9002(99)01005-0. URL: https://www.sciencedirect.com/science/article/pii/S0168900299010050 (cit. on pp. 81, 94).

[109] S. Hurtado, M. García-Leon, and R. García-Tenorio. "GEANT4 code for simulation of a germanium gamma-ray detector and its application to efficiency calibration". In: *Nuclear Instruments and Methods in Physics Research Section A: Accelerators, Spectrometers, Detectors and Associated Equipment* 518.3 (2004), pp. 764–774. ISSN: 0168-9002. DOI: https://doi.org/10.1016/j.nima.2003.09.057. URL: https://www.sciencedirect.com/science/article/pii/S0168900203028444 (cit. on p. 83).

[110] Helmut Weick et al. "Improved accuracy of the code ATIMA for energy loss of heavy ions in matter". In: Oct. 2018. URL: https://web-docs.gsi.de/~weick/atima/ATIMA_GSI_scientific_report_2017-5.pdf (cit. on p. 85).

[111] J. B. ball. *KINEMATICS II: A NONRELATIVISTIC KINEMATICS FORTRAN PROGRAM TO AID ANALYSIS OF NUCLEAR REACTION ANGULAR DISTRIBUTION DATA*. Oak Ridge National Laboratory, 1926. Chap. Appendix I (cit. on p. 133).

Appendices

Appendix A

Missing Particle Reconstruction Technique

Lets consider the reaction let's consider the reaction $\alpha + ^{12}C \rightarrow \alpha + ^{12}C$. The α particle is detected at an angle θ with an energy E_α as shown in figure A.1. The total linear momentum before and after the reaction has to be conserved

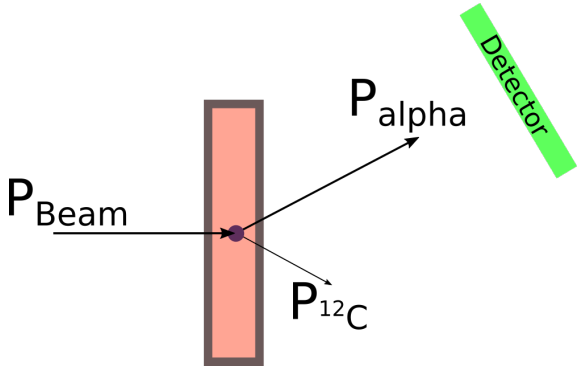

Figure A.1: Particle interaction schematic

$$\vec{P}_{beam} + \vec{P}_{target} = \vec{P}_{recoil} + \vec{P}_{product} \tag{A.1}$$

As the target is stationary respect with the beam then $\vec{p}_{target} = \vec{0}$ then:

$$\vec{P}_{beam} = \vec{P}_{\alpha} + \vec{P}_{^{12}C} \tag{A.2}$$

Re-arranging the equation we obtain:

$$\vec{P}_{^{12}C} = \vec{P}_{\alpha} - \vec{P}_{beam} \tag{A.3}$$

The components x,y,z of both sides of the equation need to be equal then:

$$\begin{aligned} \vec{P}_{Cx} &= \vec{P}_{Bx} - \vec{P}_{\alpha x} \\ \vec{P}_{Cy} &= \vec{P}_{By} - \vec{P}_{\alpha y} \\ \vec{P}_{Cz} &= \vec{P}_{Bz} - \vec{P}_{\alpha z} \end{aligned} \tag{A.4}$$

The components $\vec{P}_{Bx}$ and $\vec{P}_{By}$ are equal to $\vec{0}$ as the beam only moves in the direction $\hat{z}$

The magnitude of the momentum of an arbitrary particle ω with energy E_{ω} and mass m_{ω} can be calculated with:

$$\left|\vec{P}_{\omega}\right| = \sqrt[2]{2m_{\omega}E_{\omega}} \tag{A.5}$$

The total momentum of the ^{12}C then can be calculated by

$$\left|\vec{P}_{^{12}C}\right|^2 = \left|\vec{P}_{^{12}C_x}\right|^2 + \left|\vec{P}_{^{12}C_y}\right|^2 + \left|\vec{P}_{^{12}C_z}\right|^2 \tag{A.6}$$

Then from equation A.5 and A.6 we can calcualte the energy of the ^{12}C

To compute the energy of the recoil ^{12}C, we need data from the experiment where we can extract the angle θ and the energy E at which the particles were emitted. To calculate the components of momentum vector of a particle ω that was detected at an azimuth angle θ_y and an inclination θ_x first we need to calculate the magnitude of the momentum by using A.5 and then obtain its Cartesian components from the spherical components by using:

$$
\begin{aligned}
P_{\omega x} &= |P_{\omega}|\, cos(\theta_y) sin(\theta_x) \\
P_{\omega y} &= |P_{\omega}|\, sin(\theta_y) \\
P_{\omega z} &= |P_{\omega}|\, cos(\theta_x) cos(\theta_y)
\end{aligned}
\tag{A.7}
$$

Appendix B

Kinematics of a two-body Reaction

The specific mechanisms of nuclear interactions are still an open problem of nuclear physics, as the theories of interaction rely heavily on complicated mathematical concepts, computational calculations require a lot of time and power in order to obtain results to compare to experiments. We can analyse the two-body scattering to predict angles and energies of particles after the reaction as the total linear momentum must be conserved as well the total energy of the system. This analysis allow us to identify particles, assign excitation energy levels, verify positions and angles of detectors, etc.

It is common to study the scattering system of the beam/target $\rightarrow$ projectile(s)/ejectile(s) in the center-of-mass system and then translate the results to the laboratory system. If a particle of mass m_1 with a velocity of V_1 is scattered by a article of mass m_2 with a velocity of V_2, results in a scatter particle with mass m_3 with a velocity of V_3 and a projectile with mass m_4 with a velocity of V_4, as seen in figure B.1

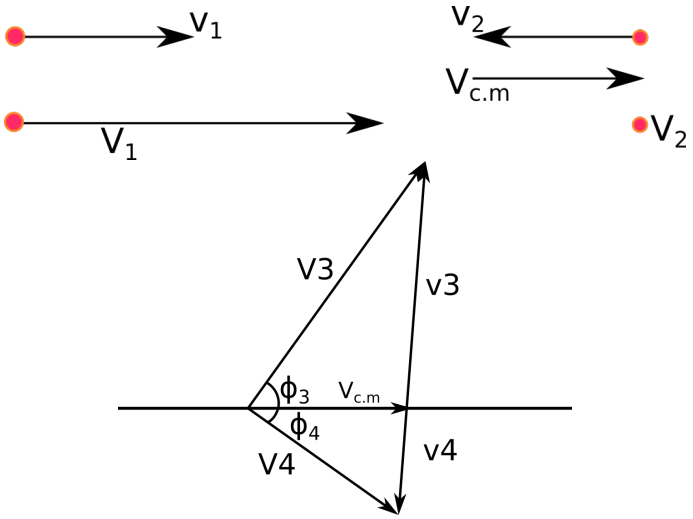

Figure B.1: Top: Representation of the system before the interaction, Bottom: System after the reaction

The Velocity of particle V_3 is:

$$V_3 = V_{c.m} cos(\phi_3) \pm (v_3 - V_{c.m}^2 sin(\phi_3))^2 \tag{B.1}$$

With:

$$V_{c.m} = \left[\left(\frac{2m_1}{(m_1 + m_2)^2} \right) E_{lab} \right]^{\frac{1}{2}} \tag{B.2}$$

And v_3 is the velocity of particle 3 in the center of mass:

$$v_3 = \left[\left(\frac{2}{m_3 + m_4} \right) \left(\frac{m_4}{m_3} \right) \left(\frac{m_2}{m_1 + m_2} \right) E_{lab} \right]^{\frac{1}{2}} \tag{B.3}$$

The energy of the particle that is measured is:

$$E_{measured} = \frac{1}{2} m_3 V_3^2 \tag{B.4}$$

A detailed derivation of these equations is on [111]. From these equations we can draw three conclusions.

- If $v_{ejectile} < V_{c.m}$, V_3 function is singled value for all angles.
- If $v_{ejectile} = V_{c.m}$, V_3 function is singled value for $0 \leq \phi \leq 90°$, and not defined

at 90°.

- If $v_{ejectile} \leq V_{c.m}$, V_3 is doubled valued for all vales of ϕ while the root is real.

The energy of particle 4 can be calculated by

$$E_{recol} = \frac{1}{2} m_4 V_4^2 \tag{B.5}$$

with:

$$V_4 = \left(v_4 + V_{c.m}^2 - 2 v_4 V_{c.m} cos(\theta_3)\right)^2 \tag{B.6}$$

and:

$$v_4 = -\left[\left(\frac{2}{m_3 + m_4}\right)\left(\frac{m_3}{m_4}\right)\left(\frac{m_2}{m_1 + m_2}\right) E_{lab}\right]^{\frac{1}{2}} \tag{B.7}$$

These results are helpful to simulate the kinematics of the particles involved in the experiment to help identify the particles detected.

Appendix C

Simulated Spectra to fit the reaction of interest gamma spectrum

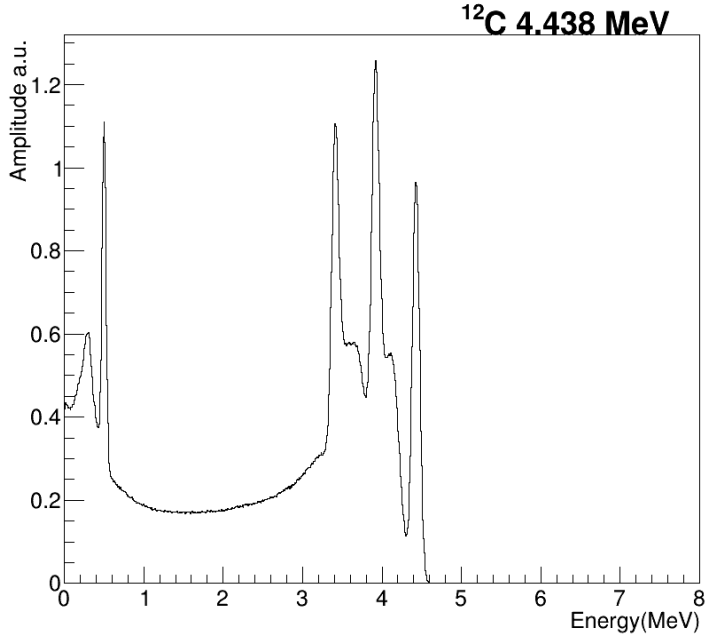

Figure C.1: Energy spectrum of the 4.438 MeV gamma decay from ^{12}C.

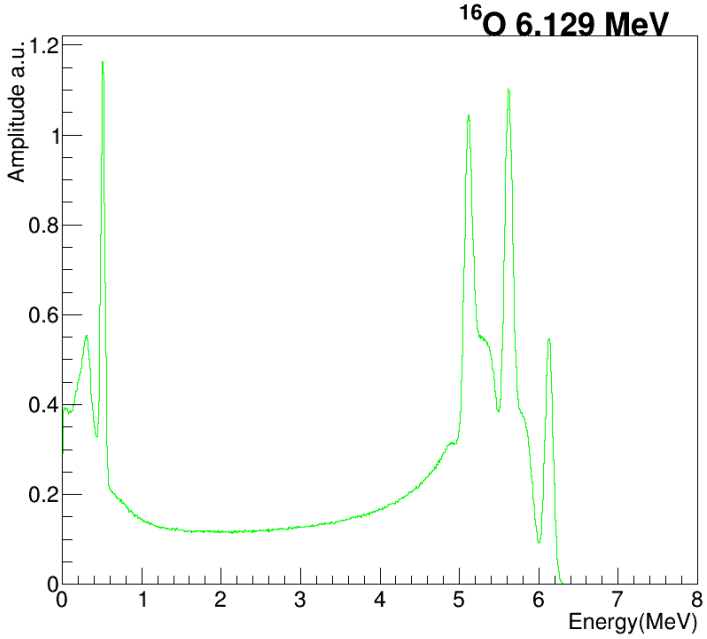

Figure C.2: Energy spectrum of the 6.129 MeV gamma decay from ^{16}O.

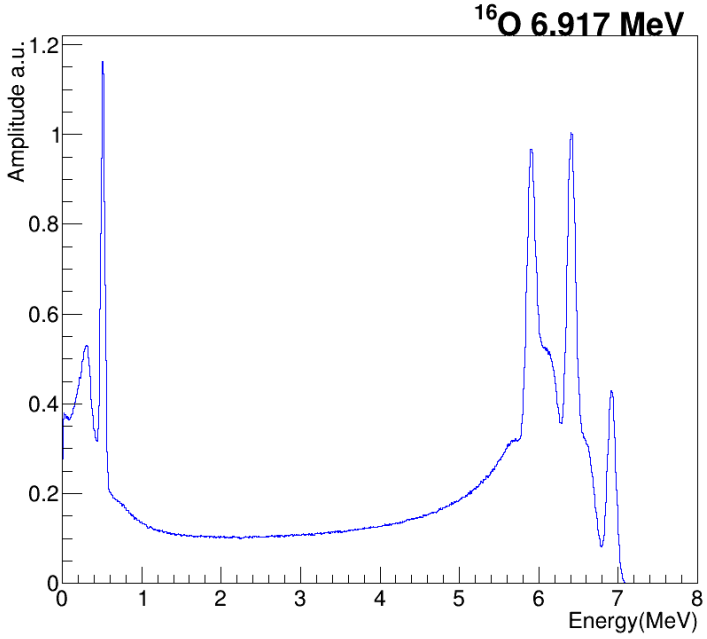

Figure C.3: Energy spectrum of the 6.917 MeV gamma decay from ^{16}O.

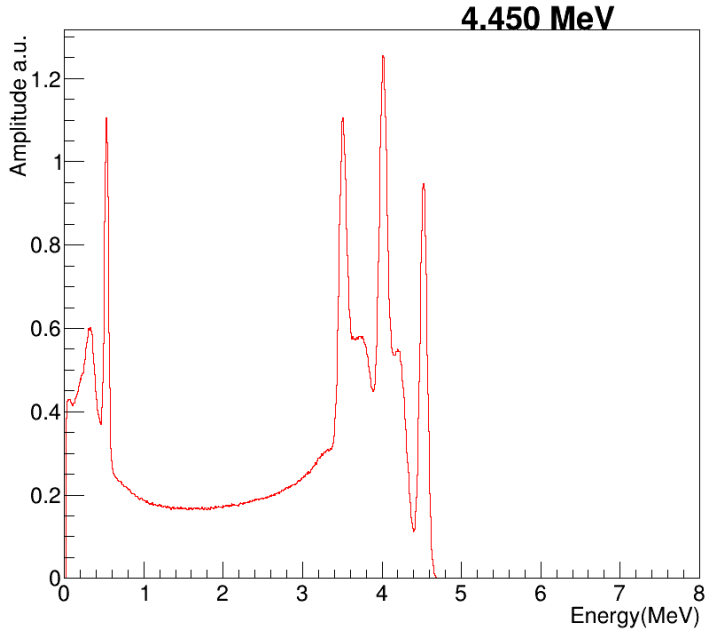

Figure C.4: Energy spectrum of the 4.50 MeV gamma decay from the unknown source.

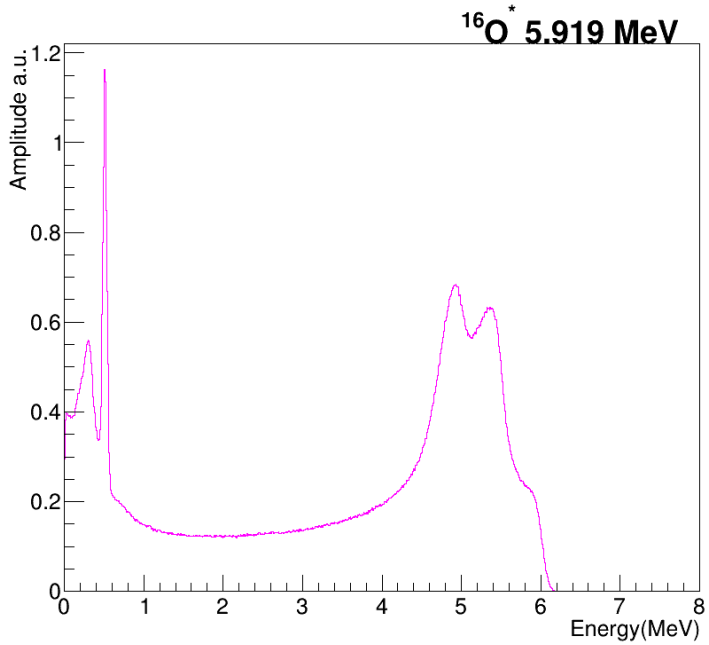

Figure C.5: Energy spectrum of the 5.919 MeV gamma decay from the 16.275 MeV, $J^{\pi} = 6^{+}$ level in ^{16}O.

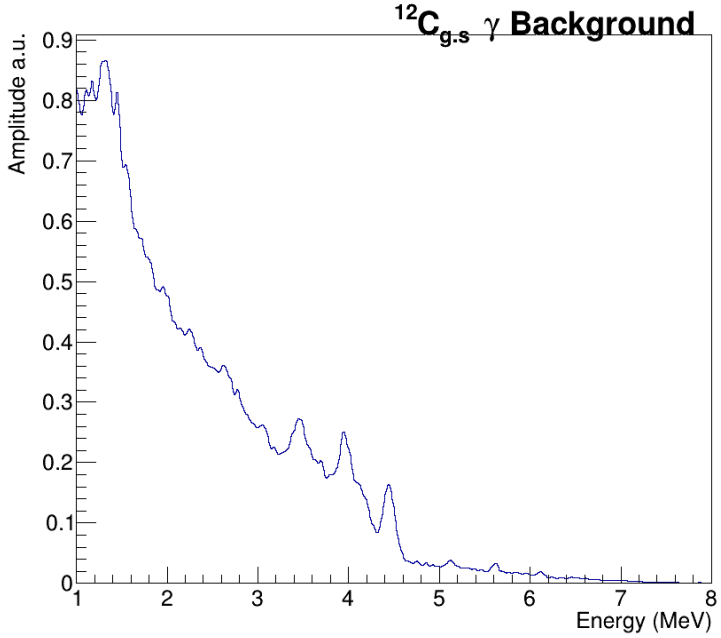

Figure C.6: Measured energy spectrum of the gamma background during the experiment.